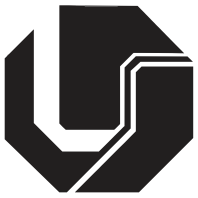

UNIVERSIDADE FEDERAL DE UBERLÂNDIA
FACULDADE DE ENGENHARIA MECÂNICA
PÓS-GRADUAÇÃO EM ENGENHARIA MECÂNICA

Aerodynamic Modeling and Simulation of a Reduced-Scale Generic Future Fighter Using Neuro-Fuzzy with Differential Evolution

Vitor Taha Sant'Ana

Uberlândia

2023

Vitor Taha Sant'Ana

Aerodynamic Modeling and Simulation of a Reduced-Scale Generic Future Fighter Using Neuro-Fuzzy with Differential Evolution

PhD Dissertation presented to the Graduation Program in Mechanical Engineering at the Federal University of Uberlândia, as part of the requirements for obtaining the degree of Doctor in Mechanical Engineering.

Focus Area: Solid Mechanics and Vibrations.
Research Line: Mechanical System Dynamics.

Prof. Dr. Roberto Mendes Finzi Neto,
Advisor

Uberlândia
2023

Dados Internacionais de Catalogação na Publicação (CIP)
Sistema de Bibliotecas da UFU, MG, Brasil.

S231a
2023

Sant'Ana, Vitor Taha, 1994-
Aerodynamic Modeling and Simulation of a Reduced-Scale Generic Future Fighter Using Neuro-Fuzzy with Differential Evolution [recurso eletrônico] / Vitor Taha Sant'Ana. - 2023.

Orientador: Roberto Mendes Finzi Neto.
Coorientador: Petter Krus.
Tese (Doutorado) - Universidade Federal de Uberlândia, Programa de Pós-Graduação em Engenharia Mecânica.
Modo de acesso: Internet.
Disponível em: http://doi.org/10.14393/ufu.te.2023.6006
Inclui bibliografia.

1. Engenharia Mecânica. I. Finzi Neto, Roberto Mendes (Orient.).II. Krus, Petter, 1958-, (Coorient.). III. Universidade Federal de Uberlândia. Programa de Pós-Graduação em Engenharia Mecânica. IV. Título.

CDU:621

Rejâne Maria da Silva
Bibliotecária – CRB6/1925

UNIVERSIDADE FEDERAL DE UBERLÂNDIA
Coordenação do Programa de Pós-Graduação em Engenharia Mecânica
Av. João Naves de Ávila, nº 2121, Bloco 1M, Sala 212 - Bairro Santa Mônica, Uberlândia-MG, CEP 38400-902
Telefone: (34) 3239-4282 - www.posmecanicaufu.com.br - secposmec@mecanica.ufu.br

ATA DE DEFESA - PÓS-GRADUAÇÃO

Programa de Pós-Graduação em:	Engenharia Mecânica				
Defesa de:	Tese de Doutorado Acadêmico, nº 367, PPGEM				
Data:	13/11/2023	Hora de início:	08:00	Hora de encerramento:	
Matrícula do Discente:	11923EMC011				
Nome do Discente:	Vitor Taha Sant'Ana				
Título do Trabalho:	Aerodynamic Modeling and Simulation of a Reduced-Scale Generic Future Fighter Using Neuro-Fuzzy with Differential Evolution				
Área de concentração:	Mecânica dos Sólidos e Vibrações				
Linha de pesquisa:	Dinâmica de Sistemas Mecânica				
Projeto de Pesquisa de vinculação:					

Reuniu-se por meio de videoconferência a Banca Examinadora, designada pelo Colegiado do Programa de Pós-graduação em Engenharia Mecânica, assim composta: Professores Doutores: Roberto Kawakami Harrop Galvão - ITA; Ingo Max Werner Staack - Technische Universität Braunschweig; Neusa Maria Franco de Oliveira - ITA; Valder Steffen Júnior - FEMEC/UFU; Aldemir Aparecido Cavalini Júnior FEMEC/UFU; e Roberto Mendes Finzi Neto, orientador do candidato.

Iniciando os trabalhos, o presidente da mesa, Dr. Roberto Mendes Finzi Neto, apresentou a Comissão Examinadora e o candidato, agradeceu a presença do público, e concedeu ao Discente a palavra para a exposição do seu trabalho. A duração da apresentação do Discente e o tempo de arguição e resposta foram conforme as normas do Programa.

A seguir o senhor(a) presidente concedeu a palavra, pela ordem sucessivamente, aos(às) examinadores(as), que passaram a arguir o(a) candidato(a). Ultimada a arguição, que se desenvolveu dentro dos termos regimentais, a Banca, em sessão secreta, atribuiu o resultado final, considerando o(a) candidato(a):

Aprovado.

Esta defesa faz parte dos requisitos necessários à obtenção do título de Doutor.

O competente diploma será expedido após cumprimento dos demais requisitos, conforme as normas do Programa, a legislação pertinente e a regulamentação interna da UFU.

Nada mais havendo a tratar foram encerrados os trabalhos. Foi lavrada a presente ata que após lida e achada conforme foi assinada pela Banca Examinadora.

Documento assinado eletronicamente por **Roberto Mendes Finzi Neto**, **Professor(a) do Magistério Superior**, em 13/11/2023, às 10:58, conforme horário oficial de Brasília, com fundamento no art. 6º, § 1º, do Decreto nº 8.539, de 8 de outubro de 2015.

Documento assinado eletronicamente por **Aldemir Aparecido Cavalini Junior**, **Professor(a) do Magistério Superior**, em 13/11/2023, às 10:59, conforme horário oficial de Brasília, com fundamento no art. 6º, § 1º, do Decreto nº 8.539, de 8 de outubro de 2015.

Documento assinado eletronicamente por **Roberto Kawakami Harrop Galvão**, **Usuário Externo**, em 13/11/2023, às 10:59, conforme horário oficial de Brasília, com fundamento no art. 6º, § 1º, do Decreto nº 8.539, de 8 de outubro de 2015.

Documento assinado eletronicamente por **Ingo Max Werner Staack**, **Usuário Externo**, em 13/11/2023, às 10:59, conforme horário oficial de Brasília, com fundamento no art. 6º, § 1º, do Decreto nº 8.539, de 8 de outubro de 2015.

Documento assinado eletronicamente por **Valder Steffen Junior**, **Professor(a) do Magistério Superior**, em 13/11/2023, às 10:59, conforme horário oficial de Brasília, com fundamento no art. 6º, § 1º, do Decreto nº 8.539, de 8 de outubro de 2015.

Documento assinado eletronicamente por **Neusa Maria Franco de Oliveira**, **Usuário Externo**, em 13/11/2023, às 12:39, conforme horário oficial de Brasília, com fundamento no art. 6º, § 1º, do Decreto nº 8.539, de 8 de outubro de 2015.

A autenticidade deste documento pode ser conferida no site https://www.sei.ufu.br/sei/controlador_externo.php?acao=documento_conferir&id_orgao_acesso_externo=0, informando o código verificador **4901698** e o código CRC **3F9D4A26**.

Referência: Processo nº 23117.074151/2023-97 SEI nº 4901698

Acknowledgements

I would like to express my deep gratitude to everyone who has contributed to my journey. Starting with my colleagues at the Federal University of Uberlândia, I won't name everyone, but please know that you are in my thoughts with great kindness. Every professor who has played even a small part in my journey to this point deserves sincere appreciation.

I would also like to thank Professor Leonardo Sanches, who introduced me to the fields of Neuro-Fuzzy and Flight Dynamics, and my advisor Roberto Finzi, who was always by my side when I needed him.

To my father, mother, and brother, thank you for your unwavering support and invaluable advice. I am also grateful to all my friends and professors at Linköping University, including Ingo Staack, Petter Krus, and Roger Larsson, for their interesting conversations and guidance. Accepting me as a visiting Ph.D. student at LiU meant a lot to me, and I appreciate all your support.

Finally, my deepest gratitude goes to my wife, Ana Carolina, for everything, especially for accompanying me on my trip to Sweden. Without your support, this Ph.D. would have been much more difficult. This achievement is not just mine, it is ours.

"If you can’t explain it simply,
you don’t understand it well enough."
Albert Einstein

Resumo

Sant'Ana, V. T. *Aerodynamic Modeling and Simulation of a Reduced-Scale Generic Future Fighter Using Neuro-Fuzzy with Differential Evolution*. PhD Dissertation - Federal University of Uberlândia, November 2023.

A busca por modelos aerodinâmicos precisos em engenharia aeronáutica tem levado à exploração de técnicas computacionais avançadas. Esta pesquisa explora a aplicação do Neuro-Fuzzy hibridizado com a Evolução Diferencial (NF-ED) como ferramenta para alcançar um modelo e simulação aerodinâmica com elevada fidelidade para um modelo em escala reduzida de um caça conhecido como Generic Future Fighter (GFF). O objetivo principal é desenvolver uma metodologia de identificação de sistema através de teste em voo para adquirir modelos aerodinâmicos detalhados e não estacionários, especialmente para esta aeronave, combinando a interpretabilidade de Sistemas de Baseados em Regras Fuzzy (SBRF) com a adaptatbilidade das Redes Neurais Artificiais (RNA). Esta pesquisa apresenta uma comparação entre o NF-ED e outros métodos de otimização, e também outro método de inferência fuzzy. Após a obtenção do modelo aerodinâmico não estacionários com base nas aproximações das séries de Taylor para cada coeficiente de força e momento, é construída uma simulação de 6 graus de liberdade no ambiente Simulink do Matlab.

Palavras-chave: Modelagem Aerodinâmica. Neuro-Fuzzy. Identificação de Sistemas. Teste em voo. Evolução Diferencial.

Abstract

Sant'Ana, V. T. *Aerodynamic Modeling and Simulation of a Reduced-Scale Generic Future Fighter Using Neuro-Fuzzy with Differential Evolution*. PhD Dissertation - Federal University of Uberlândia, November 2023.

The pursuit of accurate aerodynamic modeling in aeronautical engineering has driven the exploration of advanced computational techniques. This research applies Neuro-Fuzzy Hybridized with Differential Evolution (NF-DE) to develop a high-fidelity aerodynamic model and simulation for the Generic Future Fighter (GFF), a reduced-scale aircraft. The primary objective is to create a system identification methodology through flight testing for detailed and unsteady aerodynamic models. The methodology combines the interpretability of Fuzzy Inference Systems (FIS) with the adaptability of Artificial Neural Networks (ANN). The study includes a comparison between NF-DE and alternative optimization and fuzzy inference methods. After developing unsteady aerodynamic models based on first Taylor series equations for each force and moment coefficient, a 6-degrees-of-freedom (DOF) simulation is designed in Matlab's Simulink environment.

Keywords: Aerodynamic Modeling. Neuro-Fuzzy. System Identification. Flight Testing. Differential Evolution.

Contents

Figure List

Table List

List of Symbols

Acronyms

AI Artificial Intelligence

ANFIS Adaptive Network-based Fuzzy Inference System

ANN Artificial Neural Network

DE Differential Evolution

FFT Fast Fourier Transform

FIS Fuzzy Inference System

FTO First Taylor Order

GA Genetic Algorithm

GFF Generic Future Fighter

MF Membership Function

MTOW Maximum takeoff weight

NF Neuro-Fuzzy

NF-CRF Neuro-Fuzzy with Complex RF

NF-DE Neuro-Fuzzy with Differential Evolution

NF-GA Neuro-Fuzzy with Genetic Algorithm

PCC Pearson's Correlation Coefficient

Greek Symbols

α Angle of attack

β Sideslip angle

μ Air viscosity

ϕ Euler angle with aircraft's X body axis

ψ Euler angle with aircraft's Z body axis

ρ Air specific mass

θ Euler angle with aircraft's Y body axis

Latin Symbols

$\dot{p}$ Euler angle acceleration in X axis

$\dot{q}$ Euler angle acceleration in Y axis

$\dot{r}$ Euler angle acceleration in Z axis

$\overline{c}$ Mean aerodynamic chord

$\overline{q}$ Dynamic pressure

A Wing aspect ratio

b Wing span

C_D Drag coefficient

C_L Lift coefficient

C_l Moment coefficient around aircraft's body X axis

C_m Force coefficient in aircraft's body Y axis

C_n Force coefficient in aircraft's body Z axis

C_X Force coefficient in aircraft's body X-axis

C_Y Force coefficient in aircraft's body Y-axis

C_Z Force coefficient in aircraft's body Z-axis

C_{D_0} Drag coefficient at zero angle of attack

E Young modulus

e Oswald's efficiency factor

F_X Force in X axis

F_Y Force in Y axis

F_Z Force in Z axis

I_{XX} Aircraft's inertia moment about X axis

I_{XZ} Aircraft's product of inertia

I_{YY} Aircraft's inertia moment about Y axis

I_{ZZ} Aircraft's inertia moment about Z axis

L Moment around X axis

L_f Lift force

M Moment around Y axis

N Moment around Z axis

p Euler angle velocity in X axis (roll rate)

q Euler angle velocity in Y axis (pitch rate)

r Euler angle velocity in Z axis (yaw rate)

Re Reynolds number

S Reference wing area

u Velocity in aircraft's X axis

V Total velocity of the aircraft

v Velocity in aircraft's Y axis

w Velocity in aircraft's Z axis

X Aircraft's body axis pointed to the nose

Y Aircraft's body axis pointed to the right wing

Z Aircraft's body axis pointed to the ground

Chapter 1

Introduction

This chapter is going to present an overall idea about this study, and it is divided in three sections:

- Motivation
- Background
- Objectives

1.1 Motivation

In the field of aerospace and flight testing, accurate system identification plays a critical role in understanding and predicting the behavior of complex aircraft systems. The ability to model and analyze the dynamics of an aircraft is essential for various purposes, including flight control design, performance evaluation, and safety assessment. However, due to the inherent complexity and nonlinearity of aircraft systems and aerodynamics, traditional modeling approaches often fail to capture the intricacies of their behavior.

Traditional modeling techniques, such as linear regression or system identification based on parametric models, are limited by their assumptions of linearity and simplified relationships between input and output variables. These approaches struggle to account for the nonlinear and uncertain nature of real aircraft systems, leading to inaccurate predictions and suboptimal control strategies.

To overcome these limitations, advanced modeling techniques like Neuro-Fuzzy systems have gained significant attention in recent years. Neuro-Fuzzy combines the strengths of fuzzy logic and neural networks to handle complex and uncertain data, allowing for more accurate system identification and prediction, and it is important to emphasize that it is not a "black box" model.

The fuzzy logic component of Neuro-Fuzzy systems enables the representation and manipulation of linguistic variables and expert knowledge in a structured manner. It provides a flexible framework for capturing and reasoning about imprecise and uncertain information, making it particularly well-suited for modeling complex systems with vague or incomplete data.

In parallel, the neural network component of Neuro-Fuzzy systems excels at capturing non-linear relationships and mapping complex input-output patterns. By leveraging the learning capabilities of neural networks, Neuro-Fuzzy models can adapt and evolve based on the available data, improving their accuracy and robustness over time.

The application of Neuro-Fuzzy in system identification, particularly in the context of subscale flight testing and aerodynamic modeling, offers numerous benefits. It enables the development of more accurate and reliable models that capture the dynamics of aircraft systems under different operating conditions. These models can aid in flight control systems design, performance optimization, fault detection, and full-scale aircraft decision making.

Through this research, the author aims to explore the capabilities of Neuro-Fuzzy systems in system identification and subscale flight testing, providing valuable insights into their applicability, strengths, and limitations. By doing so, the contribution to the advancement of modeling techniques in aviation and open avenues for improved understanding and performance of full-scale aircraft systems.

1.2 Background

There are different approaches to investigate and build a reliable aerodynamic model within the system identification research domain, including CFD, wind tunnels, and flight testing. Although these approaches have proven their worth, they often require significant resources, time, and specialized knowledge.

In this context, Artificial Intelligence (AI) has emerged to play a key role. AI-based methods, such as machine learning and Neuro-Fuzzy systems, offer complementary help to reduce the resources required to build an aerodynamic model. The pioneers to use Artificial Neural Networks (ANN) as a tool in the aerodynamic research field were Rajkumar and Bardina (2002), where the authors used sparse data from an airfoil to identify the lift coefficient behavior in function of the angle of attack.

One of the most important flight test centers in the world is the NASA Langley Research Center in Virginia-USA shown in Fig. 1.1, which was founded in 1917 and is the first civilian aeronautical laboratory in the USA. An important study conducted there is presented by Brandon and Morelli (2012), where the authors used experimental data from a full-scale aircraft to train a neuro-fuzzy architecture to obtain a reliable aerodynamic model for the Aermacchi MB 326M Impala aircraft.

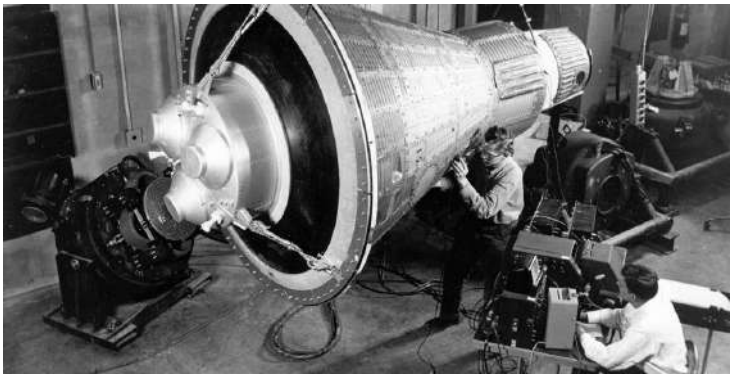

Figure 1.1: Engineers inspecting a capsule in Langley Research Center in 1960. Source: NASA.

Another memorable work was presented by Brandon and Morelli (2016), where the authors used orthogonal functions and Neuro-Fuzzy to predict the aerodynamic forces and moments with online on-board measurements of the input variables during the flight. The authors made a comparison between the two methods and the Neuro-Fuzzy performed good accuracy in the unsteady aerodynamic curve prediction.

The work published by Roy and Peyada (2017a) used Neuro-Fuzzy and Genetic Algorithm to describe the first Taylor series for the lateral forces and moments of the full-scale aircraft. The same authors also published the longitudinal aerodynamics of the same aircraft in the same year (ROY; PEYADA, 2017b). A comparison between Neuro-Fuzzy with Genetic Algorithm (NF-GA) and Neuro-Fuzzy with Differential Evolution (NF-DE) is presented in chapter 4.

Machine learning (ML) techniques have emerged as a promising approach to develop reliable aerodynamic models for full-scale or reduced-scale aircraft using numerical or experimental data. Tao and Sun (2019) presented a deep learning-based multi-fidelity approach applied to robust optimization for airfoils and wings under Mach number uncertainty. Another work using deep learning presented a high-precision nonlinear aerodynamic configuration analysis method, which according to the authors, is able to provide very good agreement for the pre- and post-stall aerodynamic behavior and generate the results in less time than intensive methods such as CFD (KARALI et al., 2021).

The ML techniques are also used to capture some special nonlinearities of the aerodynamic flow, such as the stall of the aircraft. The work presented by Tatar and Sabour (2020) is responsible to model this phenomenon using CFD data simulations of an airfoil using Neuro-Fuzzy and orthogonal functions.

Deep learning (DL) techniques are also used in aerodynamic modeling and optimization. For example, Li, Kou and Zhang (2022) used DL to model the aerodynamic distribution of a transonic wing, using numerical and experimental results to train the ANN. The authors consider that high-fidelity data is obtained experimentally, and low-fidelity data is obtained through numerical simulations, and they found that using only a small portion of high-fidelity data mixed with a large portion of low-fidelity data was sufficient to train a deep neural network (DNN) and obtain a good aerodynamic model.

The application of Neuro-Fuzzy in the context of subscale flight testing and system identification/simulation represents a significant and innovative approach among all the others found in the literature review. Therefore, this work focuses on using real-world data obtained from flight tests and other sources to comprehensively analyze and understand the aerodynamic performance of GFF under an open field unsteady flight condition.

1.3 Objectives

The Neuro-Fuzzy is a method widely applied to control studies, as the work presented by Carvalho et al. (2021). However, the objective of this study is to explore the application of Neuro-Fuzzy systems in the context of system identification and flight

testing for reduced scale aircraft. By exploiting the interpretability of fuzzy logic and the adaptive learning capabilities of neural networks, Neuro-Fuzzy models offer promising potential for accurately capturing the complex aerodynamic behavior of the aircraft.

To achieve this goal, different configurations of Neuro-Fuzzy architectures are tested and analyzed. These configurations include different combinations of input variables, membership function shapes, number of membership functions, number of output functions, optimization methods and inference methods, allowing the author to systematically evaluate their impact on model accuracy and performance. By conducting a comprehensive comparison of these configurations, the best Neuro-Fuzzy architecture tested that can effectively address the challenges posed by unsteady aerodynamic system identification was achieved and it is described in Section 4. Ultimately, this study aims to contribute to the advancement of modeling techniques in aviation by providing valuable insights into the suitability and effectiveness of Neuro-Fuzzy systems in addressing real-world subscale flight testing and aerodynamic modeling challenges.

This research uses experimental data from a reduced scale version (12% of the full scale) of a Generic Future Fighter (GFF) first designed by SAAB and the built by Linköping University (JOUANNET et al., 2012). The experimental data were collected from flight tests of a remote-controlled (RC) aircraft instrumented with a Pixhawk, a device for measuring the angle of attack and sideslip angle, and various other instruments. The instrumentation and data acquisition were performed by (RUEDA, 2021) at Linköping University (LiU), and these data were kindly made available to the author of this work. The Fig. 1.2 presents the reduced scale aircraft (GFF).

Figure 1.2: Generic Future Fighter (GFF). Source: Courtesy from Linköping University.

In order to clarify the objectives of this study and to give a better understanding of what will be approached in this document, the following diagram from Fig. 1.3 is presented to explain the main steps to achieve the final model.

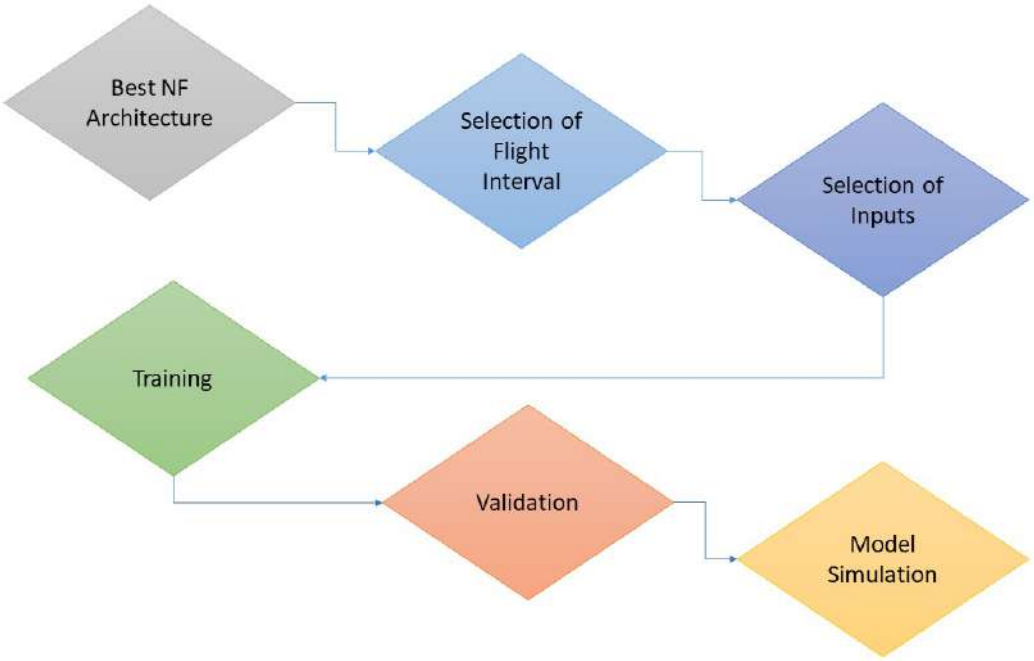

Figure 1.3: Step diagram of activities. Source: Author.

This study aims to present an innovative methodology to perform system identification of a reduced scale fighter aircraft using Neuro-Fuzzy with Differential Evolution. After the identification is done, a simulation based on the Neuro-Fuzzy results is presented in the Simulink environment.

In the next chapter of this paper, the basic theory of the applied machine learning techniques, aerodynamics and flight dynamics of aircraft will be presented.

Chapter 2

Theoretical Approach

This chapter contains an explanation of the methodology used in this document. First, the Fuzzy Logic theory is explained, followed by the Fuzzy Rule-based System (FRBS) with an explanation of the most used inference methods. Finally, the Neuro-Fuzzy, the Differential Evolution, and the Artificial Neural Networks are presented. Finally, the aerodynamic forces and moments of the aircraft are explained.

2.1 Fuzzy logic

The fuzzy logic can be used in the modeling of vast biological behaviors, like the growth of violets in the function of water and sunlight, as presented by Jafelice, Barros and Bassanezi (2012).

Fuzzy logic differs from the classical Boolean logic mainly because the latter can assume only assume two conditions, 0 or 1, while the first can assume several values varying between 0 and 1.

A simple example to illustrate fuzzy logic is the classification of people into the category of elderly. Depending on the jurisdiction, the law often designates individuals over the age of sixty as elderly. Using Boolean logic, only people who meet this exact age criterion are considered elderly. Fuzzy logic, however, introduces a different perspective by assigning a degree of membership that increases with age, as shown in Fig. 2.1.

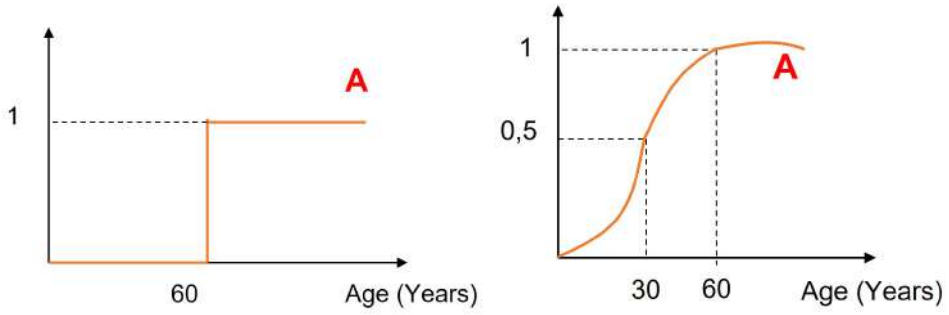

(a) Boolean Logic. (b) Fuzzy Logic.

Figure 2.1: Comparison between Boolean Logic and Fuzzy Logic. Source: Adapted from classes notation from Prof. João Alberto Fabro and André Schneider de Oliveira.

Based on this, it seems interesting to model a subscale aircraft using this mathematical approach. The logic can be well adapted to the flight dynamics of an aircraft. The following section gives a better idea of how Fuzzy Logic correlates the input variables with its outputs.

2.2 Fuzzy Rule-based System

The FRBS has four important structures to present, which can be described on the following items:

- **Input Processor**: The input processor converts real numbers into numbers with a certain degree of membership on fuzzy sets. This process is called fuzzification.
- **Rule Bases**: The rule bases are linguistic interpretations of the system's behavior and, together with the inference machine, can be considered the core of FRBS. They can be created by prepositions of the type `IF...THEN`, according to the expert knowledge. This step is responsible for establishing the relations between the linguistic variables.
- **Inference Machine**: The inference machine is responsible for establishing the association between the input fuzzy sets with the output fuzzy functions (Takagi-Sugeno method), and this association is guided by the rule bases. knowledge.
- **Output Processor**: The output processor is responsible for performing the defuzzification, i.e. converting the degree of membership of the fuzzy sets back to

real numbers.

The FRBS architecture can be seen in Fig. 2.2.

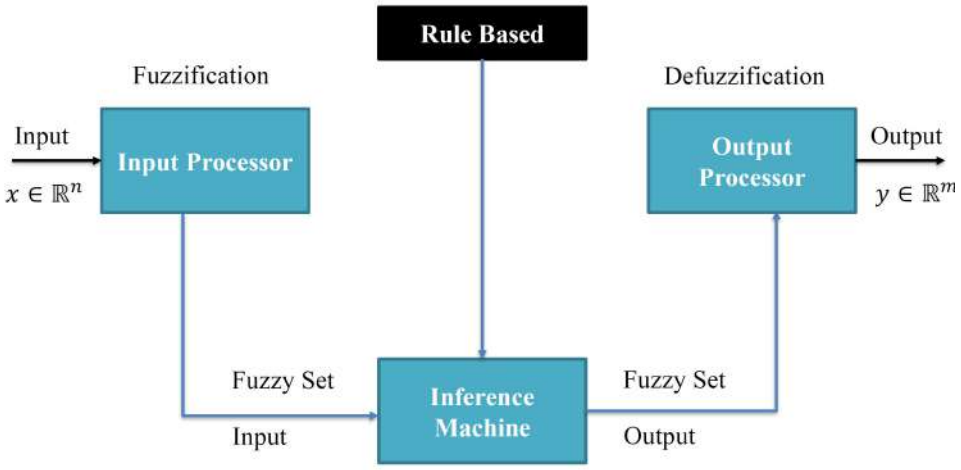

Figure 2.2: FRBS architecture. Source: Adpated from Pereira et al. (2017)

2.2.1 Mamdani Inference Method

According to Jafelice et al. (2004), the defuzzification in the Mamdani inference method is made through the sum of areas underneath the curve. The resulting area is analyzed and the answer of the system is the position of the centroid of the entire area. The example of Mamdani's inference method is shown in Fig. 2.3.

To describe the Mamdani inference method, it is necessary to propose two arbitrary rules:

Rule 1: If (X is A_1 AND Y is B_1) Then (Z is C_1)

Rule 2: If (X is A_2 AND Y is B_2) Then (Z is C_2)

The centroid for a continuous domain can be calculated using Eq. 2.1.

$$G(C) = \frac{\int_R u_i C(z_i)}{\int_R C(z_i)} \tag{2.1}$$

where R is the region of integration.

2.2.2 Takagi-Sugeno-Kang Inference Method

The TSK inference method manages the outputs as functions that depend on the input variables. The output functions have parameters that multiply the input variables.

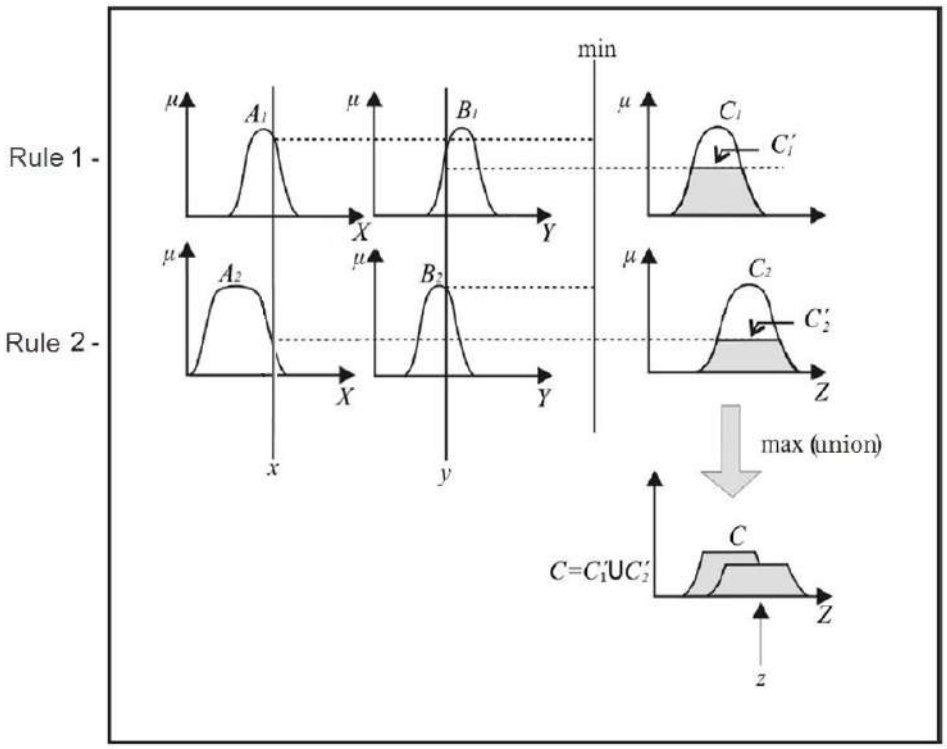

Figure 2.3: Mamdani inference method. Source: Adapted from Jafelice et al. (2003)

Fig. 2.4 shows how the TSK inference method works.

It is necessary to propose two arbitrary rules to describe the TSK inference method:

Rule 1: If (X is A_1 AND Y is B_1) Then (Z is z_1)

Rule 2: If (X is A_2 AND Y is B_2) Then (Z is z_2)

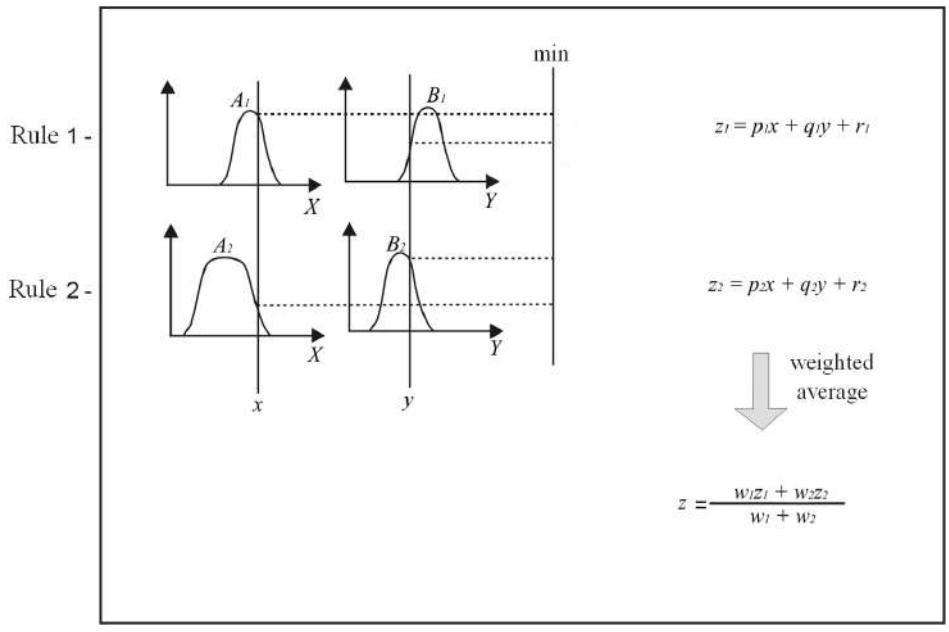

Figure 2.4: TSK inference method. Source: Adapted from Jafelice et al. (2003)

The defuzzification is done by a weighted average between the output functions multiplied by the weights estimated by the rule bases.

2.2.3 Pondered Individual Analysis

This inference method was first presented by Pereira, Jafelice and Finzi (2022), and it is very similar to the Mamdani inference method. Nevertheless, it does not have the area integration anymore, which gives this technique the ability to save some computational cost and the possibility to maintain a high interpretability of the linguistic variables.

The technique is based on the mathematical translation of each fuzzy proposition that composes the rule bases. According to Pereira, Jafelice and Finzi (2022), to perform the PIA method it is necessary to understand the following nine steps.

1. The definition of the FRBS inputs and outputs fuzzy sets, and the rule bases, have the same reasoning adopted in the Mamdani inference method.

2. The point where the membership function has the maximum value (one) is called the center point (CP). In case that exists a membership function with more than one CP, it is necessary to make an arithmetic mean between these points to identify the resultant CP.

3. For each fuzzy rule from FRBS, the effect of increasing or decreasing the input variable (IN) will perform a different effect on the output variable (OUT), according to what type of relationship they have, i.g. directly proportional or inversely proportional.

    - **Direct**: The representation when the input variable is directly proportional to the output variable will be IN **Dir** OUT.
    - **Inverse**: When the correlation between IN and OUT are inversely proportional, the representation will be IN **Inv** OUT.
    - **Neutral**: To conclude, when it is not possible to infer the relationship between IN and OUT, the representation will be IN **Neut** OUT.

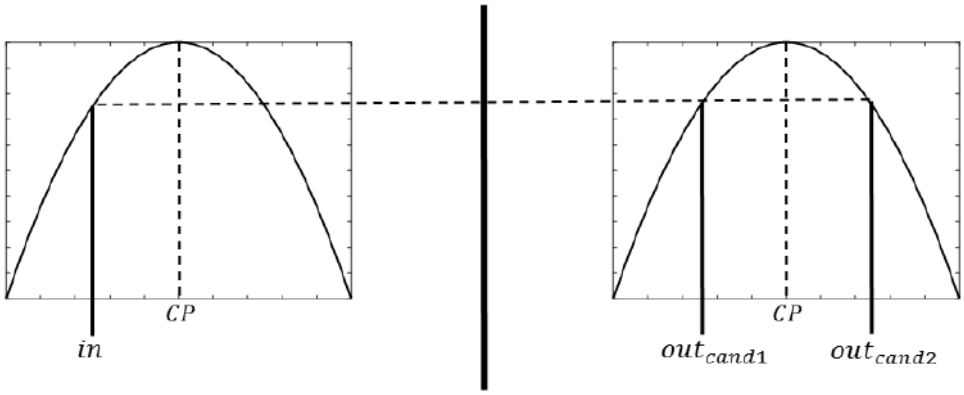

Figure 2.5: PIA inference method. Source: Pereira, Jafelice and Finzi (2022)

4. For any given input variable x_i that has a degree of membership equal to μ in a given membership function, the same degree of membership (μ) is projected onto the corresponding output variable (y_i) membership function according to the established rule base (R_i). See Figure 2.5. The projection will yield two possible output candidates, out_{cand1} and out_{cand2}.

5. In order to select the correct output candidate, it is necessary to consider the following conditions:

   - If in < CP and IN **Dir** OUT then $out = out_{cand1}$.
   - If in > CP and IN **Inv** OUT then $out = out_{cand1}$.
   - If in < CP and IN **Inv** OUT then $out = out_{cand2}$.
   - If in > CP and IN **Dir** OUT then $out = out_{cand2}$.
   - Other cases are threatened as an arithmetic mean between out_{cand1} and out_{cand2}.

6. The process is repeated for each input variable. With respect to the rule bases R_i, it is possible to define an output contribution $cont_{C_{jm}}$, according to Eq. 2.2, where C_j is the output fuzzy set, m is the number of times that C_j was already correlated in the rule base definition. Also, out_{k_i} is the selected output value and a_k is the weight associated with the output variable, both in terms of a k input variables. If all variables have the same effect on the output process, $a_k = 1$ is assumed.

$$cont_{C_{j_m}} = \frac{\sum_{k=1}^{n_{in}} a_k out_{k_i}}{\sum_{k=1}^{n_{in}} a_k} \tag{2.2}$$

7. The next step, after defining the contribution of each rule, is to calculate the value of the consequent function f_{C_j} of each output fuzzy set C_j. The Eq. 2.3 shows the calculation for the consequent function, where T_j is the sum of the rules associated with the set C_j.

$$f_{C_j} = \frac{\sum_{m=1}^{T_j} w_{C_{j_m}} cont_{C_{j_m}}}{\sum_{m=1}^{T_j} w_{C_{j_m}}} \tag{2.3}$$

8. To identify the weights, it is necessary to understand that the FRBS interprets the union as the minimum and the intersection as the maximum. Therefore, when a linguistic rule processes a condition with AND, the weight will be the larger value (max), and when the rule processes a condition with OR, the weight will be the smaller value (min). The Eq. 2.4 gives an example of the weight identification from any rule, where $w_{C_{j_m}}$ is the weight of each rule R_i and $W_{C_{j_m}}$ is the weight of each consequent function f_{C_j}.

$$W_{C_j} = max(w_{C_{j_m}}), m = 1, ..., T_j \tag{2.4}$$

9. Finally, the output of the FRBS can be obtained through defuzzification. For PIA, the defuzzification is done using the weighted mean method. The Eq. 2.5 shows the calculation, where n_C is the number of fuzzy sets from Z output.

$$z = \frac{\sum_{j=1}^{n_C} W_{C_j} f_{C_j}}{\sum_{j=1}^{n_C} W_{C_j}} \tag{2.5}$$

This section introduced the three fuzzy inference methods that will be evaluated in Section 4. The following section will introduce the first machine learning technique developed: Artificial Neural Network.

2.3 Artificial Neural Networks

This section presents the Artificial Neural Networks (ANN), which is a type of machine learning that mimics the structure and functions of the human brain, which was first described by McCulloch and Pitts (1943). ANNs are composed of interconnected processing units, or nodes/neurons, that work together to solve complex problems. Neurons are organized into layers, and the connections between neurons are defined by weights.

The most basic structure of an ANN consists of five structures:

- **Input Layer:** The input layer receives data or information from the outside world and passes it on to the next layer.
- **Hidden Layer:** The hidden layer processes the data by performing mathematical operations on the input data using the weights assigned to each neuron.
- **Output Layer:** The output layer produces the final result or prediction based on the information processed by the hidden layers.
- **Activation Function:** The activation function determines the output of each neuron in the hidden layer(s) and the output layer. It introduces nonlinearity into the network.
- **Bias:** The bias is an additional parameter that is added to each neuron to control the overall output of the network, helping to make the network more flexible and better able to adapt to different situations.

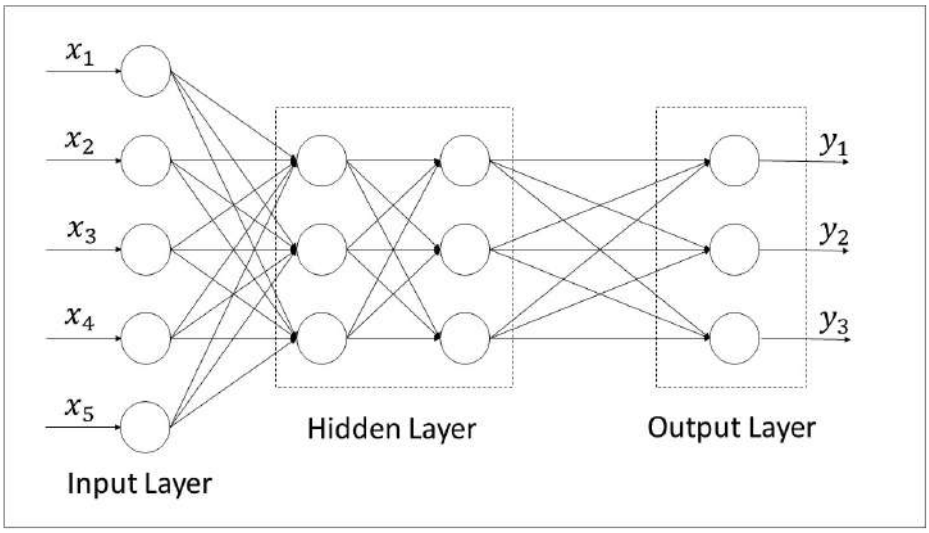

Figure 2.6: Arbitrary ANN architecture. Source: Adapted from Aggarwal et al. (2018)

The output from a neuron (Fig. 2.7) is given by Eq. 2.6 (AGGARWAL et al., 2018).

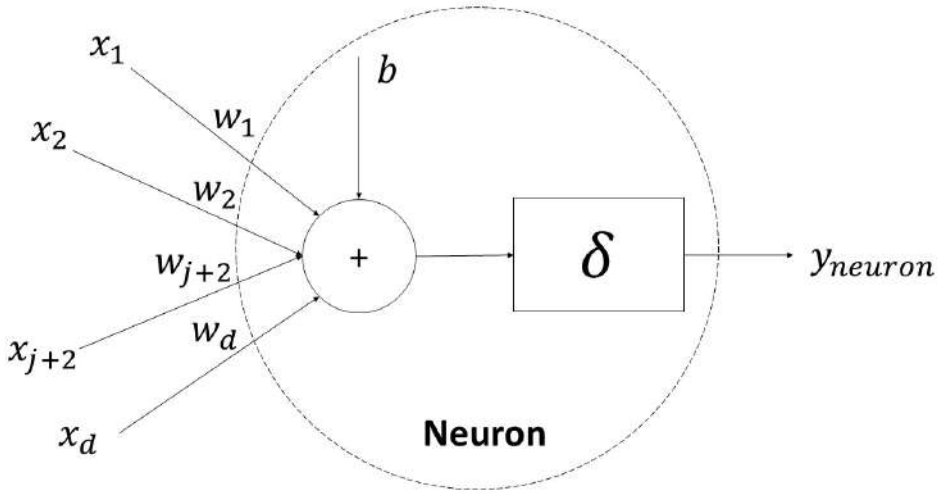

Figure 2.7: Neuron representation. Source: Adapted from Pereira et al. (2021)

$$y_{neuron} = \delta(\sum_{j=1}^{d} w_j x_j + b) \tag{2.6}$$

Where y_{neuron} is the output of the neuron, x_j is the input of node j, w_j is the weight associated with input j, d is the number of inputs, and b is the bias. According to Aggarwal et al. (2018), the activation functions can be represented by δ and it can assume different types of functions, e.g., sign, linear function, sigmoid, hyperbolic tangent, etc., see Fig. 2.8.

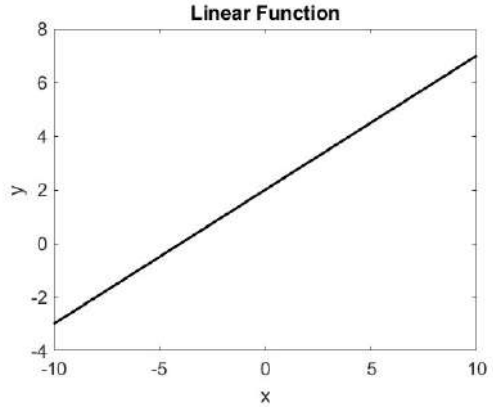

(a) Linear function

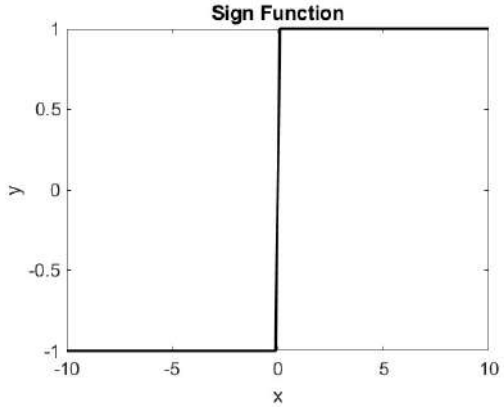

(b) Sign function

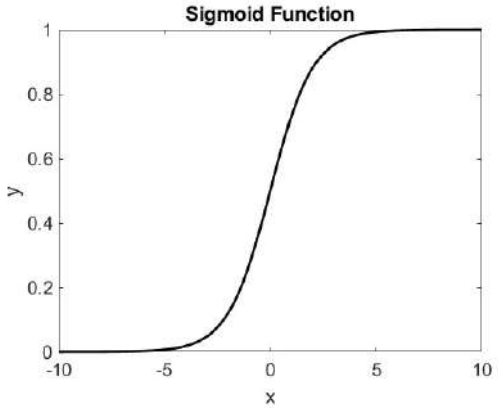

(c) Sigmoid function

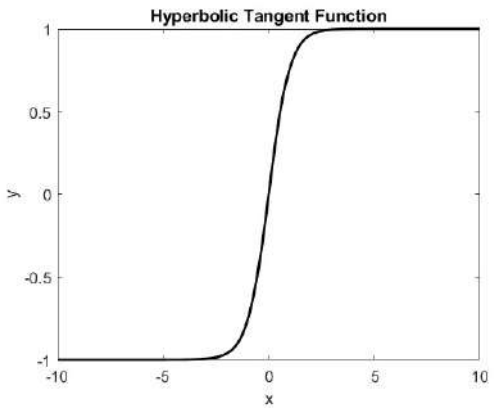

(d) Hyperbolic tangent function

Figure 2.8: Activation function examples. Source: Adapted from Aggarwal et al. (2018).

The ANN is been used in several engineering applications, although in the aerodynamics domain, the pioneers were Rajkumar and Bardina (2002), where the authors used sparse data of an airfoil to predict the entire lift coefficient curve.

2.4 Neuro-Fuzzy

In this section, the Neuro-Fuzzy architecture is presented, followed by the explanation of each layer separately. The Neuro-Fuzzy was first introduced by (JANG, 1993), and it is a combination of the interpretability of the Fuzzy Logic and the adaptability of the Artificial Neural Networks. In Fig. 2.9 it is possible to see the layers that compose the Neuro-Fuzzy architecture.

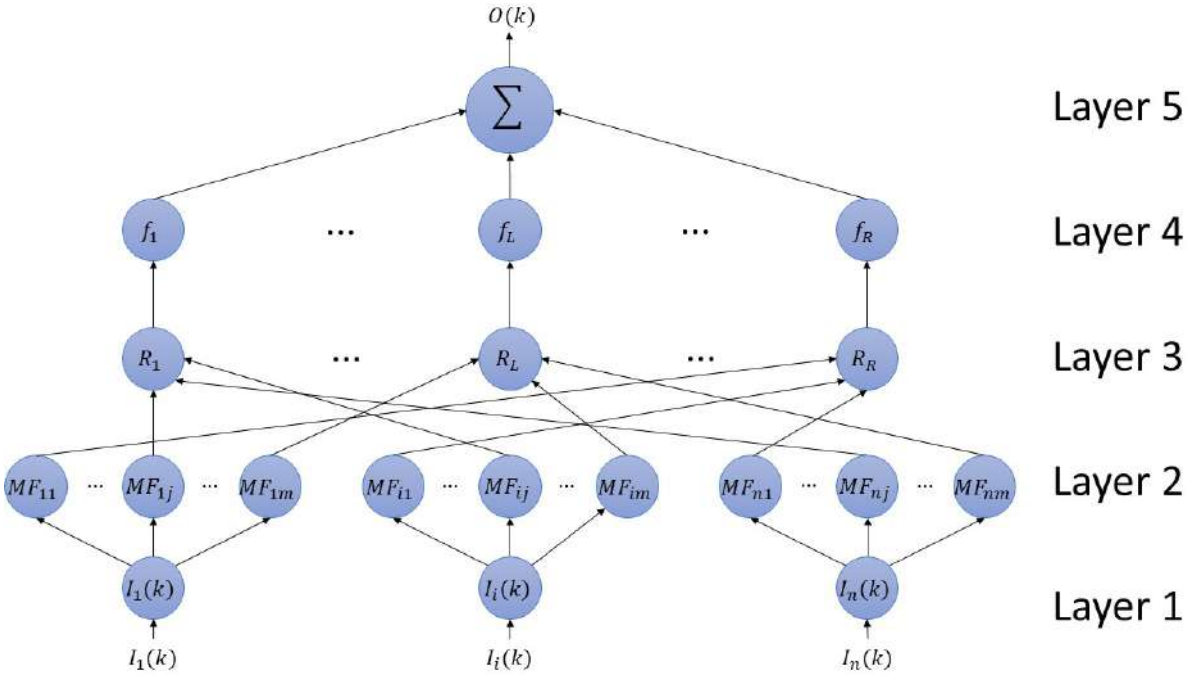

Figure 2.9: Neuro-Fuzzy based on Takagi-Sugeno inference method architecture. Source: Adapted from Pereira et al. (2017).

First Layer: Each node receives as input only one variable $I_i(k)$, in which is used in the training process. The output of the node i of the first layer at time k, $u_i^{(1)}(k)$, is given by:

$$u_i^{(1)}(k) = I_i(k) \tag{2.7}$$

Second Layer: In this layer the fuzzification of the input variables is performed, i.e. the real numbers are transformed into fuzzy subsets with a certain degree of pertinence. Membership functions (MF) are constructed to describe the inputs. Considering that the membership functions are approximated by Gaussian functions, the output of node ij of layer 2 at time k, $u_{ij}^{(2)}(k)$, is given by:

$$u_{ij}^{(2)}(k) = e^{-\frac{(u_i^{(1)}(k) - m_{ij}(k))^2}{2\sigma_{ij}^2(k)}} \tag{2.8}$$

where $m_{ij}(k)$ and $\sigma_{ij}^{(2)}(k)$ are the mean and standard deviation, respectively, of the Gaussian membership function MF_{ij}.

Third Layer: The propositions of the type IF...THEN... are implemented, forming the rule bases of the ANFIS. For each rule, the operators AND and OR are managed as minimum and maximum, respectively, so that output of the L node from this layer,

$u_L^{(3)}(k)$, is a function of the layer 2 for the selected output of rule R_L. The total number of rule bases for each system is defined by Eq. 6.1.

Fourth Layer: The nodes of this layer are known as consequent nodes, and they are defined as a function $f_L : R^n \rightarrow R$ where $f_L = f(I_1, ..., I_i, ..., I_n, w_{1L}, ..., w_{jL}, ..., w_{oL}, k)$, where $w_{1L}, ..., w_{jL}, \ ..., w_{oL}$ are weights that will be determined in the ANFIS training phase. The output of node L of layer 4, $u_L^{(4)}(k)$, is calculated by:

$$u_L^{(4)} = u_L^{(3)}(k) f_L(I_1, ..., I_i, ..., I_n, w_{1L}, ..., w_{jL}, ..., w_{oL}, k) \tag{2.9}$$

Fifth Layer: The last layer provides the ANFIS resultant answer and it is given by the equation:

$$O(k) = \frac{\sum_{L=1}^{R} u_L^{(4)}(k)}{\sum_{L=1}^{R} u_L^{(3)}(k)} \tag{2.10}$$

2.5 Optimization Methods

This section presents the optimization methods evaluated in the Neuro-Fuzzy training. The comparison between the optimization methods was performed using 600 MB of RAM memory dedicated to MATLAB, with a RAM speed equal to 2133 MHz (DDR4). The results obtained are presented in the Chapter 4.

2.5.1 Genetic Algorithm

Genetic algorithms (GA) are a type of evolutionary algorithm that is based on the natural selection of the species (HOLLAND, 1992). The idea of the GA is to create a population of candidate solutions, evaluate their fitness to the problem, and then apply genetic operators such as crossover and mutation to produce a new generation of solutions (population). The process is repeated until a satisfactory solution is found or a maximum number of 300 generations has been reached (Fig. 2.10).

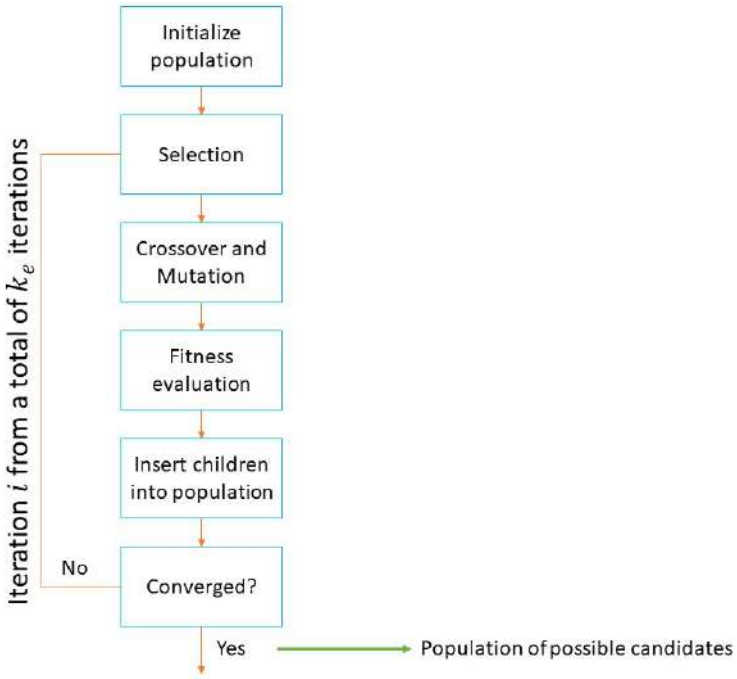

Figure 2.10: Genetic algorithm block architecture. Source: Author.

The parameters used in the genetic algorithm are shown in Tab. 2.1. The reinsertion rate is 1, which means that every time the weakest individual will be replaced.

Table 2.1: Parameters used in the Genetic Algorithm.

Optim. Parameters	Value
Population size	40
Maximum Generation	198
Mutation rate	0.06
Crossover rate	1
Reinsertion rate	1

2.5.2 Differential Evolution

Differential Evolution (DE) was first published by Storn and Price (1997) and since then it has been widely used by the scientific community. Because of that, this optimization methodology was chosen to optimize the Fuzzy Logic parameters.

According to Storn and Price (1997), the mutation probability (F) needs to be inside the interval $[0, 2]$ and the crossing probability (CR) $\in [0, 1]$, and the value selection has to be determined by the user. Therefore, the optimization parameters used to acquire the results can be seen in Tab. 2.2.

Using the DE optimization method to train the Neuro-fuzzy parameters, it took less

Table 2.2: Optimization parameters used in the Differential Evolution.

Optim. Parameters	Value
Number of individuals	150
Number of variables	17-25
Crossing probability (CR)	0.95
Mutation probability (F)	0.4

than a minute (30 seconds) to optimize seventeen variables using more than three hundred data. The Fig. 2.11 depicts the simplified architecture of the differential evolution applied in this work.

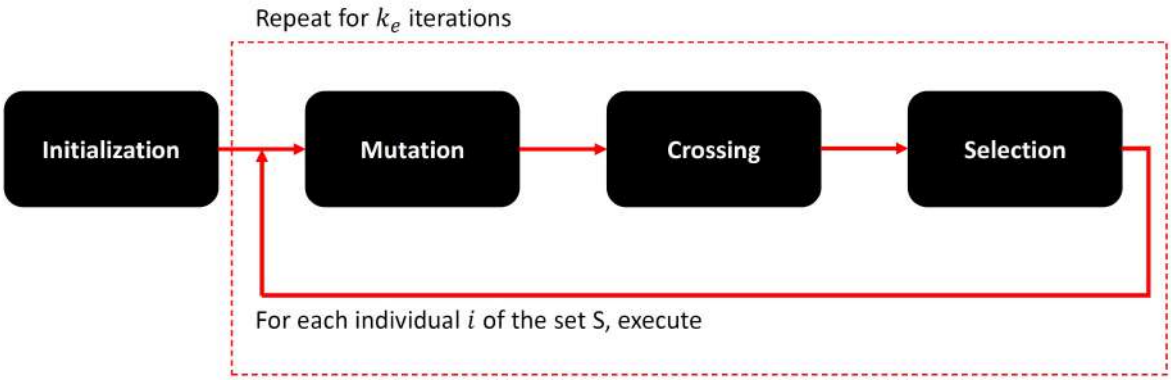

Figure 2.11: Simplified representation of the differential evolution. Source: Author.

2.5.3 Complex-RF

The Complex is an optimization method based on the simplex method (SPENDLEY; HEXT; HIMSWORTH, 1962), that had been evolved through different contributions, and the final modification made by Krus et al. (2003) includes a randomization factor (β) and a forgetting factor (γ), becoming the Complex RF. According to Braun and Krus (2017), the Complex RF basic procedure is divided in 12 steps.

1. Generate $k = 2n$ test points.
2. Apply a forgetting factor: $f(\mathbf{x}_i) = f(\mathbf{x}_i) + [1.0 - (0.5\alpha_{RF})^{\gamma/k}][\max(f) - \min(f)]$.
3. Sort the points by their objective values: $f(0.6cm_1) \leq f(0.6cm_2) \leq \cdots \leq f(0.6cm_k)$.
4. Calculate the centroid $\mathbf{x}_c$ of points $0.6cm_1, 0.6cm_2, \ldots, 0.6cm_{k-1}$.

5. Calculate the reflected point $0.6cm_k = 0.6cm_c + \alpha_{RF}(0.6cm_c - 0.6cm_k) + \beta x_R \max(\Delta x/\Delta x_R)\mathrm{rand}(-0.5, 0.5)$.
6. If no constraints are violated and $f(0.6cm_k) \leq f(0.6cm_{k-1})$: Go to step 2.
7. Define $n_c = 0$.
8. Define $a = 1 - e^{-n_c/5}$.
9. Calculate the contracted point $0.6cm_k = [(0.6cm_c)(1-a)+(0.6cm_1)a+(0.6cm_k)]/2$.
10. If $f(0.6cm_k) \leq f(0.6cm_{k-1})$: Go to step 2.
11. Increase n_c by 1.
12. Go to step 8.

Where α_{RF} is the reflection factor and k is the number of points. For a problem with n design variables, $\alpha_{RF} = 1.3$ and $k = 2n$ provide good results (BOX, 1965).

According to Braun and Krus (2017), Δx is a vector that carries the uncertainties for each design variable, which contains the difference between its highest and lowest value. The x_R contains the range between the upper and lower limits for each input variable. The forgetting factor is responsible to guarantee that the complex consists predominantly of recently evaluated points, and the random factor is responsible to increase the escaping chance from local optima, creating momentum to cross flat areas of objective functions.

2.6 Aircraft Aerodynamics and Flight Dynamics

In this section, the forces and moments that acts on the center of gravity of a remote-controlled (RC) subscale Generic Future Fighter (GFF), illustrated in Fig. 2.12, are explained. The presenting aircraft is a 13% scale aircraft, designed and built in Linköping University (JOUANNET et al., 2012). This remote controlled (RC) reduced scale aircraft conceptual design was developed by Saab Aeronautics.

Figure 2.12: Generic Future Fighter RC subscale model. Source: Courtesy of Linköping University.

The dimensions and mass characteristics of the GFF can be observed in Tab. 2.3. Every parameter from that table is written in the SI units.

Table 2.3: GFF mass characteristics and geometry. Source: Linköping University.

Parameter	**Value**
Wing span (b) $[m]$	1.470
Mean aerodynamic chord ($\bar{c}$) $[m]$	0.754
Aspect ratio (A) [-]	2.345
Wing reference area (S) $[m^2]$	0.921
Maximum takeoff weight (MTOW) $[kg]$	19.200
Operating empty mass $[kg]$	15.880
Moment of inertia about X-axis (I_{XX})) $[kgm^2]$	0.560
Moment of inertia about Y-axis (I_{YY})) $[kgm^2]$	5.280
Moment of inertia about Z-axis (I_{ZZ})) $[kgm^2]$	5.560

To better explain the 6-DOF (see Fig. 2.13) of the aircraft, the same can be decoupled into two important axis, the Longitudinal axis and the Lateral-Directional axis. Each of them has three degrees of freedom.

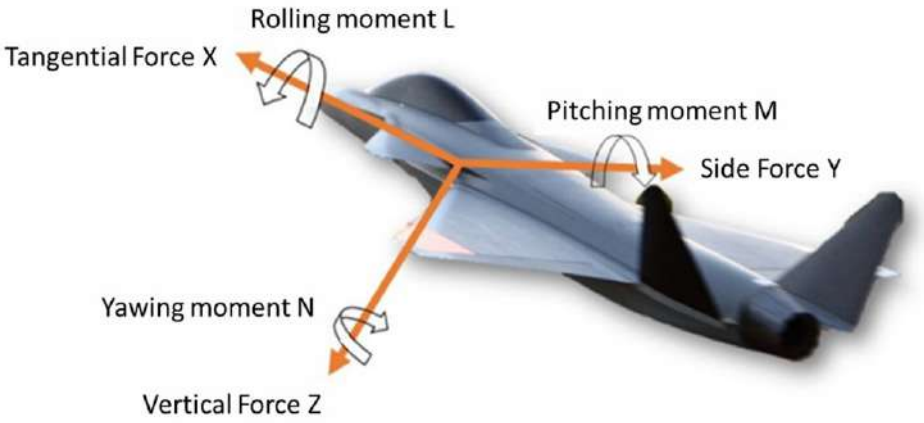

Figure 2.13: GFF body axis six degrees of freedom. Source: Courtesy of Linköping University and Author.

2.6.1 Longitudinal

Longitudinal aircraft forces and moments are crucial for the aerodynamic model. Their forces and moments are typically aligned with the flight direction (wind axis). The most well-known and important force is the aerodynamic lift (Eq. 2.11), which is generated by the wings and acts perpendicular to the direction of flight. Lift is the responsible force to keep the aircraft in the air and can vary according to the variation of the wing shape, airfoil, angle of attack, and more. The lift force can be calculated using the following equation (ROSKAM, 1998).

$$L_F = C_L \overline{q} S \tag{2.11}$$

Where C_L is the total airplane lift coefficient, $\overline{q}$ is the dynamic pressure and S is the reference wing area. Besides the variables included in the lift equation, according to Anderson (1999), it also depends on the angle-of-attack, control surfaces deflections, and Mach number or Reynolds number (Eq. 2.12).

$$Re = \frac{\rho_\infty V_\infty c}{\mu_\infty} \tag{2.12}$$

Another important force is the drag, which acts in the opposite way of the relative wind, and perpendicular to the lift force. The drag caused by the resistance of the air as the aircraft moves forward is called parasite drag, which is mainly dependent on

the aircraft's shape. Also, the drag is directly influenced by the amount of lift, which is called the induced drag. The total drag is the sum of the induced drag and the parasite drag and it can be seen in Eq. 2.13 (ROSKAM, 1998).

$$C_D = \overline{C}_{D_0} + \frac{C_L^2}{\pi A e} \tag{2.13}$$

Where: $\overline{C}_{D_0}$ is the drag due to aircraft's shape, C_L is the lift coefficient, A is the wing aspect ratio and e is Oswald's efficiency factor. Like lift force, the drag force also depends on the control surface deflections, angle-of-attack, and Mach number or Reynolds number.

In addition to these forces, there are also longitudinal moments that act around the aircraft's center of gravity. The most important is the pitching moment, which is a rotation of the aircraft around its lateral axis and, to be more precise, it happens around the aircraft's Y-axis. In the case of the GFF, the pitching moment is controlled by the ailerons, which can be deflected in the same direction (acting as elevators) and are located at the trailing edge of the delta wings, see Fig. 2.14. In addition, when the ailerons are acting as elevators, the canard is also deflected in the opposite direction to supplement the pitching moment around the center of gravity.

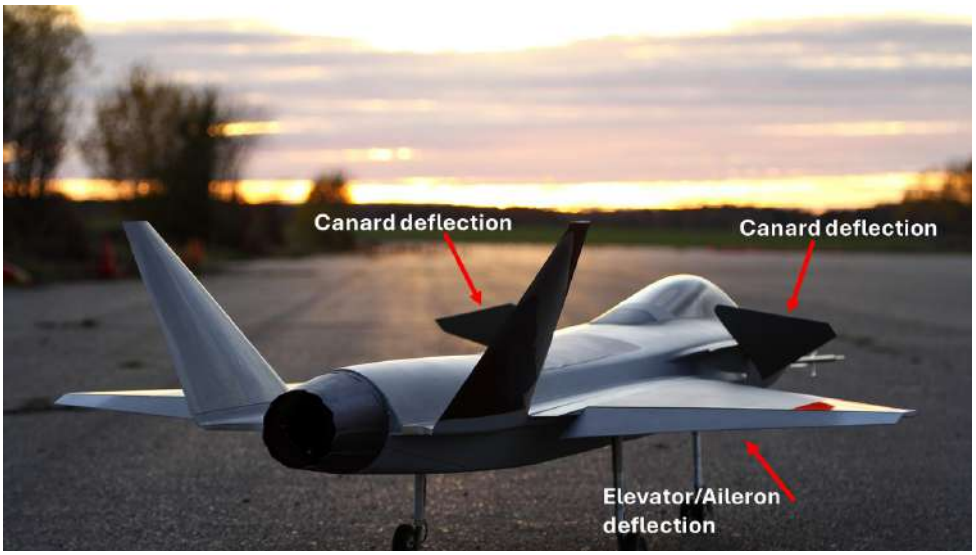

Figure 2.14: Illustration of GFF's elevator and canard deflection.

The 3-DOF encompassed by the aircraft's Longitudinal non-inertial body axis are: Tangential force, Pitching moment (Y-axis moment), and Vertical force. The Eq. 2.14 (ROSKAM, 1998) shows how these forces and moment are calculated.

$$\begin{bmatrix} F_X - T \\ M \\ F_Z \end{bmatrix} = \begin{bmatrix} C_X \frac{1}{2}\rho V^2 S \\ C_m \frac{1}{2}\rho V^2 S \bar{c} \\ C_Z \frac{1}{2}\rho V^2 S \end{bmatrix} \tag{2.14}$$

Where ρ is the air's specific mass, S is the reference wing area, V is the relative wind velocity, and $\bar{c}$ is the mean aerodynamic chord.

The forces in X-axis and Z-axis can be obtained through accelerometer measurements (FOSSEN, 2011), but the moments need to be calculated using the gyroscope information. The Eq. 2.15 is showing how to acquire the pitching moment using gyroscope information. The following equation is going to be used to calculate the GFF's pitching moment around its center of gravity.

$$M = (I_{XX} - I_{ZZ})pr + I_{XZ}(p^2 - r^2) + I_{YY}\dot{q} \tag{2.15}$$

On the equation above, it is necessary to perform the derivative of the q (pitching rate). The derivative is acquired using a high-pass filter, and it is better explained in Chapter 3.

$$\begin{bmatrix} C_X \\ C_m \\ C_Z \end{bmatrix} = \begin{bmatrix} C_{X_0} + C_{X_\alpha}\alpha + \frac{\bar{c}}{2V}C_{X_{\dot{\alpha}}}\dot{\alpha} + C_{X_{\delta_E}}\delta_E + C_{X_{\delta_C}}\delta_C + \frac{\bar{c}}{2V}C_{X_q}q \\ C_{m_0} + C_{m_\alpha}\alpha + \frac{\bar{c}}{2V}C_{m_{\dot{\alpha}}}\dot{\alpha} + C_{m_{\delta_E}}\delta_E + C_{m_{\delta_C}}\delta_C + \frac{\bar{c}}{2V}C_{m_q}q \\ C_{Z_0} + C_{Z_\alpha}\alpha + \frac{\bar{c}}{2V}C_{Z_{\dot{\alpha}}}\dot{\alpha} + C_{Z_{\delta_E}}\delta_E + C_{Z_{\delta_C}}\delta_C + \frac{\bar{c}}{2V}C_{Z_q}q \end{bmatrix} \tag{2.16}$$

Each component from Eq. 2.16 is a partial derivatives of the coefficient by the analyzed state variable. According to Etkin and Reid (1995), the Eq. 2.16 can be rewritten substituting every stability derivative for its partial derivative form. The Eq. 2.17 presents the longitudinal forces and moments coefficient in function of non-dimensional stability derivatives.

$$\begin{bmatrix} C_X \\ C_m \\ C_Z \end{bmatrix} = \begin{bmatrix} C_X = C_{X_0} + \frac{\partial C_X}{\partial \alpha}\alpha + \frac{\partial C_X}{\partial \dot{\alpha}}\frac{\dot{\alpha}\bar{c}}{2V} + \frac{\partial C_X}{\partial \delta_E}\delta_E + \frac{\partial C_X}{\partial \delta_C}\delta_C + \frac{\partial C_X}{\partial q}\frac{q\bar{c}}{2V} \\ C_m = C_{m_0} + \frac{\partial C_m}{\partial \alpha}\alpha + \frac{\partial C_m}{\partial \dot{\alpha}}\frac{\dot{\alpha}\bar{c}}{2V} + \frac{\partial C_m}{\partial \delta_E}\delta_E + \frac{\partial C_m}{\partial \delta_C}\delta_C + \frac{\partial C_m}{\partial q}\frac{q\bar{c}}{2V} \\ C_Z = C_{Z_0} + \frac{\partial C_Z}{\partial \alpha}\alpha + \frac{\partial C_Z}{\partial \dot{\alpha}}\frac{\dot{\alpha}\bar{c}}{2V} + \frac{\partial C_Z}{\partial \delta_E}\delta_E + \frac{\partial C_Z}{\partial \delta_C}\delta_C + \frac{\partial C_Z}{\partial q}\frac{q\bar{c}}{2V} \end{bmatrix} \tag{2.17}$$

2.6.2 Lateral-Directional

Lateral-directional forces and moments are critical aspects of aircraft stability and control. They are responsible for controlling the aircraft's movement along those axes, which correspond to the roll, lateral force, and yaw movements of the aircraft.

Lateral forces are those acting perpendicular to the longitudinal axis of the aircraft and are generated primarily by the wings. When the aircraft rolls, the wings generate different lift forces that are no longer aligned with the aircraft's center of gravity, resulting in a lateral force. This lateral force is opposed by the ailerons, which are control surfaces located at the trailing edge of the wings. By deflecting the ailerons in opposite directions, the pilot can control the lateral force and initiate a roll. In the GFF, the ailerons work as elevators as well, when they are deflected in the same direction.

Directional forces are those acting perpendicular to both the longitudinal and lateral axes of the aircraft and are generated primarily by the aircraft's vertical tail. Usually, the rudder is used in take-off and landing to better control the aircraft. During the flight, the yaw moment are control only with the ailerons, which is the GFF's case.

The longitudinal, lateral, and directional forces can be decomposed in forces around the non-inertial body axis of the aircraft (F_X, F_Y, F_Z) (FOSSEN, 2011). This operation converts the wind axis orientation to the aircraft's body axis orientation and it is not necessary to apply in the data acquired for the GFF, see Chapter 3. The rotation matrix is described by Eq. 2.18.

$$p^{body} = \begin{bmatrix} cos(\alpha)cos(\beta) & -cos(\alpha)sin(\beta) & -sin(\alpha) \\ sin(\beta) & cos(\beta) & 0 \\ sin(\alpha)cos(\beta) & -sin(\alpha)sin(\beta) & cos(\alpha) \end{bmatrix} p^{wind} \tag{2.18}$$

In addition to the lateral and directional forces, aircraft also experience lateral and directional moments, which are responsible for controlling the aircraft's rotational motion along these axes. Similarly to the pitch moment, the lateral and directional moments need to be calculated using the Pixhawk gyroscope data. The lateral moment (Eq. 2.19) is generated primarily by the ailerons, which produce a differential lift between the two wings, resulting in a rolling moment.

$$L = I_{XX}\dot{p} - I_{XZ}(\dot{r} + pq) + (I_{ZZ} - I_{YY})qr \tag{2.19}$$

The directional moment (Eq. 2.20) is generated primarily by the rudder, which produces a side force that acts at a distance from the aircraft's center of gravity, resulting in a yawing moment.

$$N = I_{ZZ}\dot{r} - I_{XZ}\dot{p} + (I_{YY} - I_{XX})pq + I_{XZ}qr \tag{2.20}$$

The GFF has a V-tail configuration, and the rudders are barely used. The entire lateral and directional forces and moments are controlled mainly by the deflection of the ailerons.

The 3 DOF that belongs to the aircraft's Lateral-Directional axis are: roll moment (moment around X-axis), Y force, and yaw moment (moment around Z-axis), and can be observed in Fig. 2.13. According to Roskam (1998), the forces and moments can be written as:

$$\begin{bmatrix} L \\ F_Y \\ N \end{bmatrix} = \begin{bmatrix} C_l \frac{1}{2}\rho V^2 Sb \\ C_Y \frac{1}{2}\rho V^2 S \\ C_n \frac{1}{2}\rho V^2 Sb \end{bmatrix} \tag{2.21}$$

Where b is the GFF wing span.

The forces and moments coefficients can be written in the first order of the Taylor series (ROSKAM, 1998). For the Lateral-Directional axis, the most correlated variables for the GFF are sideslip angle, sideslip angle rate, aileron deflection, and canard deflection.

$$\begin{bmatrix} C_l \\ C_Y \\ C_n \end{bmatrix} = \begin{bmatrix} C_{l_0} + C_{l_\beta}\beta + \frac{b}{2V}C_{l_{\dot{\beta}}}\dot{\beta} + C_{l_{\delta_A}}\delta_A + \frac{b}{2V}C_{l_p}p + \frac{b}{2V}C_{l_r}r \\ C_{Y_0} + C_{Y_\beta}\beta + \frac{b}{2V}C_{Y_{\dot{\beta}}}\dot{\beta} + C_{Y_{\delta_A}}\delta_A + C_{Y_\alpha}\alpha \\ C_{n_0} + C_{n_\beta}\beta + \frac{b}{2V}C_{n_{\dot{\beta}}}\dot{\beta} + C_{n_{\delta_A}}\delta_A + \frac{b}{2V}C_{n_p}p + \frac{b}{2V}C_{n_r}r \end{bmatrix} \tag{2.22}$$

Note that not every stability derivative from Eq. 2.22 is going to be used to train the Neuro-Fuzzy technique, only the high correlated variables are going to be selected. The non-dimensional stability derivatives (ETKIN; REID, 1995) are going to be obtained through Eq. 2.23 in Chapter 6.

$$\begin{bmatrix} C_l \\ C_Y \\ C_n \end{bmatrix} = \begin{bmatrix} C_{l_0} + \frac{\partial C_l}{\partial \beta}\beta + \frac{\partial C_l}{\partial \dot{\beta}}\frac{\dot{\beta}b}{2V} + \frac{\partial C_l}{\partial \delta_A}\delta_A + \frac{\partial C_l}{\partial p}\frac{bp}{2V} + \frac{\partial C_l}{\partial r}\frac{br}{2V} \\ C_{Y_0} + \frac{\partial C_Y}{\partial \beta}\beta + \frac{\partial C_Y}{\partial \dot{\beta}}\frac{\dot{\beta}b}{2V} + \frac{\partial C_Y}{\partial \delta_A}\delta_A + \frac{\partial C_Y}{\partial \alpha}\alpha \\ C_{n_0} + \frac{\partial C_n}{\partial \beta}\beta + \frac{\partial C_n}{\partial \dot{\beta}}\frac{\dot{\beta}b}{2V} + \frac{\partial C_n}{\partial \delta_A}\delta_A + \frac{\partial C_n}{\partial p}\frac{bp}{2V} + \frac{\partial C_n}{\partial r}\frac{br}{2V} \end{bmatrix} \tag{2.23}$$

At the end of the Longitudinal and Lateral-Directional modeling, it is expected that the Neuro-Fuzzy model can identify the most important stability derivatives for the GFF.

Chapter 3

Data Analysis

This chapter presents the methodologies used to obtain a reliable and smooth signal that accurately describes the aircraft's behavior during flight. Additionally, this chapter is going to elucidate the process of determining the training and validation intervals for each output variable, providing a rationale for these choices.

For general system measurements, it is common to have unlike noise with the acquired data. According to Larsson (2019), the input and output measurements of a system can be expressed in Eq. 3.1.

$$\begin{aligned} \dot{x}(t) &= a(x(t), u(t), w(t); \theta) \\ y(t) &= c(x(t), u(t), v(t); \theta) \end{aligned} \tag{3.1}$$

Where $x(t)$ is a $n_x \times 1$ state vector, $u(t)$ is a $n_u \times 1$ input vector and $w(t)$ is the modeled process noise. The nonlinear continuous function a describes the dynamic model, which can be considered as the Neuro-Fuzzy in this case. The output $y(t)$ is a $n_y \times 1$ vector and $v(t)$ is the modeled measurements noise.

The objective of the measured data is to describe a real system using a computational model, in other words, to create a system identification tool capable of simulating the GFF on MatLab, like illustrated in Fig. 3.1.

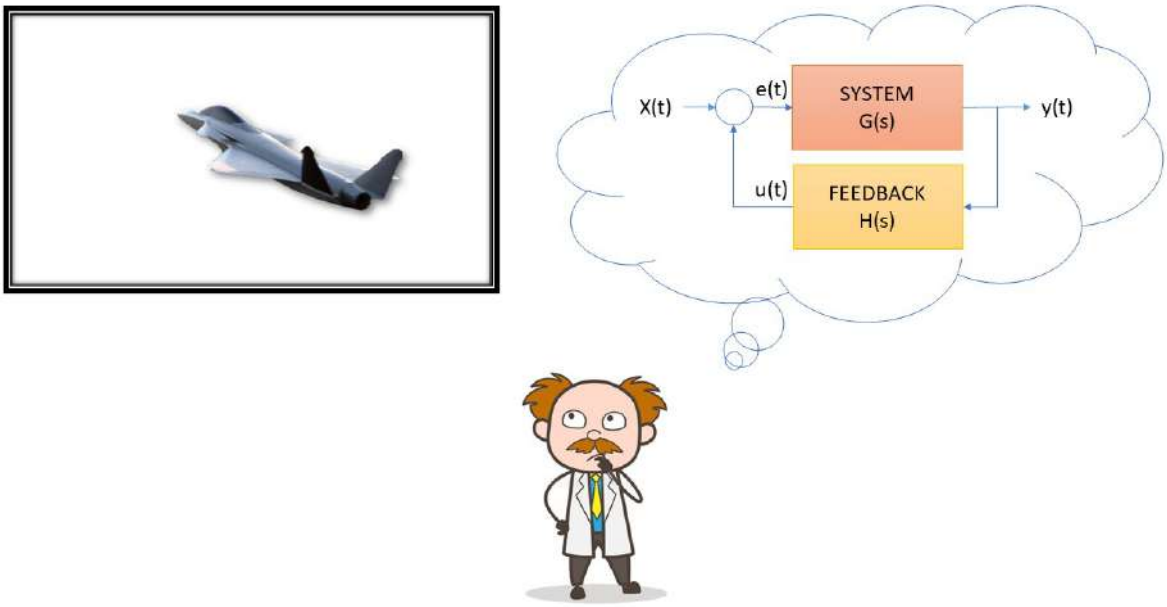

Figure 3.1: Exemplification of a system identification. Source: Author.

3.1 Aerodynamic Data Acquisition

According to Fossen (2011), the forces in the X-axis, Y-axis, and Z-axis can be obtained through the signals recorded by the accelerometers of an Inertial Measurement System (IMU). However, the moments have to be calculated using the Eq. 2.15, 2.19 and 2.20.

In this section, the embedded systems in the GFF that are required to acquire the complete aerodynamic model will be presented.

3.1.1 GFF instrumentation

This work uses the GFF data, which was acquired with a Pixhawk embedded in the aircraft, see (LUNDSTRÖM et al., 2016). Typically, the sample acquisition rate from a Pixhawk's IMU is 50 Hz. However, in this study, the onboard GFF's IMU acquisition frequency was increased by removing the automatic and control code, allowing all processing efforts to be dedicated to acquiring data. As a result, the sample rate was increased from 50 Hz to 100 Hz. Figure 3.2 shows the cockpit of the subscale aircraft with the Pixhawk inside.

Figure 3.2: GFF embedded systems. Source: Courtesy from Linköping University.

The GFF also has a nose-boom which contains a pitot-static tube and two flow-direction transducers, one for angle-of-attack (α) measurements and the other one for sideslipe angle (β) measurements (SOBRON et al., 2016). The Fig. 3.3 shows the system for acquiring the aerodynamic angles.

Figure 3.3: GFF nose-boom visualization. Source: Courtesy from Linköping University.

3.2 Filtering

This section has the objective to identify and remove unwanted noise. For that, the Fast Fourier Transform (FFT) of the IMU (Inertial Measurement Unit) was performed to verify the filter's frequency. As the name says, the IMU acquires the signal in a quasi-steady state (inertial), therefore the frequencies above 10 Hz are unwanted in

this case.

3.2.1 Lowpass Filter

The transfer function of the lowpass filter is shown in Eq. 3.2.

$$G_{lowpass} = \frac{1}{(s/\omega_f)^2 + 2\sigma_f/\omega_f + 1} \tag{3.2}$$

Where ω_f is the cut band or passband frequency and σ_f is the filter damping. The cut band frequency and the damping in this case were 10 Hz and 0.7 respectively. The lowpass filter response is ilustrated in Fig. 3.4.

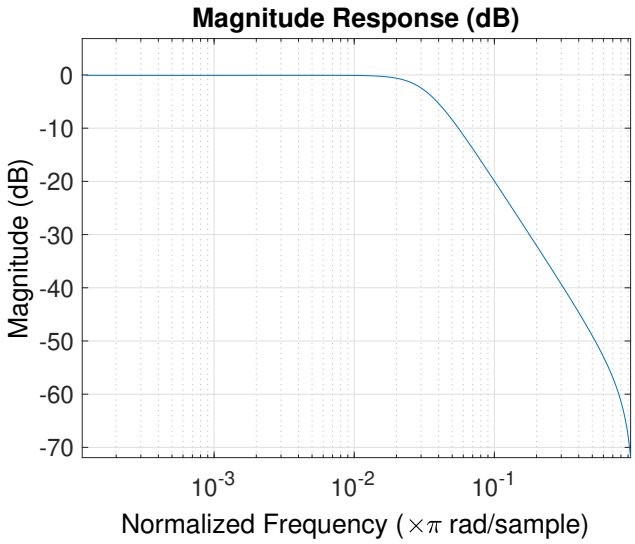

Figure 3.4: Lowpass filter magnitude response. Source: Author.

The raw signal is a noisy response of the GFF movements during the flight. In order to eliminate the noise, the lowpass filter is applied to every variable that is going to be inserted in the Neuro-Fuzzy box. Figure 3.5 shows the Fast Fourier Transform (FFT) for the Z-axis accelerometer signal with and without the lowpass filter.

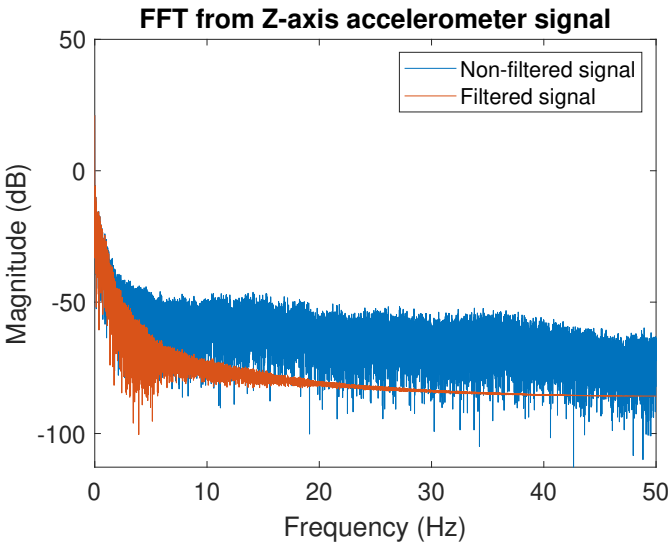

Figure 3.5: FFT of the GFF Z-axis accelerometer signal. Source: Author.

3.2.2 Highpass Filter

To obtain a signal derivative, it is used a first-order highpass filter or a band pass filter like presented in Fig. 3.6. The filter's equation is described in Eq. 3.3.

$$G_{highpass} = \frac{s}{(s/\omega_f)^2 + 2\sigma_f/\omega_f + 1} \tag{3.3}$$

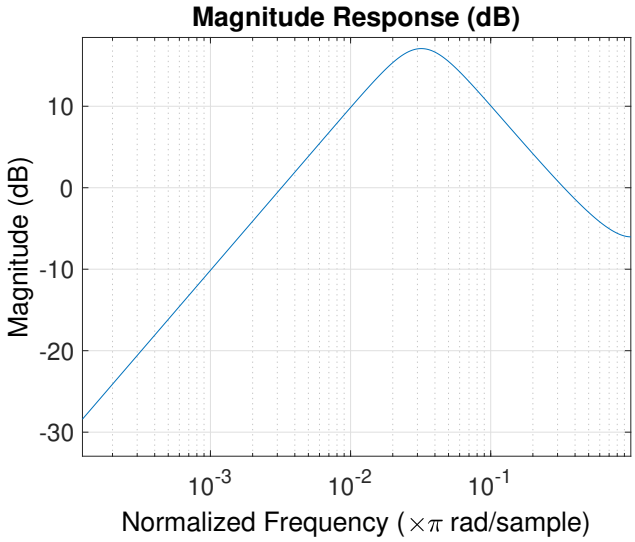

Figure 3.6: Highpass filter magnitude response. Source: Author.

After filtering all the input and output variables, it is expected to have them all in the same phase, avoiding signal delay problems.

3.3 Data Selection

In this section, the author separate the useful data into two sets: training and validation. The training set will comprise 35,000 data samples, while the validation set will comprise 11,000 data samples.

The size of the data consist on 94,605 data samples with an acquisition frequency of 100 Hz. The total time that the Pixhawk stayed in the armed mode was 946 seconds. The useful data is between 25,000 up to 75,000. Figure 3.7 shows the useful data interval.

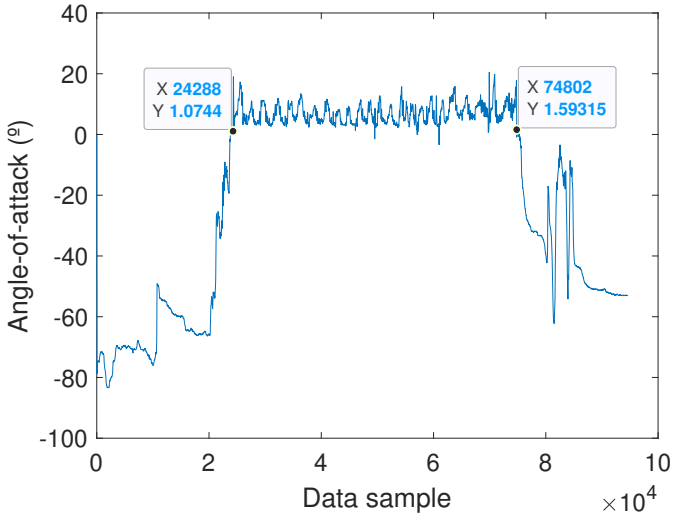

Figure 3.7: GFF angle-of-attack sampling data. Source: Author.

To enhance the training process, the author calculates the Person's Correlation Coefficient (PCC) as shown in Eq. 3.4 to evaluate the correlation between the input and output variables. A high correlation between these variables is crucial to achieve a higher coefficient of determination (R^2) (BRANDON; MORELLI, 2016). Therefore, by analyzing the PCC values, we can identify which input variables are more strongly correlated with the output variable and select them for training, which ultimately leads to a more accurate model.

$$r = \frac{\sum_{i=1}^{n}(x_i - \overline{x})(y_i - \overline{y})}{\sqrt{\sum_{i=1}^{n}(x_i - \overline{x})^2 \sum_{i=1}^{n}(y_i - \overline{y})^2}} \tag{3.4}$$

The training set was carefully selected to guarantee that none of the validation set will extrapolate the training set. The training data consists of an amount of 35,000 data sample that is from 39,000 until 74,000. The validation data is in the interval from

27,000 until 38,000, consisting of a sample of 11,000 data. Figure 3.8 highlights the training and validation sets.

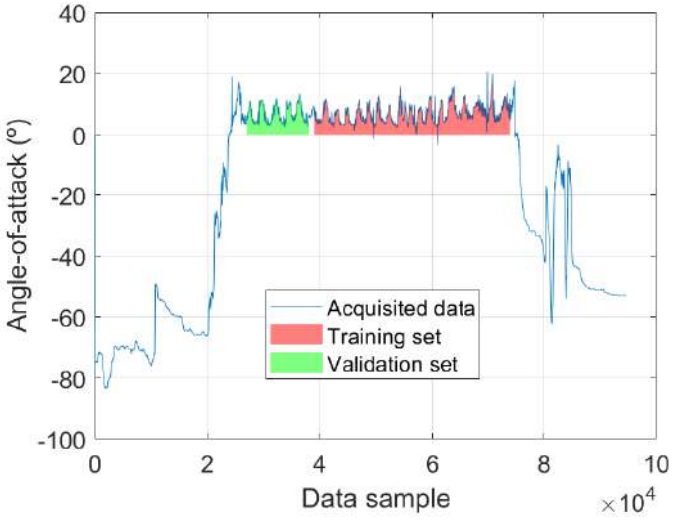

Figure 3.8: Training set and validation set visualization. Source: Author.

This chapter presented how the GFF aerodynamic data were acquired followed by the procedures to improve the quality of those signals extracted from Pixhawk SD card. The following chapter will present the results of the aerodynamic model predicted by the Neuro-Fuzzy technique.

The Tab. 3.1 presents the correlation among all input variables for the longitudinal and the lateral-directional axes.

Table 3.1: Correlation between longitudinal and lateral-directional input variables

Longitudinal training data					
	δ_E	δ_C	α	$\dot{\alpha}$	q
δ_E	1.000	-0.923	-0.612	-0.424	-0.699
δ_C		1.000	0.644	0.436	0.867
α			1.000	0.000	0.587
$\dot{\alpha}$				1.000	0.458
q					1.000
Longitudinal validation data					
	δ_E	δ_C	α	$\dot{\alpha}$	q
δ_E	1.000	-0.996	-0.871	-0.345	-0.878
δ_C		1.000	0.856	0.347	0.869
α			1.000	0.000	0.647
$\dot{\alpha}$				1.000	0.453
q					1

Lateral-directional training data					
	α	β	$\dot{\beta}$	δ_A	p
α	1.000	0.092	0.046	0.098	0.010
β		1.000	0.312	0.247	0.047
$\dot{\beta}$			1.000	0.370	0.219
δ_A				1.000	0.844
p					1.000
Lateral-directional validation data					
	α	β	$\dot{\beta}$	δ_A	p
α	1.000	0.190	0.022	0.183	0.110
β		1.000	0.348	0.300	-0.126
$\dot{\beta}$			1.000	0.221	-0.032
δ_A				1.000	0.815
p					1.000

The correlations between the input variables and output variables for the longitudinal axes are presented in the Tab. 3.2.

Longitudinal training set					
	α	$\dot{\alpha}$	δ_E	δ_C	q
C_X	0.5634	0.0464	-0.0362	0.1432	0.2444
C_m	-0.1663	0.7625	-0.4079	0.3560	0.2549
C_Z	-0.9838	-0.0836	0.6873	-0.7509	-0.6747
Longitudinal validation set					
	α	$\dot{\alpha}$	δ_E	δ_C	q
C_X	0.8109	0.0639	-0.6363	0.6294	0.4449
C_m	-0.1659	0.7433	-0.2146	0.2217	0.2283
C_Z	-0.9940	-0.0594	0.9081	-0.9046	-0.7182

Table 3.2: Correlation between inputs and output variables for the longitudinal axes.

The selected variables for each degree of freedom depends on that correlation. The three most correlated variables were selected as input variables.

The correlation between input variables and output variables for the lateral-directional axes are presented in the Tab. 3.3.

Lateral-Directional training set						
	α	β	$\dot{\beta}$	δ_A	p	r
C_l	-0.0035	-0.2117	-0.2904	0.2662	0.0012	-0.1151
C_Y	-0.4544	-0.5945	-0.5050	-0.1051	-0.1349	-0.3022
C_n	0.0570	0.2695	0.7014	0.7513	0.4687	-0.0329
Lateral-Directional validation set						
	α	β	$\dot{\beta}$	δ_A	p	r
C_l	-0.0058	-0.2694	-0.7485	-0.0155	-0.0014	0.0066
C_Y	-0.5310	-0.6493	-0.7085	-0.2911	-0.0426	-0.2283
C_n	0.0588	0.2720	0.8101	0.5080	0.1708	-0.1112

Table 3.3: Correlation between inputs and output variables for the lateral-directional axes.

Chapter 4

Case Study

This chapter aims to determine the optimal configuration for the Neuro-Fuzzy model. To achieve this objective, several aspects were evaluated, starting with the performance of three different membership function (MF) shapes. After choosing the MF'S shape, a comparison between three inference methods: Mamdani, Takagi-Sugeno (TS), and Pondered Individual Analysis (PIA) (PEREIRA; JAFELICE; FINZI, 2022) is conducted. Additionally, the quality of the training is assessed by evaluating the number of input and output membership functions, as well as the dependence of the input variables in the output function. Finally, the chapter concludes with a comparison between three optimization methods, taking into account the processing time, accuracy, and robustness of each.

4.1 Comparison between different Membership Function shapes

This section will present a comparison between three shapes of membership functions using PIA as a fuzzy inference method. The MF shapes analyzed were: triangular, trapezoidal, and Gaussian functions. Also, the number of membership functions of each input and output variable is maintained between the analysis and it follows the same MISO system from Section 4.2. This analysis uses experimental data from GFF flight tests made by Rueda (2021).

4.1.1 Triangular Membership Functions

Using only triangular MF to describe fuzzy sets did not change the optimization converging time, but the accuracy was affected, as can be seen in Fig. 4.1. The resultant coefficient of determination (R^2) in this case is 42%.

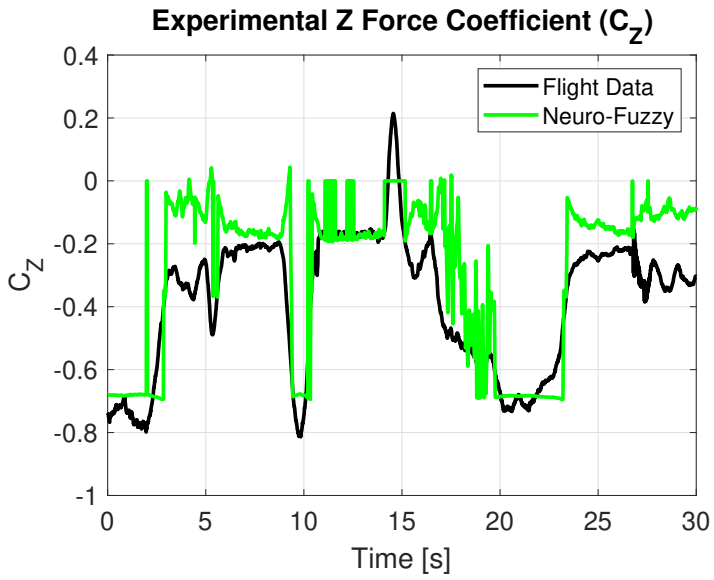

Figure 4.1: Training graph for Z force coefficient using triangular MF in Neuro-Fuzzy with DE. Source: Author.

4.1.2 Trapezoidal Membership Functions

Applying trapezoidal shapes to the input fuzzy sets, the training results are not getting better compared to Fig. 4.1. The ability to fit the experimental flight data is missed using either triangular or trapezoidal MF. The resultant training from the Neuro-Fuzzy with trapezoidal shape MF is illustrated in Fig. 4.2. The coefficient of determination in this case is 39%.

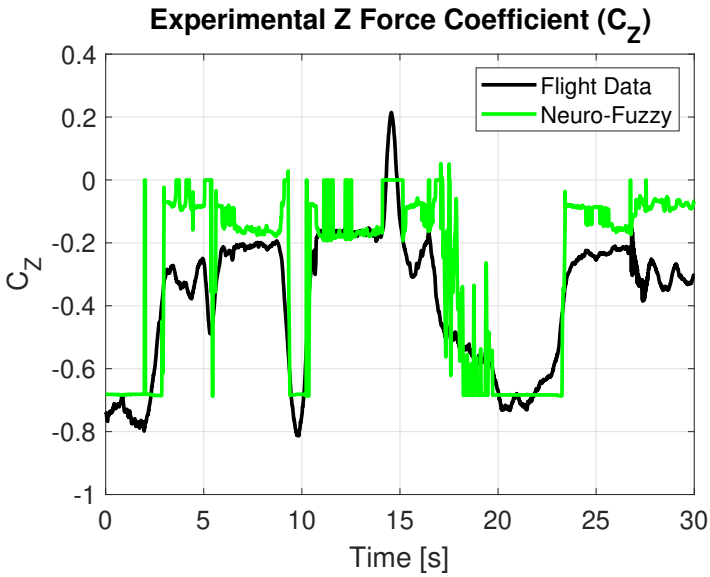

Figure 4.2: Training graph for Z force coefficient using trapezoidal MF in Neuro-Fuzzy with DE. Source: Author.

4.1.3 Gaussian Membership Functions

The last membership function shape analyzed is the Gaussian function. The equation to describe the Gaussian function is described in Eq. 2.8. The coefficient of determination for this shape of membership function is 95%.

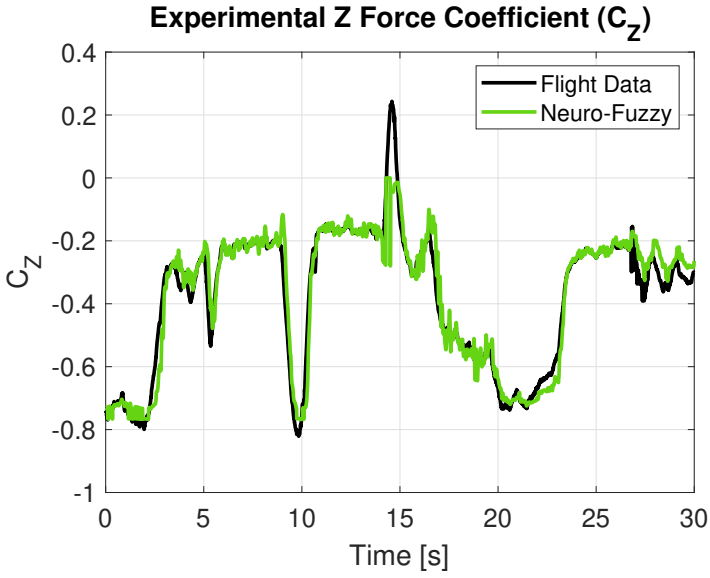

Figure 4.3: Training graph for Z force coefficient using Gaussian MF in Neuro-Fuzzy with DE. Source: Author.

The results emphasize that the best membership function shape for this study is the Gaussian membership functions.

4.2 Comparison between Fuzzy Inference Methods

The comparison between the three fuzzy inference methods is made to study the advantages and the disadvantages, e.g. computational cost and accuracy, which are the most important parameters to be evaluated in each inference method. This evaluation was carried out using experimental data from a Generic Future Fighter (GFF), acquired and supplied by Linköping University.

Each comparison is made using a MISO (Multi Input Single Output) system with emphases on the C_Z because it is the most expressive degree of freedom among all. The Neuro-Fuzzy configuration counts with two input variables, which are the angle of attack (α) and the elevator deflection (δ_e).

The optimization method used for this study is the differential evolution (DE) with 250 generations and with 100 individuals. In terms of evaluation, every fuzzy inference method is trained using the same configuration, which is three membership functions for the input variables and five membership functions or consequent functions (in Takagi-Sugeno's case) for the output.

4.2.1 Neuro-Fuzzy with Mamdani Fuzzy Inference Method

The first evaluation was performed using the Mamdani fuzzy inference method. The time to perform the optimization is extremely high due to the integration of the area. Nevertheless, applying the Mamdani fuzzy inference method to the Neuro-Fuzzy with DE also guaranteed a good curve fitting for the training section. Fig. 4.4a illustrates the training graph using the Mamdani fuzzy inference method.

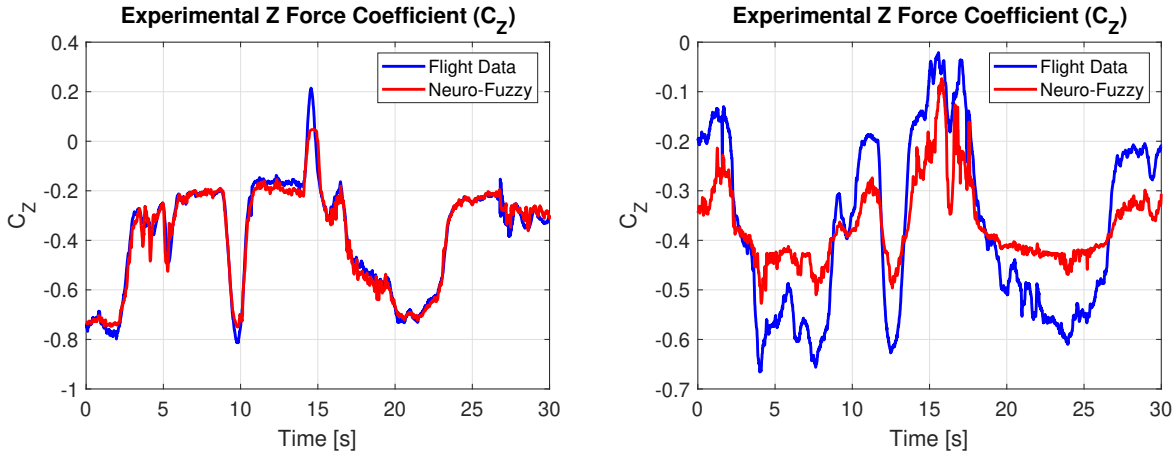

(a) Training (b) Validation

Figure 4.4: Training and validation using the Mamdani fuzzy inference method. Source: Author.

Although, the validation model is taking twenty times more than Takagi-Sugeno or even PIA fuzzy inference method. Furthermore, the validation is not good, as can be seen in Fig. 4.4b.

4.2.2 Neuro-Fuzzy with Takagi-Sugeno Fuzzy Inference Method

This fuzzy inference method allows to reduce the number of fuzzy parameters in the optimization function because the consequent function can be considered as a single variable, which can save some computational effort and time.

The training and validation graph can be observed in Fig. 4.5.

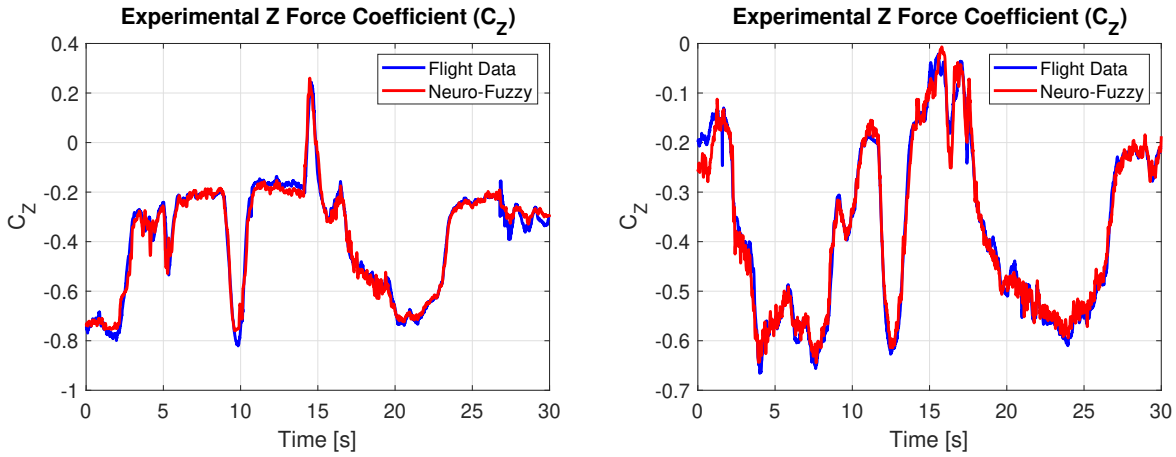

(a) Training (b) Validation

Figure 4.5: Training and validation using the Takagi-Sugeno fuzzy inference method. Source: Author.

4.2.3 Neuro-Fuzzy with PIA Fuzzy Inference Method

Here, the new fuzzy inference method developed by (PEREIRA; JAFELICE; FINZI, 2022) is applied to the Neuro-Fuzzy with Differential Evolution. The curve adjustment for the training can be seen in Fig. 4.6a and the comparison between the three fuzzy inference methods is shown in the Tab. 4.1.

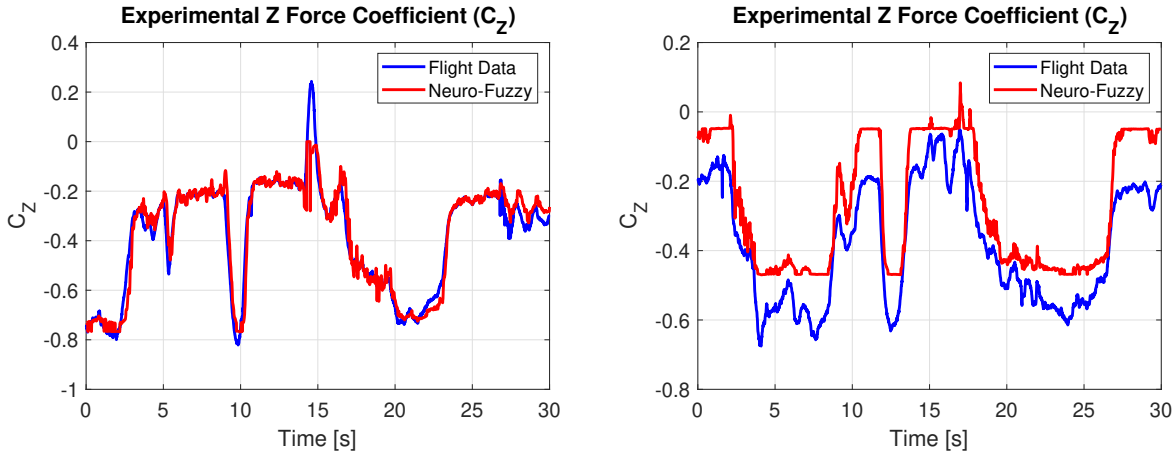

(a) Training (b) Validation

Figure 4.6: Training and validation using the PIA fuzzy inference method. Source: Author.

The validation presented in Fig. 4.6b shows a good curve fitting between the Neuro-Fuzzy and the flight data, however the Takagi-Sugeno is still better in this application.

Table 4.1: Comparison between the three fuzzy inference method.

	Training Time [s]	**Validation Time [s]**	R^2 **[-]**
Mamdani	17.210×10^3	0.558	97%
TS	0.206×10^3	0.026	97%
PIA	3.052×10^3	0.176	95%

4.3 Number of Membership Functions for Inputs

This section investigates the number of membership functions of the input variables that can affect the model in terms of training curve adjustment and evaluates the variation of the coefficient of determination (R^2).

Three different amounts of MF for the input variables of the yawing moment coefficient (C_n) were trained, and Tab 4.2 shows the parameters and results of this analysis.

The time to converge the optimization can carry some uncertainty because another optimization might have been performed at the same time.

Table 4.2: Comparison between the amount of membership functions for the input variables.

	Output Consequent	R^2	**Time [s]**
Two MF	3	0.5691	2058
Three MF	5	0.5701	3252
Four MF	7	0.5673	4418

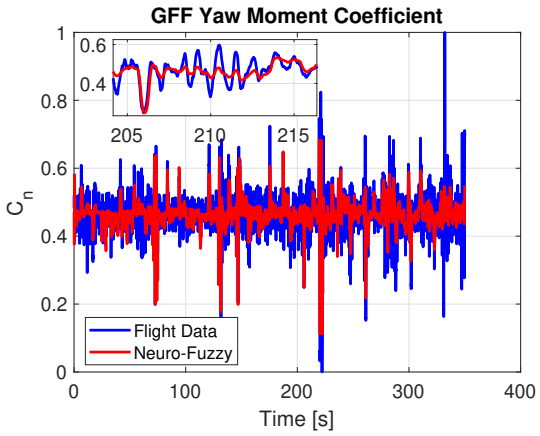

(a) Two membership functions.

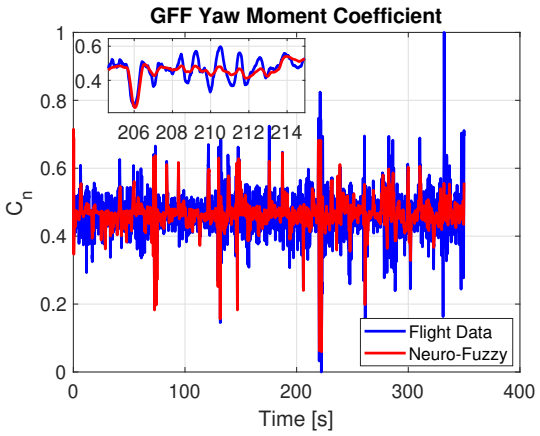

(b) Three membership functions.

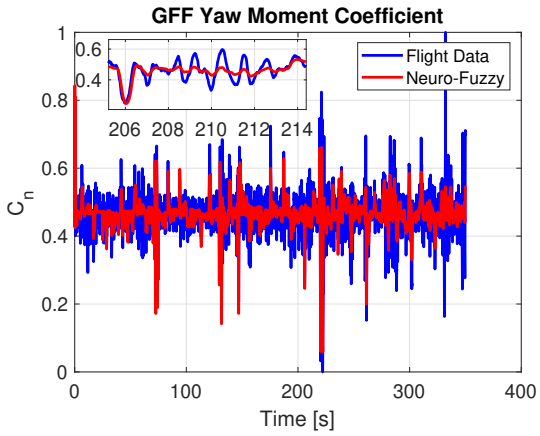

(c) Four membership functions.

Figure 4.7: Training graph for yaw moment coefficient using different numbers of membership functions for the inputs. Source: Author.

Analyzing Figs. 4.7a, 4.7b, and 4.7c and Tab. 4.2 it is possible to observe that the covering percentage from the red curve in the blue curve has not increased, which means that the quality of the training did not changed considerably, it only increased the computational cost, see Tab. 4.2. According to Brandon and Morelli (2016), the number of membership functions of the input variables should vary according to the

correlation between the input and the output variables proportionally.

4.4 Degree of Dependence of the Input Variables in the Output Function

This section presents a comparison between the output functions with dependence on the input variables and the output functions without dependence on input variables, using the Takagi-Sugeno inference method.

The comparison to evaluate the degree of dependence between output functions that have input variable dependencies and output variables that are modeled as a single constant number is performed using the same NF-DE architecture presented in Fig. 5.5. The coefficient of determination from Fig. 4.8a is 23%, while the same coefficient for Fig. 4.8b is 54%.

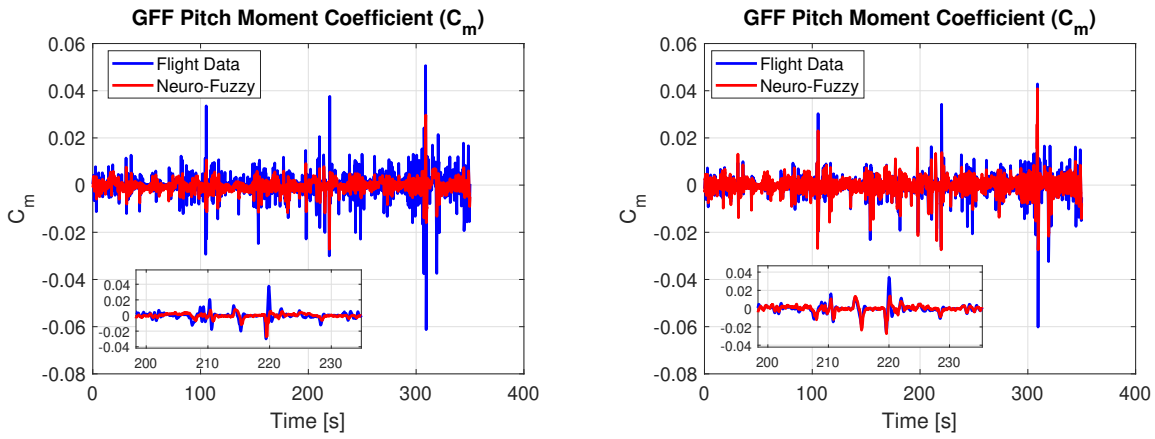

(a) Input Variable Dependent (b) Constant Output Function

Figure 4.8: Comparison between input variable dependence in the output constant function. Source: Author.

The results showed that there are considerable deterioration of the curve fitting when the output function consider the input variable. However, the computational cost could not be evaluated because the optimization stopped after 100 consecutive generations without any improvement in the cost function (coefficient of determination).

4.5 Optimization Methods Evaluation

This section presents three optimization methods, the Differential Evolution, the Genetic Algorithm, and the Complex RF. The comparison explores the total processing time, robustness, and also the accuracy. All the comparisons were made using the Takagi-Sugeno inference method.

The analysis is performed using numerical data from a reduced-scale model of Cessna 182 (SANT'ANA et al., 2019). The data was acquired using a flight simulator known as X-Plane.

4.5.1 Differential Evolution

Using numerical data acquired in X-Plane with a Cessna 182 reduced-scale model designed inside the plane maker environment. The Neuro-Fuzzy with Differential Evolution (NF-DE) optimization time was about 28 seconds for each convergence, and it was performed 30 times in a loop. The results of those amount of optimizations for the Z force coefficient can be observed in Fig. 4.9a.

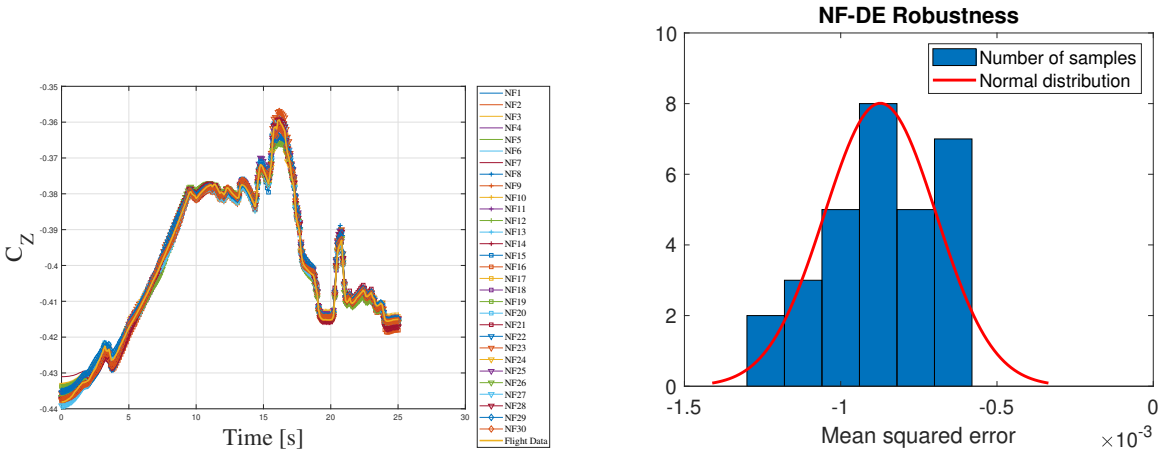

(a) Robustness Analysis (b) Histogram

Figure 4.9: Robustness analysis over thirty optimization using NF-DE. Source: Author.

The robustness of the Neuro-Fuzzy model with Differential Evolution has been analyzed using the Mean Squared Error (MSE). The results of this analysis show that even after thirty optimizations, the result remains around the mean of the solution, presenting a low standard deviation. The figure 4.9b shows the normal distribution using the

Mean Squared Error metric, which illustrates the level of robustness achieved by the model.

4.5.2 Complex RF

With the same numerical data obtained from X-Plane simulations, the Neuro-Fuzzy with Complex RF (NF-CRF) was optimized for each convergence step, taking approximately 171 seconds. The optimization was performed 30 times in a loop, and the results for the Z force coefficient can be seen in Fig. 4.10a.

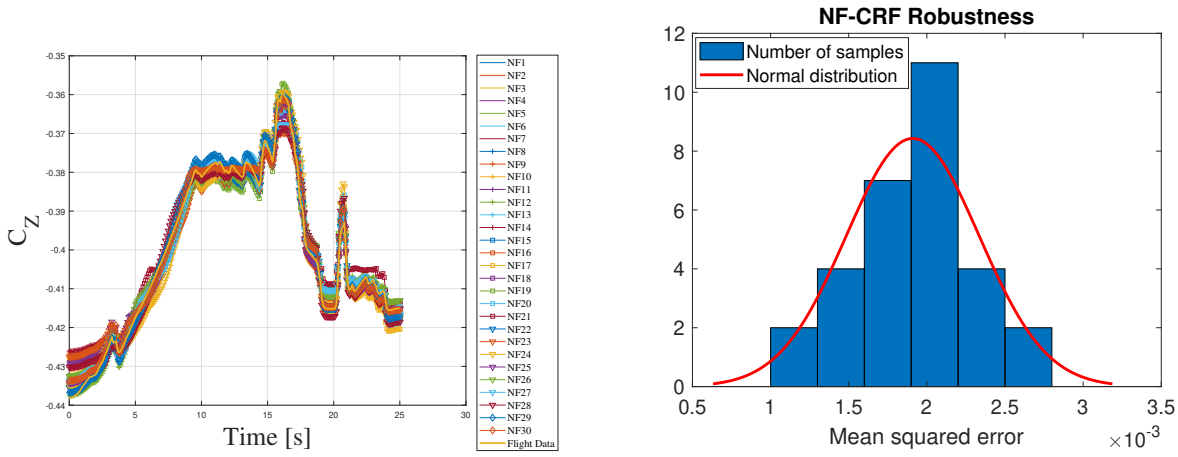

(a) Robustness Analysis (b) Histogram

Figure 4.10: Robustness analysis over thirty optimization of NF-CRF. Source: Author.

The robustness analysis of the Neuro-Fuzzy model with Complex RF was also conducted using the MSE metric. The results of this analysis are presented in Figure 4.10b, which showcases the achieved level of robustness of the model.

4.5.3 Genetic Algorithm

The analysis using the GA optimization method to find the Neuro-Fuzzy parameters showed to be a good alternative. Nonetheless, the accuracy and the computational cost are much worse than the Differential Evolution. The time to obtain forty optimized individuals containing 17 membership function parameters was 3,433 seconds. After each optimization, the best individual was selected manually, and then, the optimization was repeated for 30 times. Fig. 4.11 shows the results of the training over thirty results for the Z force coefficient, and the MSE error distribution.

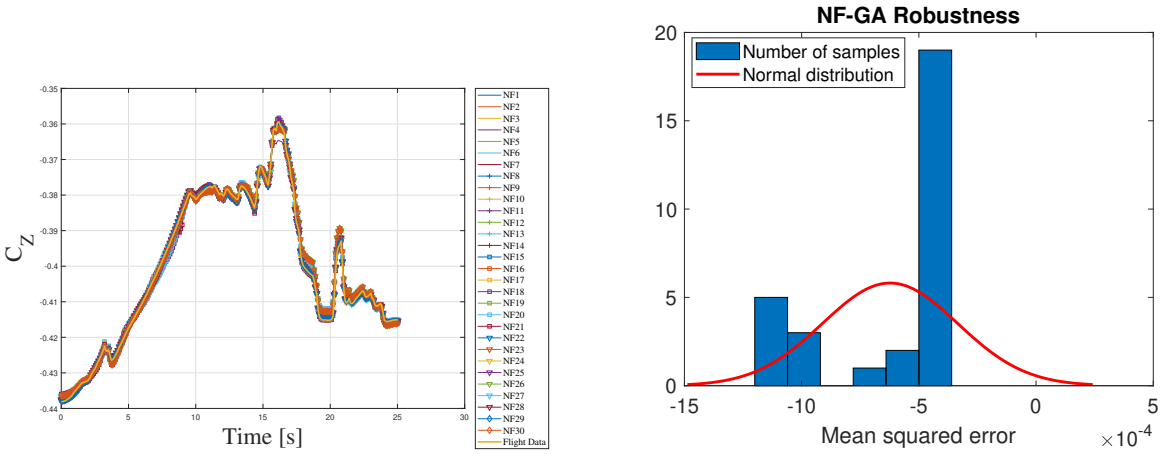

(a) Robustness Analysis (b) Histogram

Figure 4.11: Robustness analysis over thirty optimization using NF-GA. Source: Author.

It is evident from the results that the NF-GA method yields the lowest MSE when compared to all other optimization methods. However, this advantage must be weighed against the longer convergence time required by this method.

This chapter presented several configurations of the Neuro-Fuzzy, and the most efficient NF configuration tested is presented in Table 4.3.

Table 4.3: Optimal Neuro-Fuzzy Configuration

Configuration Parameter	**Value**
Inference Method	Takagi-Sugeno
Membership Function	Gaussian
Number of Input Variables	3
Number of Input Membership Functions	3
Number of Output Functions	7
Output Functions	Constants
Optimization Method	Differential Evolution

The configuration presented above is going to be used to obtain the unsteady aerodynamic model for the GFF.

Chapter 5

Results

This chapter will present the aerodynamic model for the GFF using Neuro-Fuzzy with Differential Evolution (NF-DE). Furthermore, the results are discussed and compared with other methodologies. All the training optimization were made using the Differential Evolution to optimize the parameters from the input and output variables.

Every input variable are normalized in the interval [0,1], to better fit the interval of the membership functions, see Brandon and Morelli (2016). In addition, the input and output variables pass through a low-pass (Lp) or high-pass (Hp) filtering process before entering the neuro-fuzzy optimizer.

5.1 Longitudinal aerodynamic model

5.1.1 Tangential Force (F_X)

The architecture used for the X force coefficient utilizes the input variables α, δ_E and q to construct the aerodynamic model. Figure 5.1 illustrates the Neuro-Fuzzy (NF) architecture that has been developed specifically for modeling the X force coefficient.

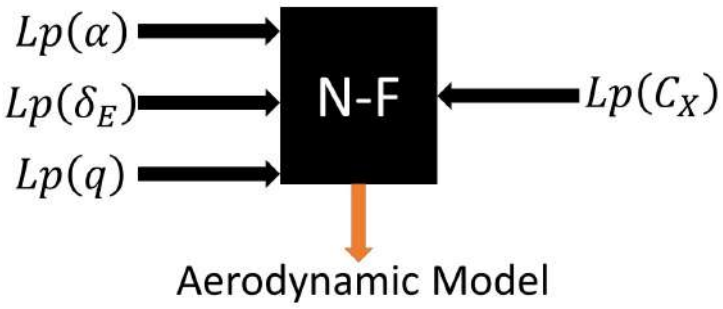

Figure 5.1: Schematic representation of the Neuro-Fuzzy for the force coefficient in X-axis. Source: Author.

For most of the cases, the Neuro-Fuzzy (NF) model is trained using a dataset of 35,000 data points for each variables, if the architecture takes in consider 3 input variables and one output, it gives a total of 140,000 data points. For the X force coefficient, the training takes more than 3 hours (12,105 seconds), and the coefficient of determination (R^2) is 44%. To validate the model, 11,000 data points are used for each input variable, with an accuracy of 46% and a validation time of 0.073 seconds. The training and validation performance of the model for C_X are visualized in Figures 5.2 and 5.3.

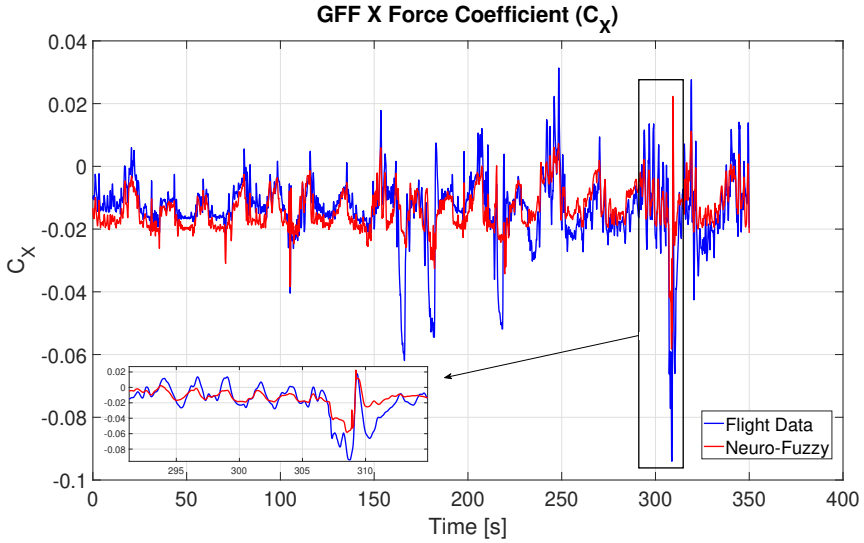

Figure 5.2: Training graph for the tangential moment coefficient. Source: Author.

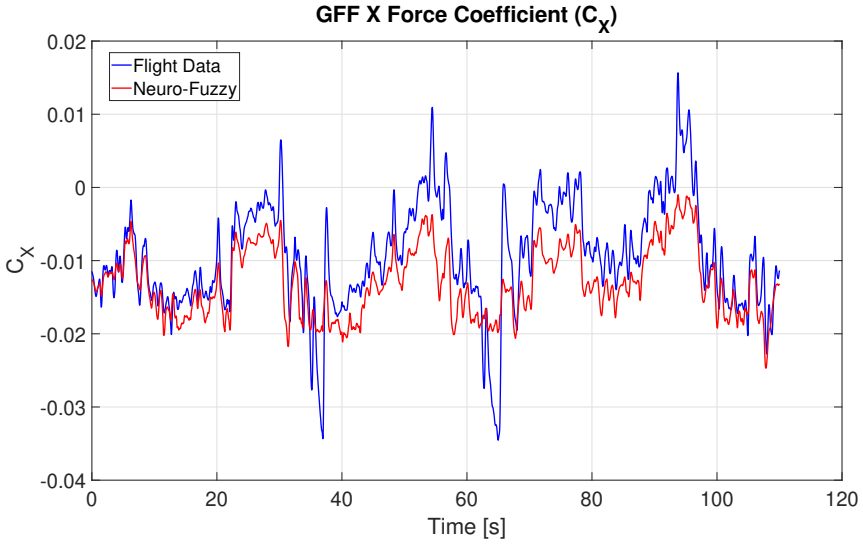

Figure 5.3: Validation graph for the tangential moment coefficient. Source: Author.

Table 5.1 presents the membership function parameters optimized for the input variables of the X force coefficient C_X.

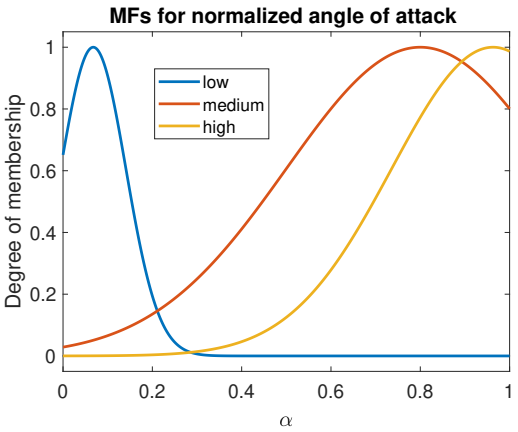

(a) Angle of attack MFs.

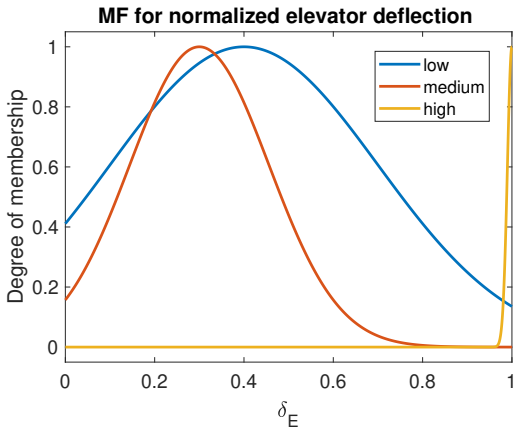

(b) Elevator deflection MFs.

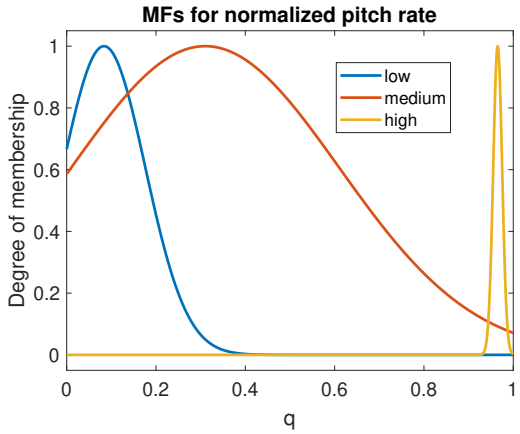

(c) Pitch rate MFs.

Figure 5.4: Membership functions from the three input variables of the X force coefficient. Source: Author.

Table 5.1: Means and standard deviations values of the input membership functions for X force coefficient.

	Mean	**Std**
α	(0.0677 0.8000 0.9629)	(0.0731 0.3000 0.2270)
δ_E	(0.4000 0.3000 1.0000)	(0.3000 0.1559 0.0100)
q	(0.0835 0.3102 0.9651)	(0.0927 0.3000 0.0100)

The seven output functions optimized by the DE are shown in Table 5.2.

Table 5.2: Consequent values for each output variable.

	Consequent function (C)
C_X	-0.0737 -0.0800 -0.0300 -0.0382 -0.0151 0.0300 0.0400

5.1.2 Pitching Moment (M)

In order to model the pitching moment coefficient, the Neuro-Fuzzy (NF) architecture employs the input variables α, $\dot{\alpha}$, and δ_E. The dedicated NF architecture for this purpose is depicted in Fig. 5.5.

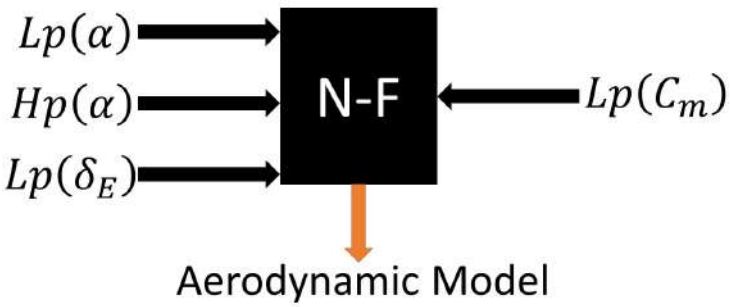

Figure 5.5: Schematic representation of the Neuro-Fuzzy for the moment coefficient around Y-axis. Source: Author.

The training process for this model takes 12,118 seconds, and the coefficient of determination (R^2) is 71%. To validate the model, 11,000 data points are utilized for each input variable, resulting in an accuracy of 43% and a validation time of 0.073 seconds. Figures 5.6 and 5.7 shows the training and validation performance of the model for C_m.

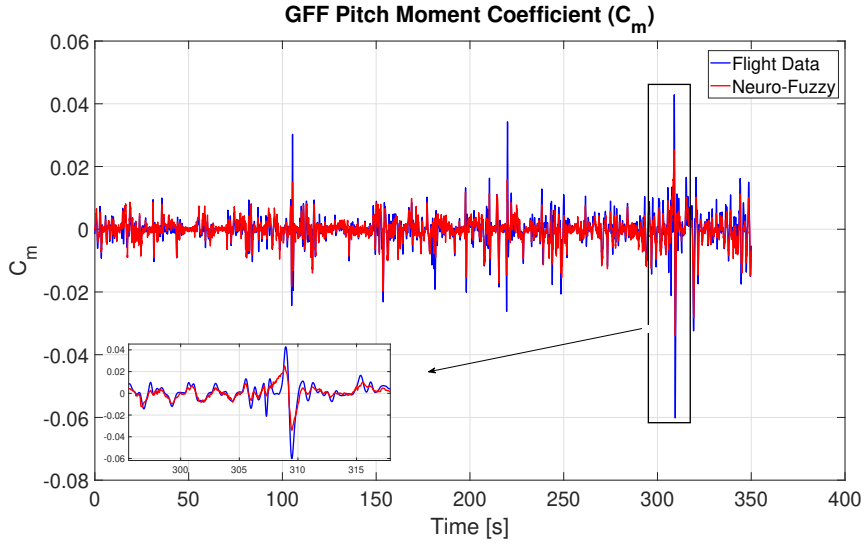

Figure 5.6: Training graph for the pitching moment coefficient. Source: Author.

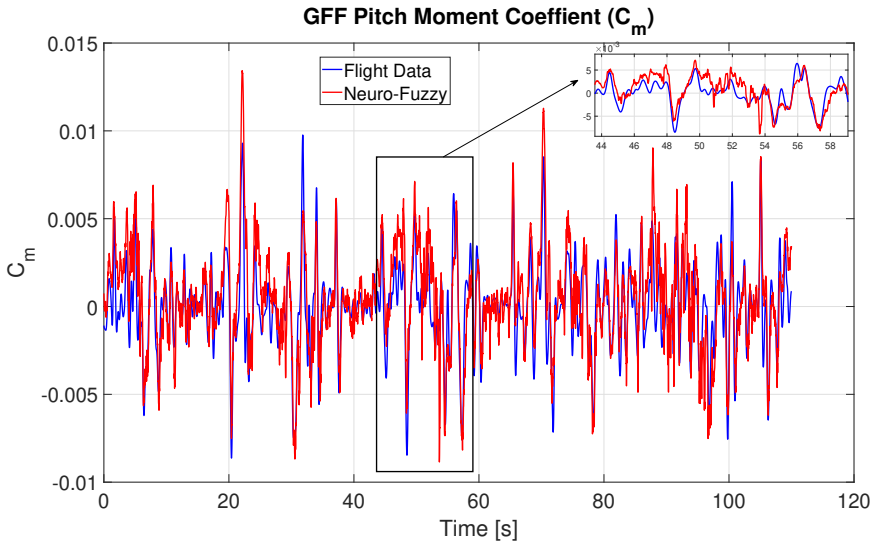

Figure 5.7: Validation graph for the pitching moment coefficient. Source: Author.

The parameters for the membership functions of the input variables can be seen in the Tab. 5.3.

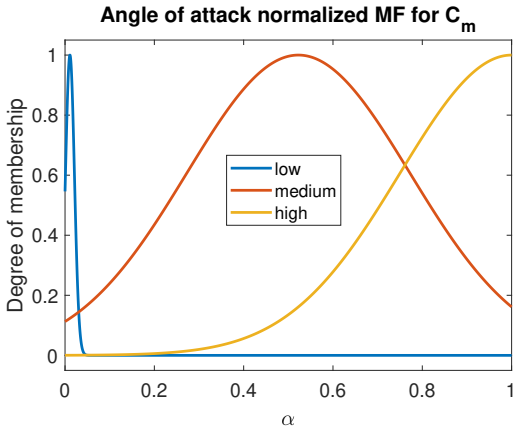

(a) Angle of attack MFs.

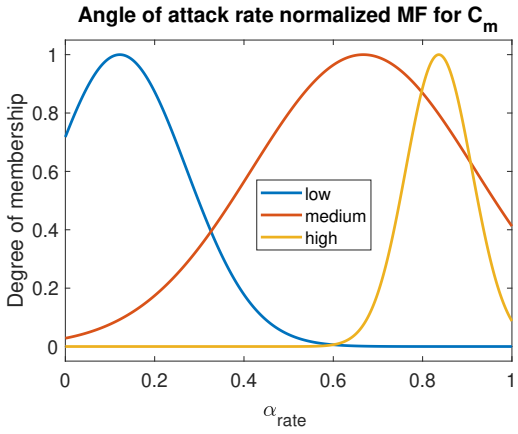

(b) Angle of attack rate MFs.

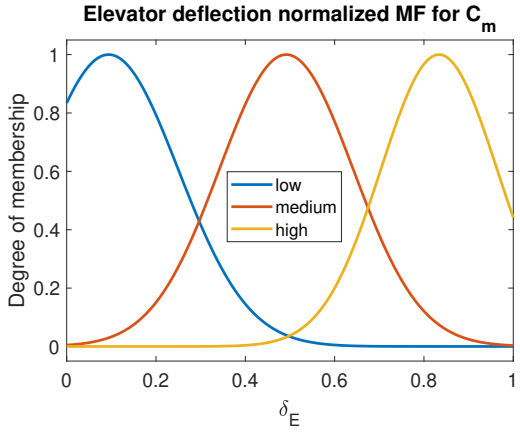

(c) Elevator deflection MFs.

Figure 5.8: Membership functions from the three input variables of the pitch moment coefficient. Source: Author.

Table 5.3: Means and standard deviations values of the input membership functions for pitch moment coefficient.

	Mean	**Std**
$\boldsymbol{\alpha}$	(0.0110 0.5225 1.0000)	(0.0100 0.2500 0.2500)
$\dot{\boldsymbol{\alpha}}$	(0.1219 0.6672 0.8363)	(0.1497 0.2500 0.0741)
$\boldsymbol{\delta_E}$	(0.0939 0.4917 0.8336)	(0.1559 0.1500 0.1302)

The output functions are treated as constants, rendering them independent of the input variables. Table 5.4 provides the optimized values for the seven output functions.

Table 5.4: Consequent values for each output variable.

	Consequent function (C)
$\boldsymbol{C_m}$	-0.0452 -0.0200 0 0.0182 0.0192 0.0310 0.0347

5.1.3 Vertical Force (F_Z)

The Z force coefficient is the most straightforward degree of freedom to model aerodynamically among all aircraft parameters. To build an aerodynamic model using Neuro-Fuzzy, the input variables α, δ_e, and q are utilized. Figure 5.9 depicts the Neuro-Fuzzy architecture designed for modeling the Z force coefficient.

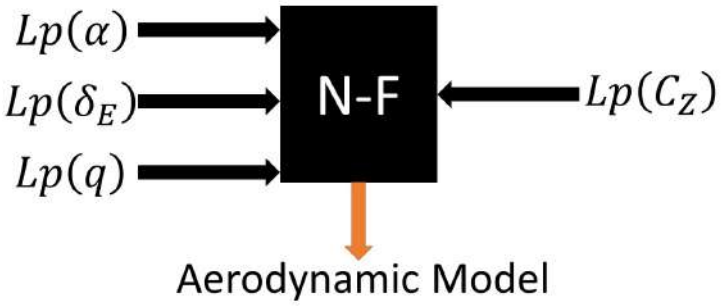

Figure 5.9: Schematic representation of the Neuro-Fuzzy for the force coefficient in Z-axis. Source: Author.

In this case, the Neuro-Fuzzy (NF) model is trained using 35,000 data points for each variable, resulting in a total of 140,000 data points. The training process for the NF-DE takes 10,795 seconds, and the resulting coefficient of determination (R^2) is 96%. For validation, the model is tested using 11,000 data points for each input variable, with a resulting R^2 of 88% and a validation time of 0.090 seconds. Figures 5.10 and 5.11 illustrates the training and validation graph for C_Z.

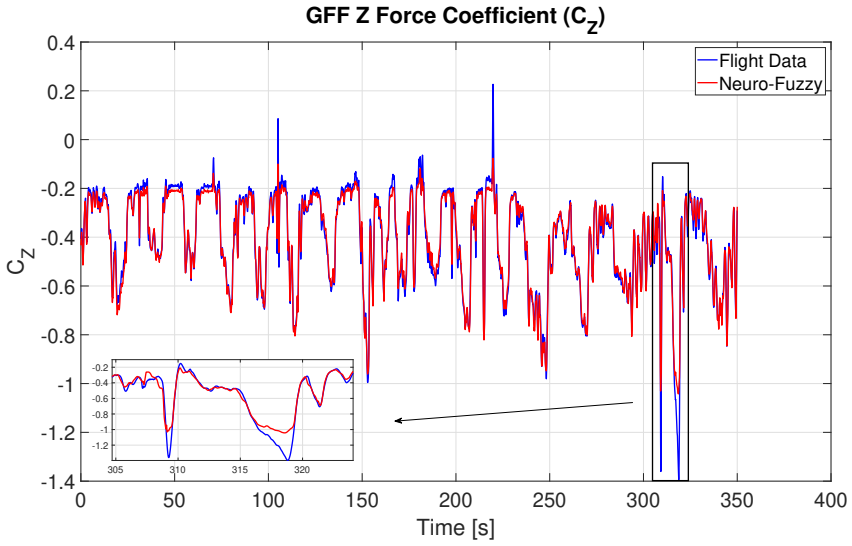

Figure 5.10: Training graph for the vertical force coefficient. Source: Author.

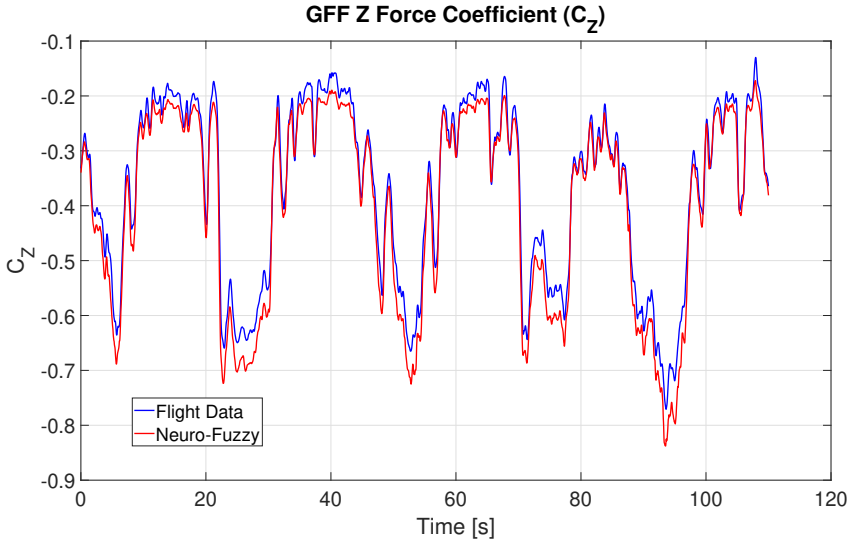

Figure 5.11: Validation graph for the vertical force coefficient. Source: Author.

Table 5.5 presents the membership function parameters used for the input variables of the NF-DE model.

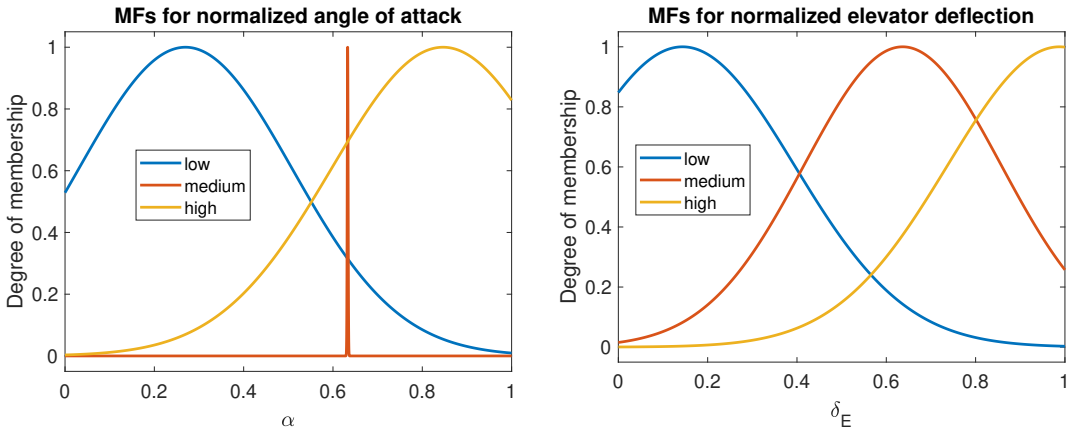

(a) Angle of attack MFs.

(b) Elevator deflection MFs.

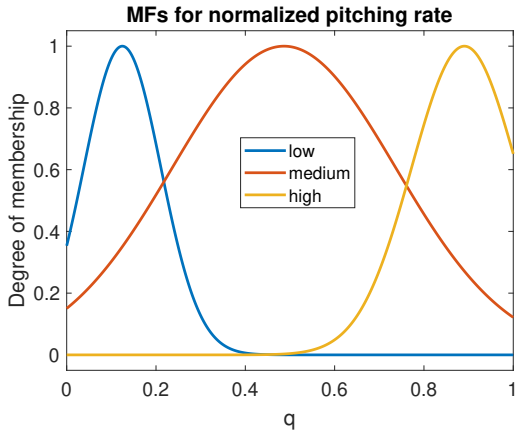

(c) Pitch rate MFs.

Figure 5.12: Membership functions from the three input variables of the Z force coefficient. Source: Author.

Table 5.5: Means and standard deviations values of the input membership functions for Z force coefficient.

	Mean	**Std**
α	(0.2697 0.6329 0.8465)	(0.2389 0.0000 0.2500)
δ_E	(0.1437 0.6366 0.9877)	(0.2500 0.2205 0.2500)
q	(0.1246 0.4866 0.8905)	(0.0864 0.2500 0.1182)

Here the output functions are also treated as constants. Table 5.6 displays the optimized values for the seven output functions.

Table 5.6: Consequent values for each output variable.

	Consequent function (C)
C_Z	-1.2157 -1.0222 -1.1000 -0.9000 -0.2054 0 -0.0343

5.2 Lateral-Directional aerodynamic model

5.2.1 Rolling moment (L)

The roll moment coefficient (C_l) has three input variables, which are β, $\dot{\beta}$, and δ_A. Fig. 5.13 shows the architecture of the Neuro-Fuzzy for the roll moment coefficient.

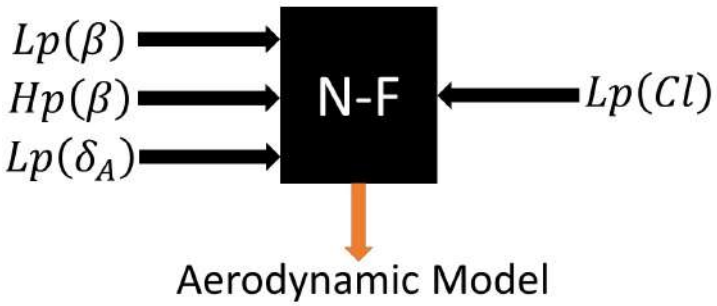

Figure 5.13: Schematic representation of the Neuro-Fuzzy for the moment coefficient around X-axis. Source: Author.

This degree of freedom did not achieved a good curve fitting, see Fig. 5.14. The coefficient of determination is 31% for the training, and the total time to run 804 generations is 13,834 seconds. The validation can be performed in only 0.086 seconds, however the coefficient of determination is bigger than the training's coefficient, with

a value of 41% of accuracy. The Figs. 5.14 and 5.15 shows the curve fitting for the validation set.

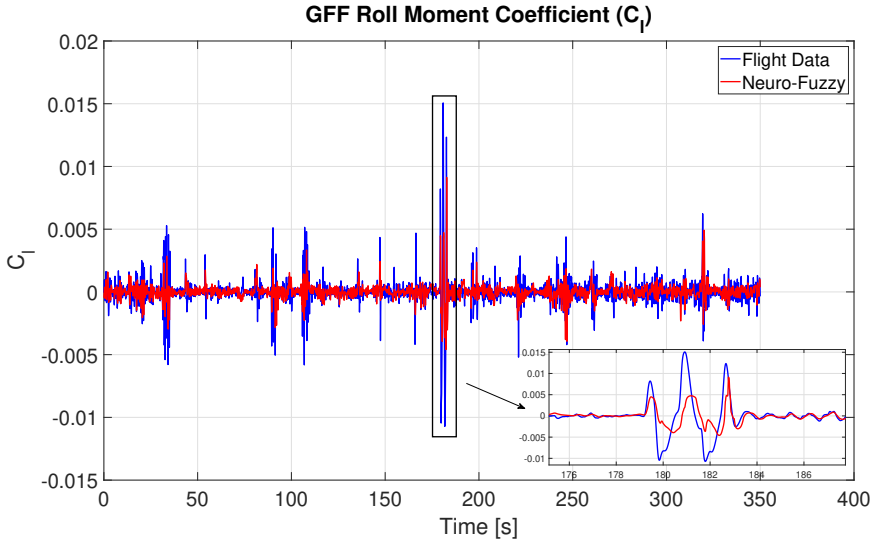

Figure 5.14: Training graph for the rolling moment coefficient. Source: Author.

Upon zooming into specific areas of the training graph, a slight phase discrepancy between flight data and the Neuro-Fuzzy model becomes evident. This phase variation may arise from the application of filters to the variables prior to computing the rolling moment, as demonstrated in Eq. 2.19.

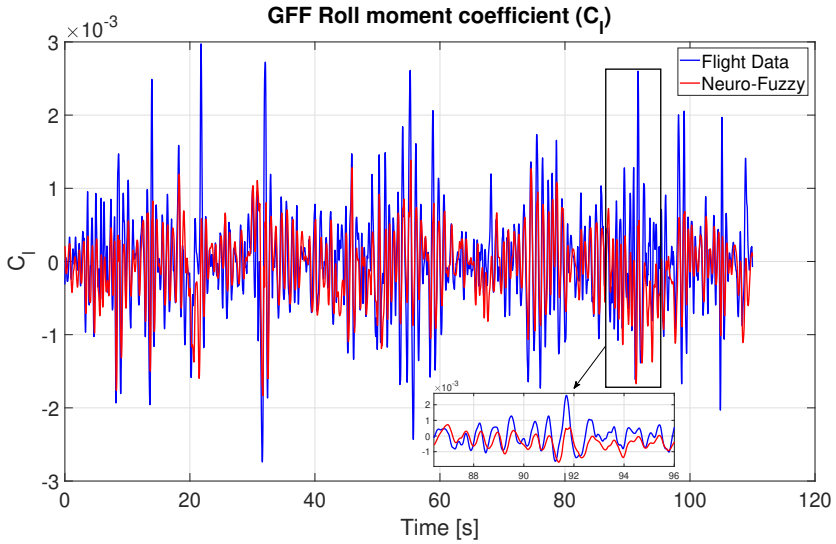

Figure 5.15: Validation graph for the rolling moment coefficient. Source: Author.

The shape of the input membership functions for the roll moment coefficient is illustrated in Fig. 5.16.

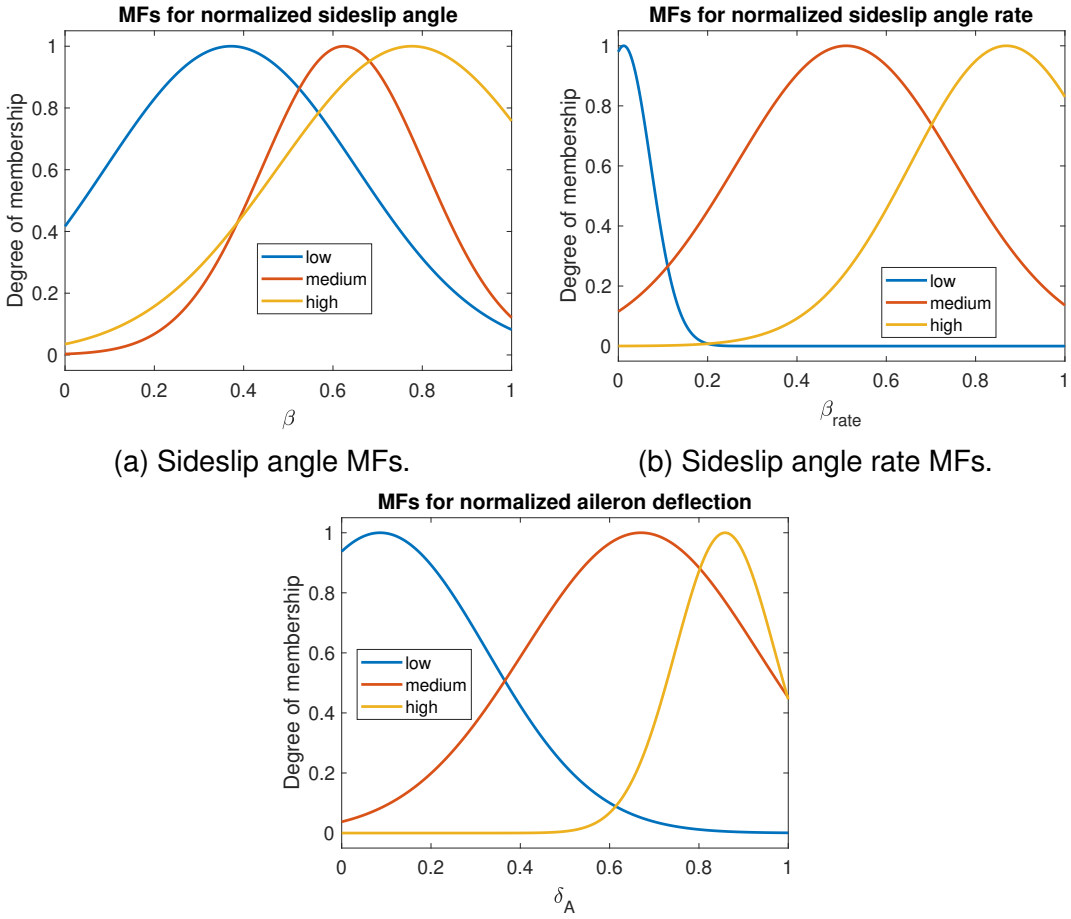

(a) Sideslip angle MFs.

(b) Sideslip angle rate MFs.

(c) Aileron deflection MFs.

Figure 5.16: Membership functions from the three input variables of the rolling moment coefficient. Source: Author.

The optimized Neuro-Fuzzy parameters for the input membership functions are shown in Tab. 5.7.

Table 5.7: Means and standard deviations values of the input membership functions for rolling moment coefficient.

	Mean	**Std**
β	(0.3717 0.6241 0.7766)	(0.2809 0.1829 0.3000)
$\dot{\beta}$	(0.0121 0.5100 0.8690)	(0.0604 0.2453 0.2147)
δ_A	(0.0860 0.6701 0.8584)	(0.2397 0.2615 0.1113)

The seven constant consequents are shown in Tab. 5.8.

Table 5.8: Consequent values for rolling moment coefficient.

	Consequent function (C)
C_l	-0.0104 -0.0063 -0.0008 0.0008 0.0042 0.0119 0.0128

5.2.2 Side Force (F_Y)

The aerodynamic model to predict the force coefficient in Y-axis takes in considering the angle of attack (α), the sideslip angle (β) and it's derivative ($\dot{\beta}$). The NF-DE architecture for the force coefficient in Y-axis is presented in Fig. 5.17.

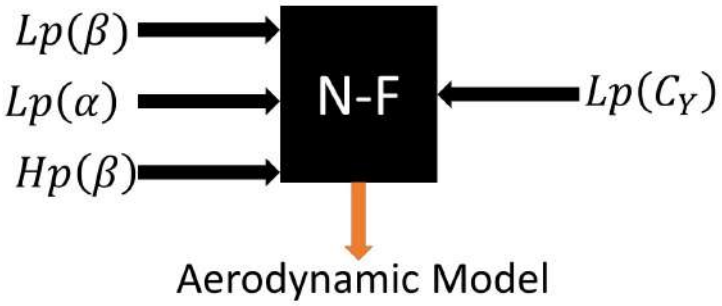

Figure 5.17: Schematic representation of the Neuro-Fuzzy for the force coefficient in Y-axis. Source: Author.

In this case, likewise the previous forces and moments, 140,000 data points has been used to train the model. The training had a total interval of 20,523 seconds to be completed and the coefficient of determination (R^2) was 64%. The validation has an accuracy of 76% (R^2) and 11,000 data points, and the Fig. 5.18 shows the curve fitting for the training, and the Fig. 5.19 shows the validation.

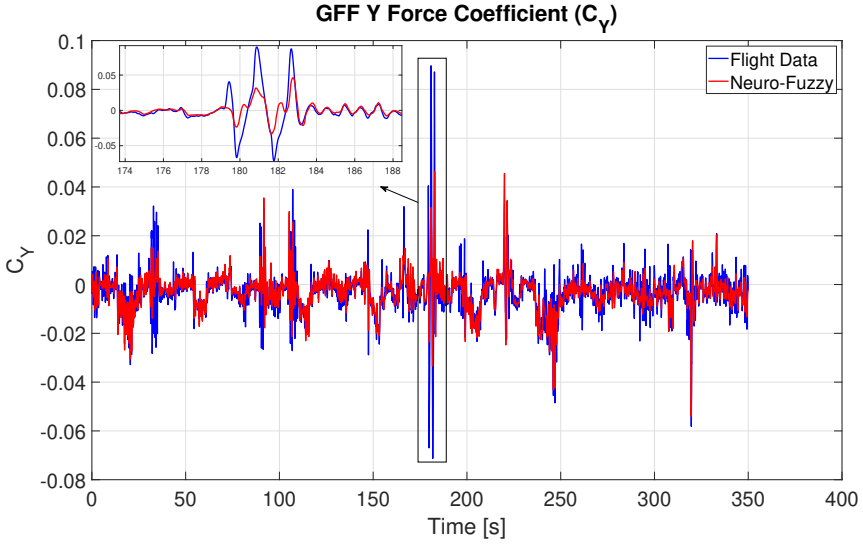

Figure 5.18: Training graph for the side force coefficient. Source: Author.

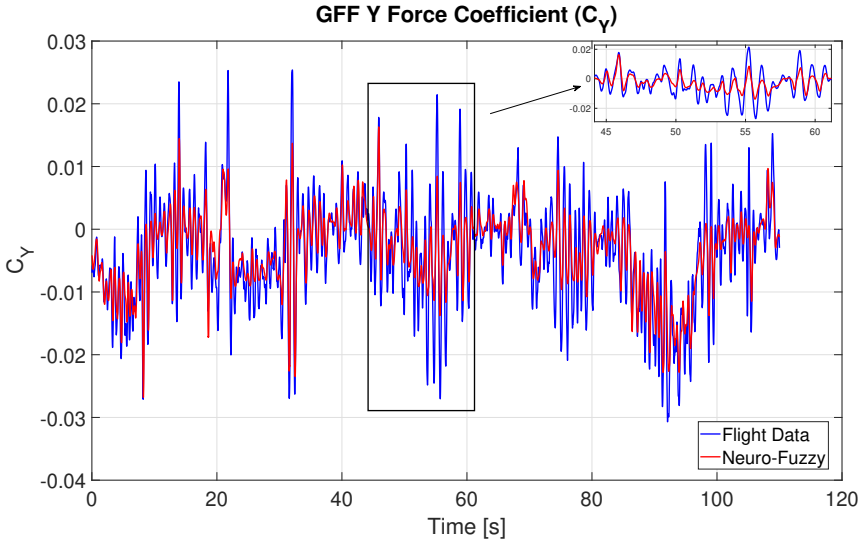

Figure 5.19: Validation graph for the side force coefficient. Source: Author.

The membership functions for the side force coefficient (C_Y) are presented in Fig. 5.20.

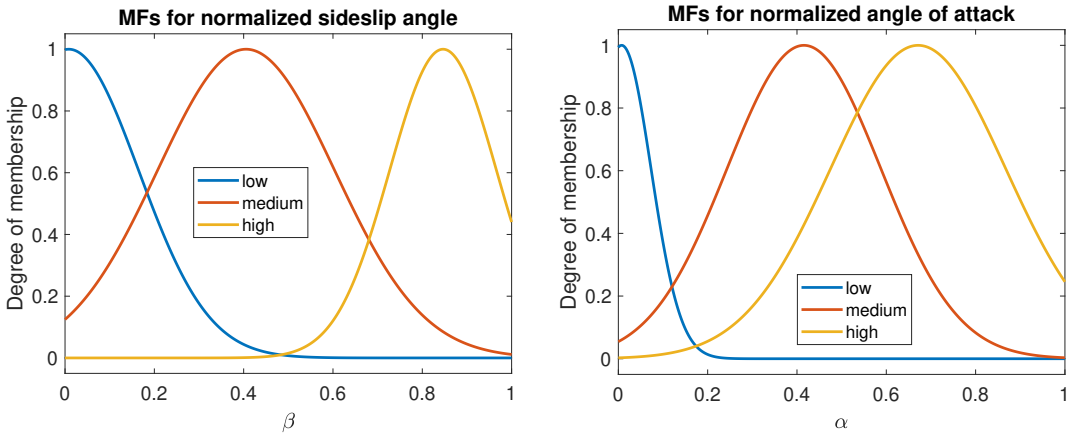

(a) Sideslip angle MFs.

(b) Angle of attack MFs.

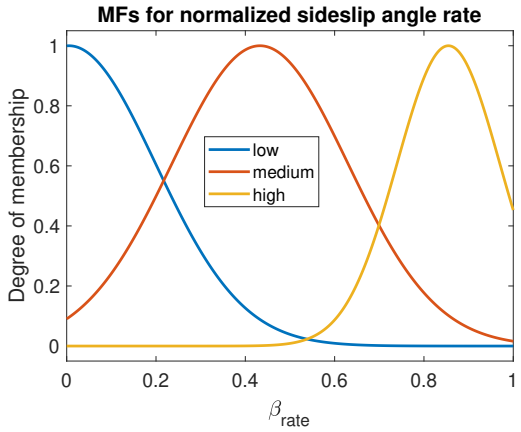

(c) Sideslip angle rate MFs.

Figure 5.20: Membership functions from the three input variables of the roll moment coefficient. Source: Author.

The optimized parameters for the input membership functions is illustrated in Tab. 5.9.

Table 5.9: Means and standard deviations values of the input membership functions for Y-axis force coefficient.

	Mean	**Std**
$\boldsymbol{\beta}$	(0.0084 0.4054 0.8465)	(0.1566 0.1986 0.1198)
$\boldsymbol{\alpha}$	(0.0075 0.4156 0.6713)	(0.0657 0.1723 0.1961)
$\dot{\boldsymbol{\beta}}$	(0.0051 0.4328 0.8548)	(0.1942 0.1974 0.1153)

The output constant functions are shown in Tab. 5.10.

Table 5.10: Consequent values for Y-axis force coefficient.

	Consequent function (C)
$\boldsymbol{C_Y}$	-0.0725 -0.0281 -0.0178 0.0024 0.0217 0.0694 0.0666

5.2.3 Yawing Moment (N)

The architecture of the yawing moment coefficient (C_n) has three input variables, aileron deflection (δ_A), roll rate (p), and sideslip angle rate ($\dot{\beta}$). Fig. 5.21 shows the schematic for the Neuro-Fuzzy architecture for C_n.

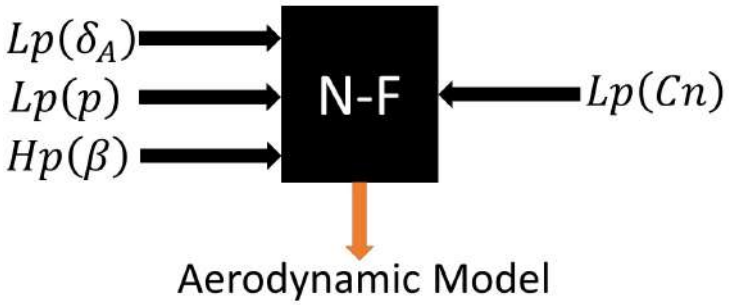

Figure 5.21: Schematic representation of the Neuro-Fuzzy for the moment coefficient around Z-axis. Source: Author.

To train the Neuro-Fuzzy parameters, a total of 140,000 data points were used, with 35,000 for each variable. The curve fitting for the training resulted in a coefficient of determination of 80% and took a total time of 16,902 seconds. Fig. 5.22 shows the curve fitting for the training and Fig. 5.23 shows the curve fitting for the validation. The coefficient of determination (R^2) for the validation set is 74%.

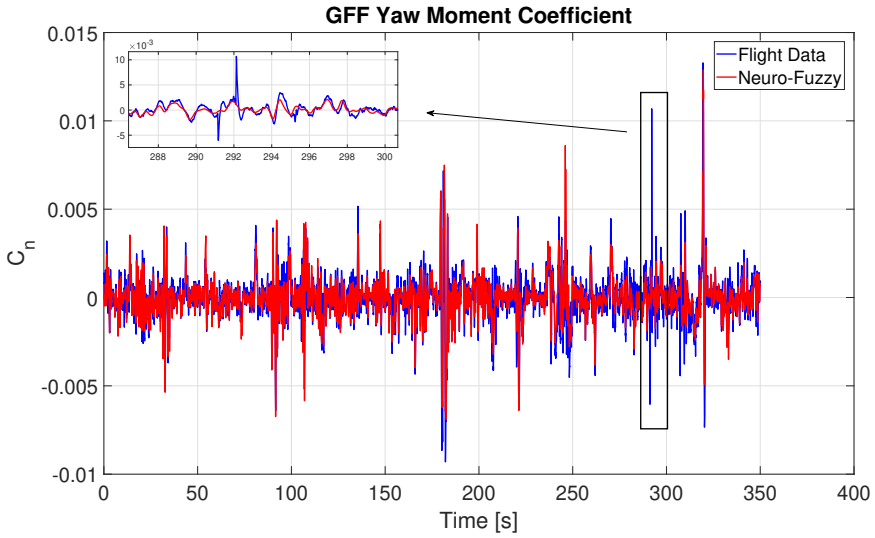

Figure 5.22: Training graph for the yawing moment coefficient. Source: Author.

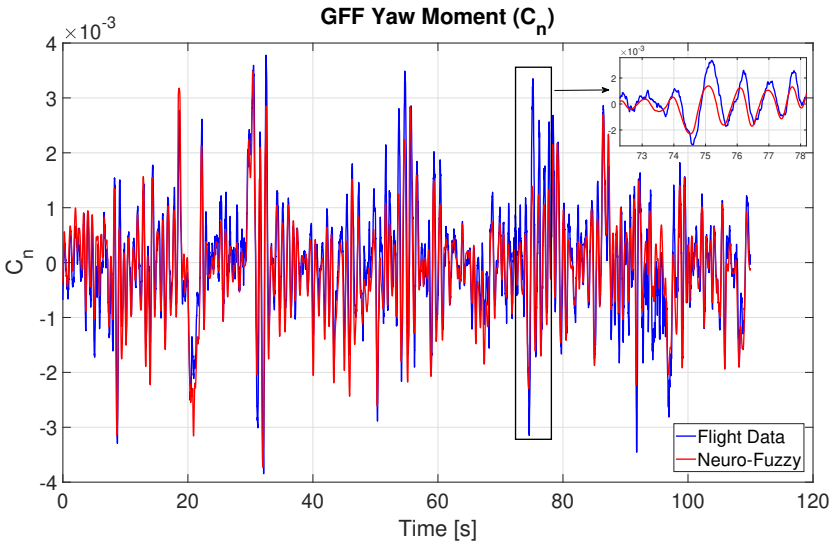

Figure 5.23: Validation graph for the yawing moment coefficient. Source: Author.

The C_n calculation was performed using the Neuro-Fuzzy parameters presented in Tab. 5.11 and Tab. 5.12, with 11,000 data points for each input variable. Remarkably, the computation time for this calculation was only 0.073 seconds.

The membership functions for the input variables of the Neuro-Fuzzy architecture used to train the yaw moment coefficient, is illustrated in Fig. 5.24.

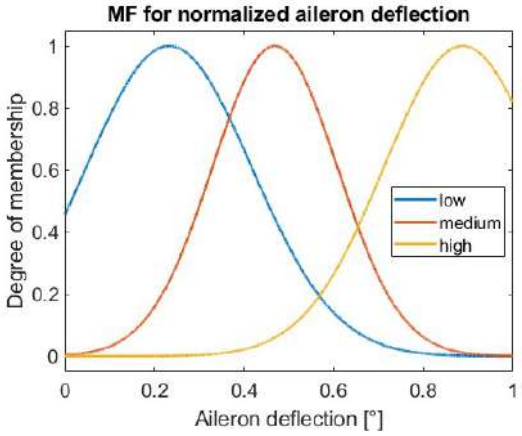

(a) Aileron deflection MFs.

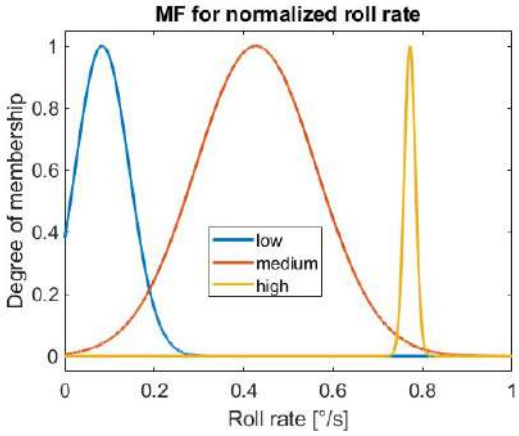

(b) Roll rate MFs.

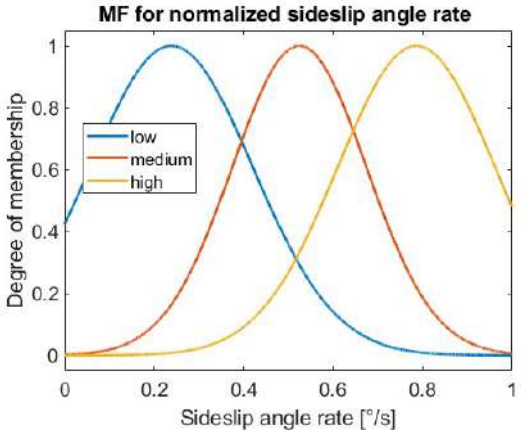

(c) Sideslip angle rate MFs.

Figure 5.24: Membership functions from the three input variables of the yaw moment coefficient. Source: Author.

Table 5.11: Means and standard deviations values of the input membership functions for yaw moment coefficient.

	Mean	**Std**
δ_A	(0.2325 0.4690 0.8880)	(0.1854 0.1401 0.1764)
p	(0.0839 0.4276 0.7718)	(0.0603 0.1355 0.0124)
$\dot{\beta}$	(0.2388 0.5247 0.7865)	(0.1824 0.1504 0.1765)

Table 5.12: Consequent values for Yaw moment.

	Consequent function (C)
C_n	-0.0099 -0.0079 -0.0017 0.0019 0.0061 0.0099 0.0130

This chapter introduced the Neuro-Fuzzy aerodynamic model developed using experimental data collected from the GFF reduced scale aircraft. The model predicts the forces and moments acting in all degrees of freedom using three input variables. This

configuration was chosen due to the absence of any other input variable with a correlation greater than 0.3. Adding more input variables would increase the computational cost and make the rule bases more complex, potentially requiring optimization of the entire rule bases.

Chapter 6

Discussions and Comparisons

This chapter is dedicated to analyse the results obtained in the previous section and comparing them with other methods commonly used in the aerodynamic modeling of the GFF. Its purpose is to provide a comprehensive comparison between the results of the proposed approach and alternative methods employed in this field.

6.1 Stability Derivatives

The stability derivatives of each degree of freedom is going to be presented in this section. The derivatives are calculated as a function of the input variables.

The rule bases for each force or moment coefficient consist of 27 rules. Each degree of freedom is designed with three input variables, each of which has three membership functions, as mentioned in the chapter 4, which are calculated according to Eq. 6.1, where n_{MF} is the number of membership functions for each input variable and i is the number of input variables.

$$N_{rules} = n_{MF}^{i} \tag{6.1}$$

To obtain the stability derivatives, two out of three input variables are declared as 0, which in fuzzy logic means that these variables are always belong to the subset classified as low. When entering the rule bases, the system determines an interval within which the results will fall, and this interval is defined by 3 out of 7 output constant consequents.

To make it a bit more easier to identify the interval of the following stability derivatives, a 3x9 matrix is created with all these rule bases. The Eq. 6.2 below shows this structure.

$$Rules = \begin{bmatrix} C_{111} & C_{211} & C_{311} & C_{121} & C_{221} & C_{321} & C_{131} & C_{231} & C_{331} \\ C_{112} & C_{212} & C_{312} & C_{122} & C_{222} & C_{322} & C_{132} & C_{232} & C_{332} \\ C_{113} & C_{213} & C_{313} & C_{123} & C_{223} & C_{323} & C_{133} & C_{233} & C_{333} \end{bmatrix} \tag{6.2}$$

In the matrix, each coefficient represents a results output function according to the values of the input variables. The index of each coefficient is represented by three numbers, each number corresponding to a specific input variable, respectively the first, second and third input variable of the fuzzy set. The number 1 means that the input variable belongs to the fuzzy set defined as low, the number 2 means that the input belongs to the medium fuzzy set and the number 3 means that the variable belongs to the high fuzzy set. For example a_{123} means that the first input variables is low, the second is medium and the third is high.

Now, the order of the constant consequent functions depends on the proportionality between the input variable and the output variable. A simple example is illustrated in Eq. 6.3, where all the input variables are directly proportional to the output variable. The coefficients of the matrix are defined between 1 and 7, corresponding to the output constant function that each rule represents, according to the values presented in the Chapter 5.

$$Rules = \begin{bmatrix} 1 & 2 & 3 & 2 & 3 & 4 & 3 & 4 & 5 \\ 2 & 3 & 4 & 3 & 4 & 5 & 4 & 5 & 6 \\ 3 & 4 & 5 & 4 & 5 & 6 & 5 & 6 & 7 \end{bmatrix} \tag{6.3}$$

In the example from Eq. 6.3, reducing the influence of the first and second input variables to zero means that only the variation of the third variable will matter. This results in the coefficients C_{111}, C_{112} and C_{113}, which correspond to the 1, 2 and 3 in Eq. 6.3. In other words, these numbers represent the first three consequent functions for this particular FRBS. This specific case represents the yawning moment coefficient (C_n), where each input variable is directly proportional to the output variable.

This was a brief discussion of the possibilities of the interval for each stability deriva-

tive. The following subsections will present each one of them.

6.1.1 Tangential Force

The first Taylor order approximation for the tangential force coefficient of the GFF, based on the input variables used to train the aerodynamic model, can be obtained from Eq. 6.4. The stability derivatives for C_X are also shown in Fig. 6.1.

$$C_X = C_{X_0} + C_{X_\alpha}\alpha + C_{X_{\delta_E}}\delta_E + \frac{\overline{c}}{2V}C_{X_q}q \tag{6.4}$$

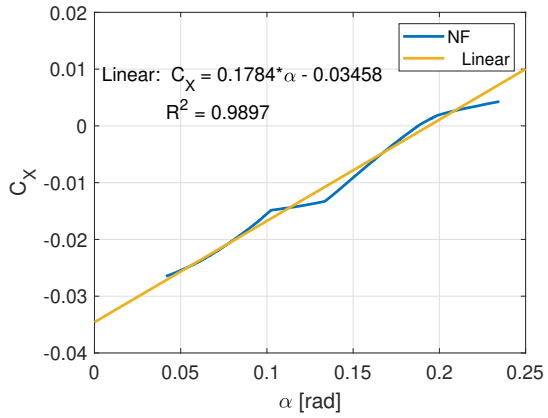

(a) C_X in function of α.

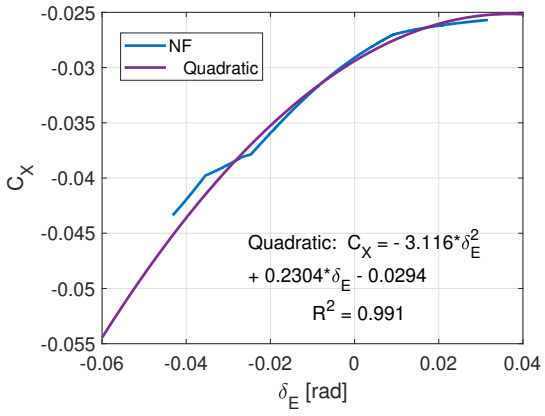

(b) C_X in function of δ_E.

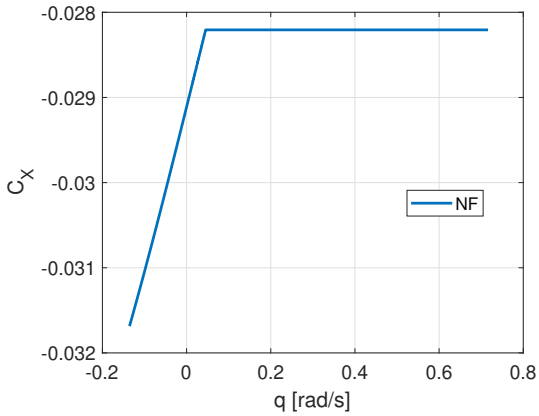

(c) C_X in function of q.

Figure 6.1: Tangential force stability derivatives approximations in radians. Source: Author.

Fig. 6.1a shows that the angle of attack has a linear influence on the tangential force coefficient, while the elevator deflection has a quadratic behavior on the tangential force coefficient, as depicted in Fig. 6.1b. Analyzing the Fig. 6.1c, it becomes clear that C_{X_q}

can be considered as zero. Simplifying the stability derivatives as a linear curve, the first Taylor order equation describing the tangential force coefficient can be seen in Eq. 6.5.

$$C_X = -0.035 + 0.178\alpha + 0.217\delta_E + 0q \tag{6.5}$$

To evaluate how accurate the Eq. 6.5 is with the Neuro-Fuzzy, the Fig. 6.2 is presented. It can be seen that the FTO and the NF have a close behavior on the prediction of the C_X.

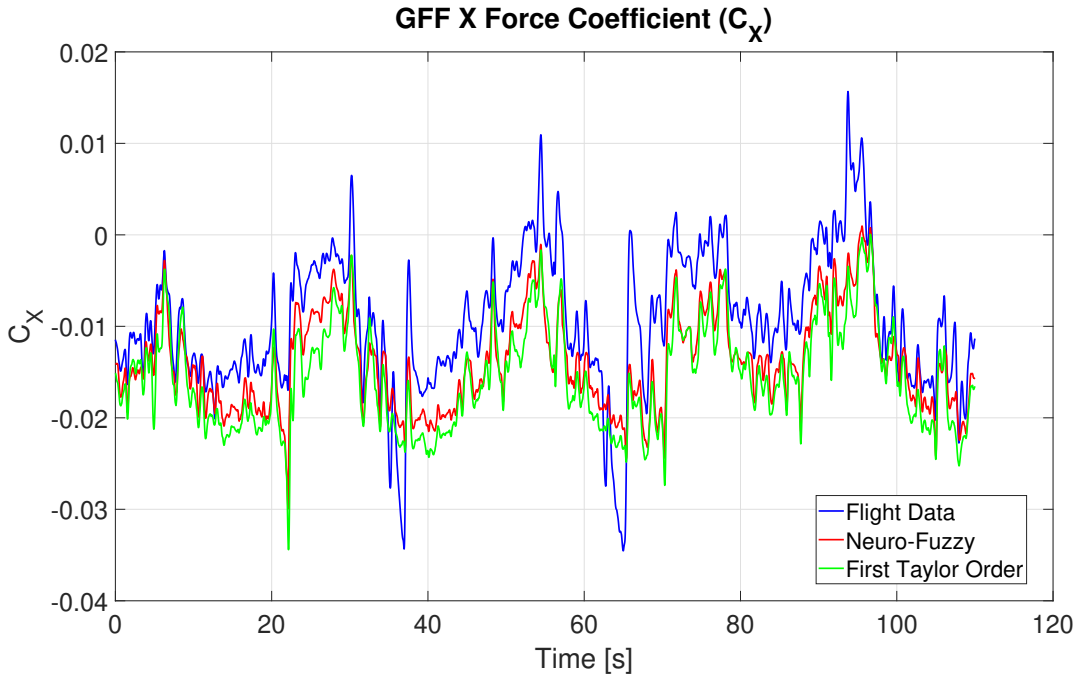

Figure 6.2: Prediction comparison between NF and FTO approximation for the side force coefficient. Source: Author.

6.1.2 Pitching Moment

The pitching moment coefficient can be obtained according to Eq. 6.6, which represents the FTO for the GFF's C_m based on the input variables used to train this moment coefficient. The pitching moment of the GFF is controlled by the canard and the elevator deflection. However, these control surfaces are linked together, and they are indirectly proportional. Therefore, only the elevator deflection is being used. The pitching moment stability derivatives are presented in Fig. 6.3.

$$C_m = C_{m_0} + C_{m_\alpha}\alpha + \frac{\overline{c}}{2V}C_{m_{\dot{\alpha}}}\dot{\alpha} + C_{m_{\delta_E}}\delta_E \tag{6.6}$$

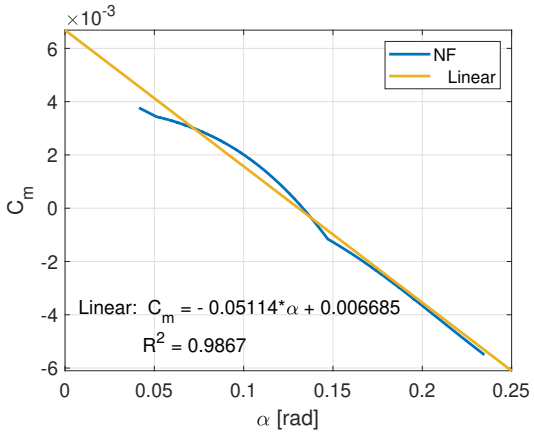

(a) C_m in function of α.

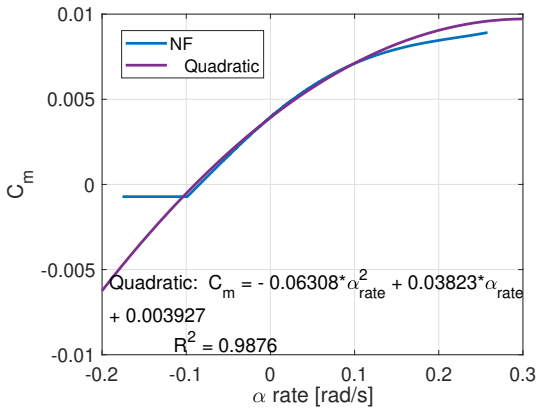

(b) C_m in function of $\dot{\alpha}$.

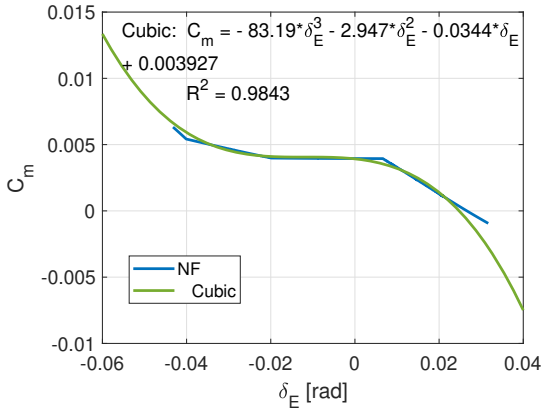

(c) C_m in function of δ_E.

Figure 6.3: Pitching moment stability derivatives approximations in radians. Source: Author.

Fig. 6.3a shows a linear correlation between C_m and α in this particular interval (validation data). However, the correlation between $\dot{\alpha}$ and the pitching moment coefficient is better approximated by a quadratic curve. Furthermore, the elevator deflection has a cubic behavior on C_m. By linear approximations from the curves shown in Fig. 6.3, the first Taylor order approximation that best describes the pitching moment coefficient is presented in Eq. 6.7.

$$C_m = 0.007 - 0.051\alpha + 0.037\dot{\alpha} + -0.066\delta_E \tag{6.7}$$

To evaluate the accuracy of Eq. 6.7 with the NF validation, the Fig. 6.4 is presented.

At some points, the FTO is not good enough to predict the value of C_m.

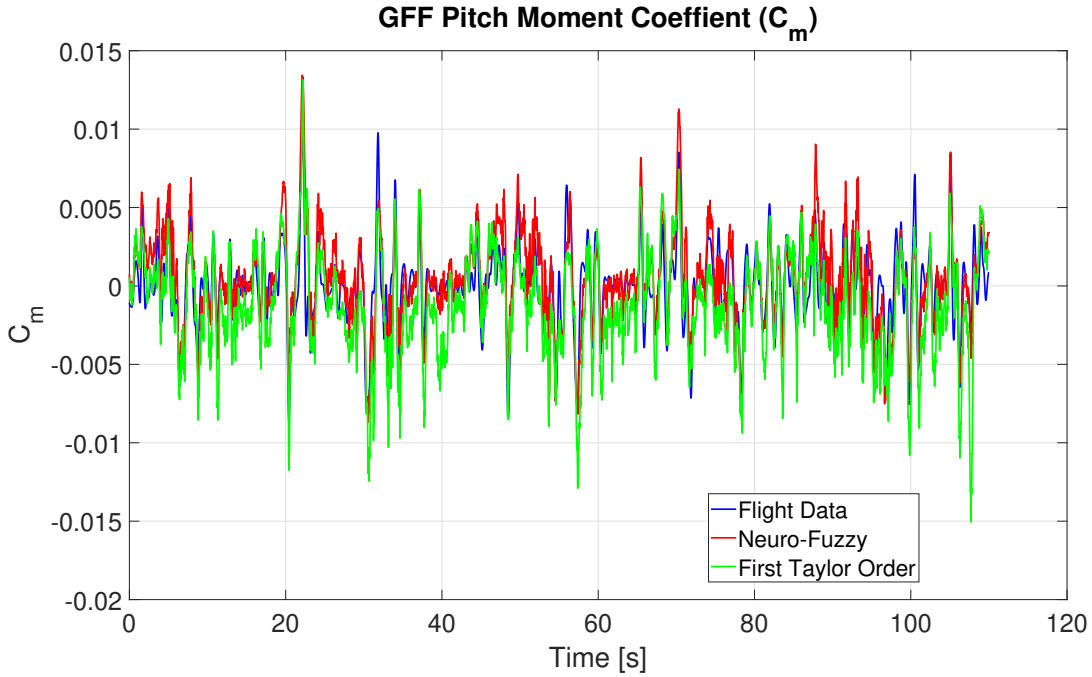

Figure 6.4: Prediction comparison between NF and FTO approximation for the pitching moment coefficient. Source: Author.

6.1.3 Vertical Force

The vertical force coefficient, expressed according to Taylor's theorem, can be represented by Eq. 6.8. To obtain each term of FTO equation, the stability derivatives for C_Z are plotted and approximated by polynomial curves, as shown in Fig. 6.5.

$$C_Z = C_{Z_0} + C_{Z_\alpha}\alpha + C_{Z_{\delta_E}}\delta_E + \frac{\overline{c}}{2V}C_{Z_q}q \tag{6.8}$$

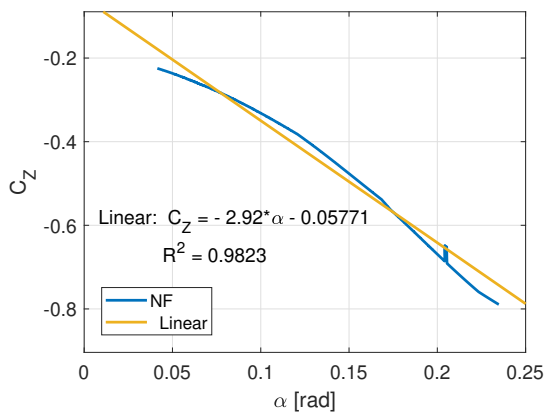

(a) C_Z in function of α.

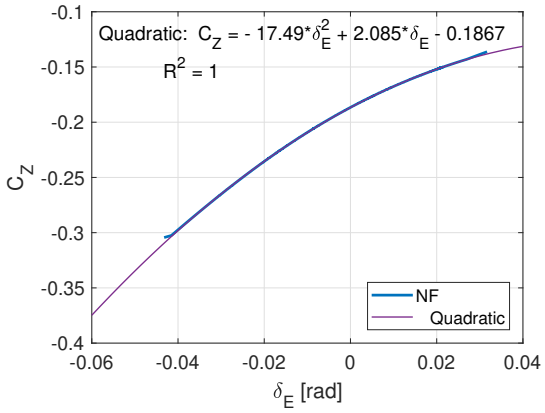

(b) C_Z in function of δ_E.

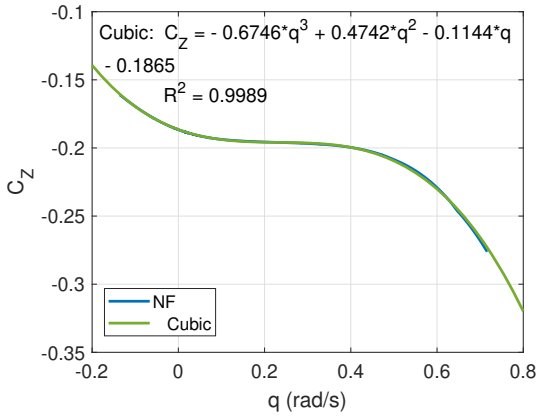

(c) C_Z in function of q.

Figure 6.5: Vertical force stability derivatives approximations in radians. Source: Author.

The most influential variable on the C_Z value is the angle of attack, as shown in Fig. 6.5a. The elevator deflection and the pitching rate also contribute to the vertical force coefficient. Fig. 6.5b shows that positive elevator deflection reduces the value of this coefficient. Furthermore, Fig. 6.5c shows that the pitching rate has a non-linear impact on the C_Z. With these approximations in mind, the first Taylor order expansion that best represents the Z force coefficient is presented in Eq. 6.9.

$$C_Z = -0.058 - 2.920\alpha + 2.185\delta_E - \frac{\overline{c}}{2V}0.046q \tag{6.9}$$

Using the Eq. 6.9, a comparison between the Neuro-Fuzzy, the First Taylor Order approximation and the flight data is presented in Fig. 6.6.

Figure 6.6: Prediction comparison for vertical force coefficient. Source: Author.

6.1.4 Rolling Moment

Based on the input variables used to train the rolling moment coefficient of the GFF, the C_l can be written according to Eq. 6.10.

$$C_l = C_{l_0} + C_{l_\beta}\beta + \frac{b}{2V}C_{l_{\dot{\beta}}}\dot{\beta} + C_{l_{\delta_A}}\delta_A \tag{6.10}$$

The stability derivatives for the rolling moment coefficient are presented in Fig. 6.7.

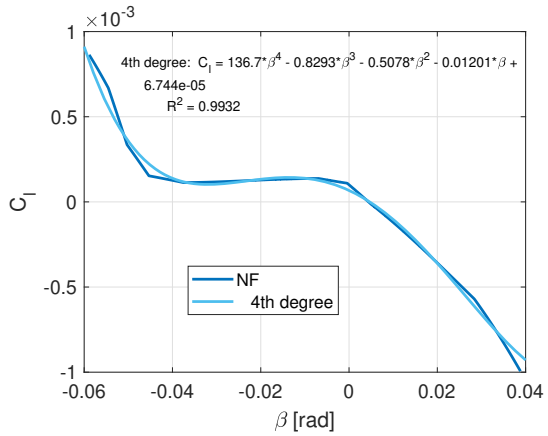

(a) C_l in function of β.

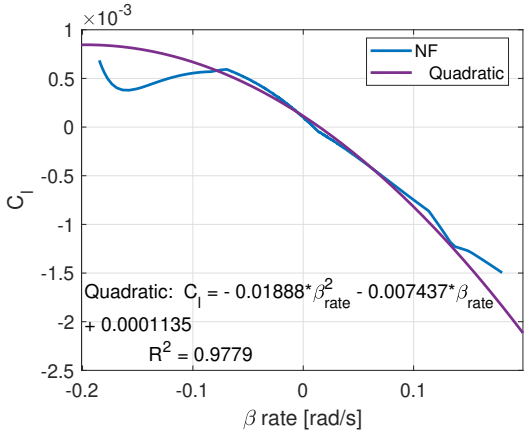

(b) C_l in function of $\dot{\beta}$.

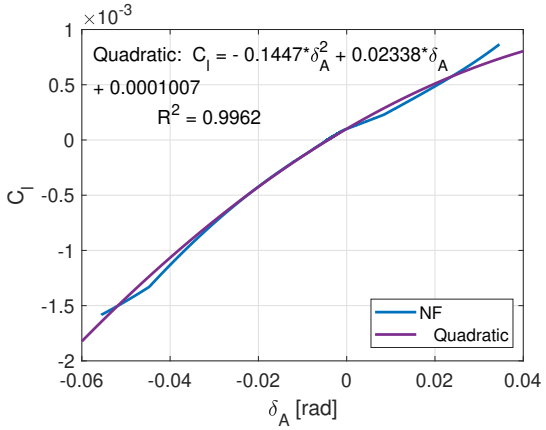

(c) C_l in function of δ_A.

Figure 6.7: Rolling moment coefficient in function of the input variables. Source: Author.

The Fig. 6.7a shows that the sideslip angle affects the C_l in a nonlinear way. The approximated polynomial is a 4th degree polynomial. Additionally, Fig. 6.7b shows the influence of the sideslip angle rate on this coefficient, which gives a quadratic behavior. Finally, Fig. 6.7c characterizes the influence of the aileron deflection on the rolling moment coefficient, making it another influential variable in the rolling moment coefficient. The Eq. 6.11 represents the FTO written with linear curve approximation of the partial derivatives of each nondimensional stability derivative.

$$C_l = 0 - 0.046\beta - \frac{b}{2V}0.007\dot{\beta} + 0.026\delta_A \tag{6.11}$$

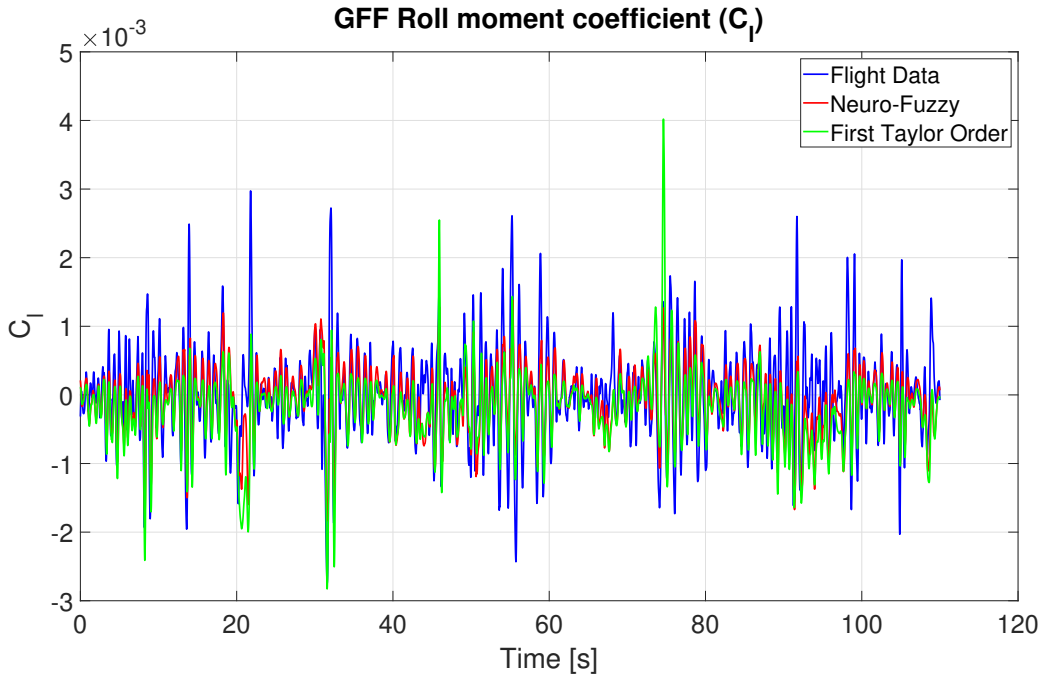

Figure 6.8: Prediction comparison between NF and FTO approximation for the rolling moment coefficient. Source: Author.

6.1.5 Side Force

The first Taylor order series that represent the side force coefficient of the GFF is presented in Eq. 6.12.

$$C_Y = C_{Y_0} + C_{Y_\alpha}\alpha + C_{Y_\beta}\beta + \frac{b}{2V}C_{Y_{\dot{\beta}}}\dot{\beta} \tag{6.12}$$

The stability derivatives for the side force coefficient are presented in Fig. 6.9.

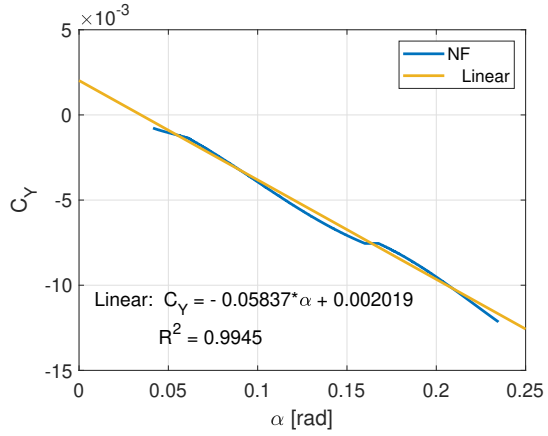

(a) C_Y in function of α.

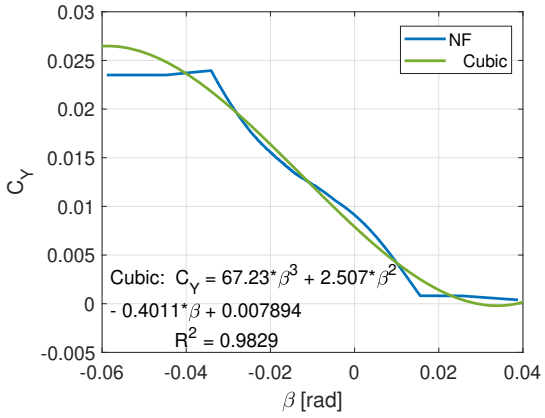

(b) C_Y in function of β.

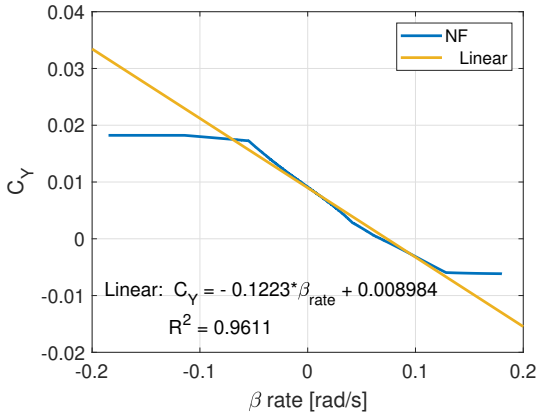

(c) C_Y in function of $\dot{\beta}$.

Figure 6.9: Side force coefficient in function of the input variables. Source: Author.

The sideslip angle has a remarkable influence on the side force coefficient, as it can be seen in Fig. 6.9b and Fig. 6.9c. This fundamental dependence makes β the most important input variable for this force. Furthermore, the angle of attack also has its collaboration, which is also indispensable, as illustrated in Fig. 6.9a.

Substituting the values found in linear approximation in Eq. 6.12, the first Taylor order that better describes the side force coefficient can be rewritten as Eq. 6.13 shows.

$$C_Y = 0 - 0.058\alpha - 0.376\beta - \frac{b}{2V}0.112\dot{\beta} \tag{6.13}$$

Finally, a comparison between the Neuro-Fuzzy prediction and the approximation using the FTO is presented in Fig. 6.10.

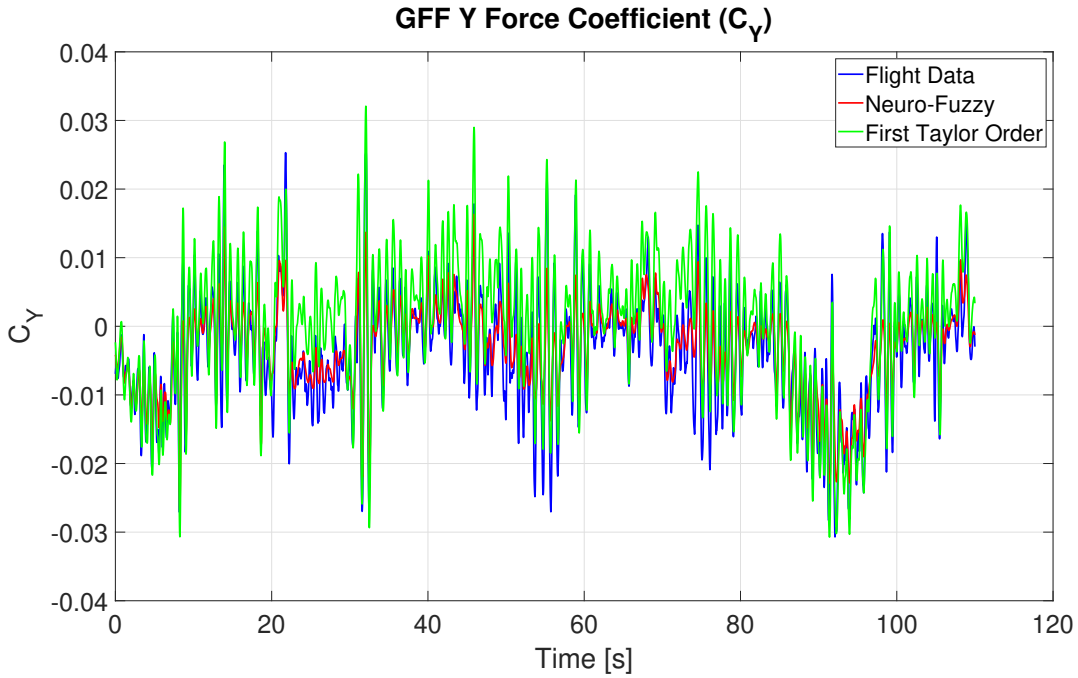

Figure 6.10: Prediction comparison between NF and FTO approximation for side force coefficient. Source: Author.

6.1.6 Yawing moment

The first Taylor order series for the yawing moment coefficient is shown in Eq. 6.14.

$$C_n = C_{n_0} + C_{n_{\delta_A}}\delta_A + \frac{b}{2V}C_{n_p}p + \frac{b}{2V}C_{n_{\dot{\beta}}}\dot{\beta} \tag{6.14}$$

The stability derivatives for the C_n are presented in Fig. 6.11.

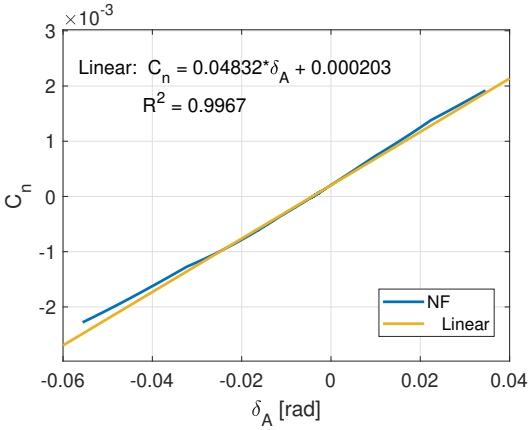

(a) C_n in function of δ_A.

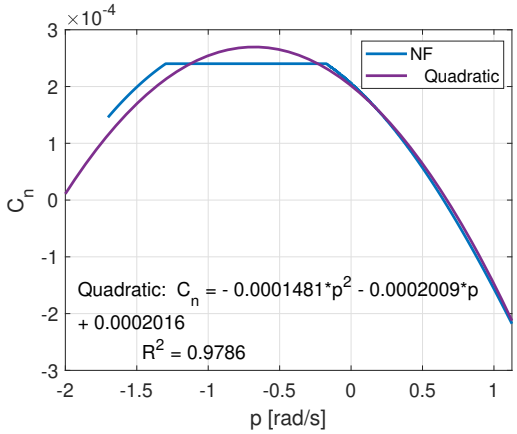

(b) C_n in function of p.

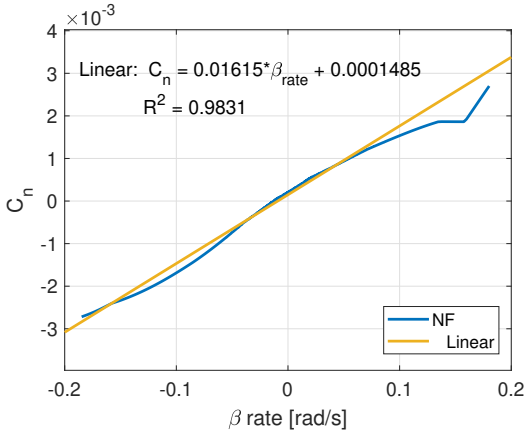

(c) C_n in function of $\dot{\beta}$.

Figure 6.11: Yawing moment coefficient in function of the input variables. Source: Author.

It is noteworthy that the roll rate does not significantly affect the yaw moment coefficient. Fig. 6.11b illustrates this variation. However, the aileron deflection and the sideslip angle rate play a crucial role in influencing this moment coefficient, as depicted in Fig. 6.11a and 6.11c, respectively.

The first Taylor order equation for the yawing moment coefficient can be expressed in Eq. 6.15. In Fig. 6.11b the roll rate does not have a linear coefficient on the interval between $[-1.50; -0.25]$, because it is a constant curve. For values of p above $-0.25 rad/s$, the stability derivative should be approximated to $3.351 \cdot 10^{-4}$.

$$C_n = 0 + 0.030\delta_A + \frac{b}{2V}0p + \frac{b}{2V}0.016\dot{\beta} \tag{6.15}$$

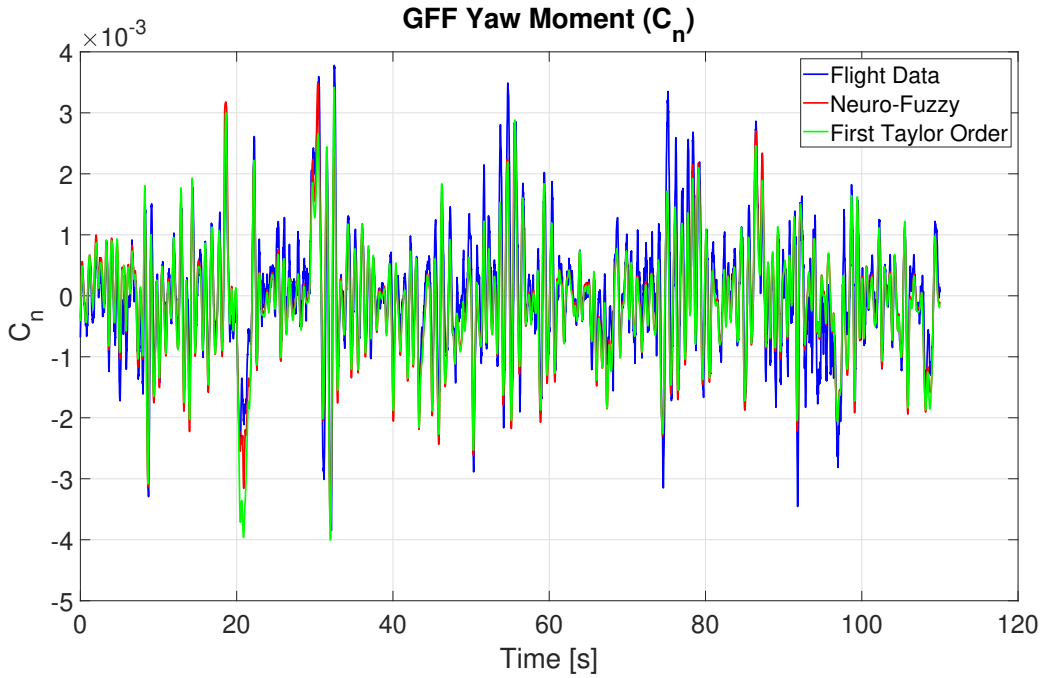

Figure 6.12: Prediction comparison between NF and FTO approximation for yawing moment coefficient. Source: Author.

Analyzing the results presented, it is possible to notice that the derivatives of the attitude angles ($\dot{\alpha}$, $\dot{\beta}$, $\dot{p}$, $\dot{q}$ and $\dot{r}$) have a greater influence on the prediction of the aerodynamic model. This is due to the unsteady aerodynamics and low moments of inertia, which cause the aircraft to oscillate at a high frequency around its center of gravity.

6.2 Comparison with CFD and Wind Tunnel

The results of the Neuro-Fuzzy predicted aerodynamic model are compared with the GFF CFD (Euler and Navier-Stokes) results and with the 1:4 reduced scale GFF wind tunnel (WT) results presented by Larsson et al. (2022). The Figs. 6.13, 6.14 and 6.15 illustrate the difference between the approaches.

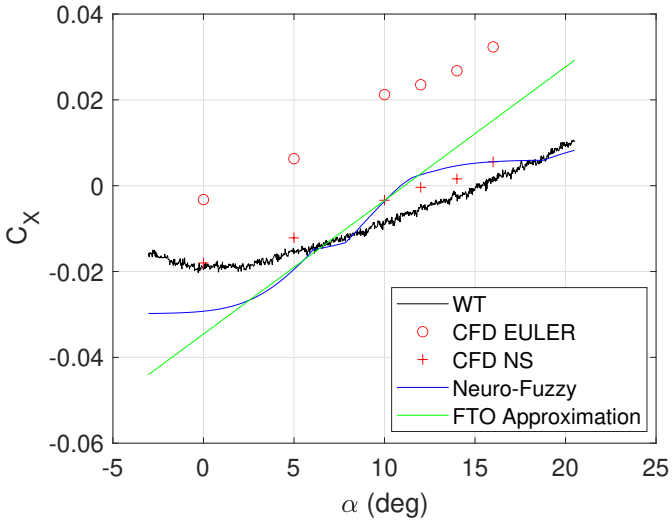

Figure 6.13: Comparison between CFD, Neuro-Fuzzy and Wind Tunnel results for the tangential force F_X. Source: Larsson et al. (2022) and Author.

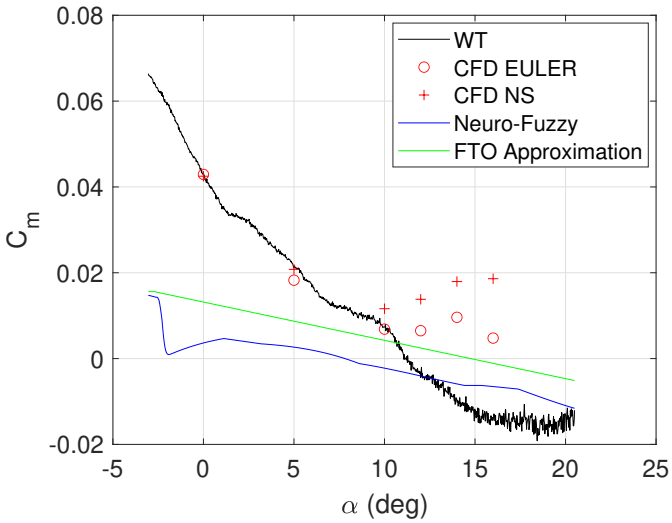

Figure 6.14: Comparison between CFD, Neuro-Fuzzy and Wind Tunnel results for the pitching moment M. Source: Larsson et al. (2022) and Author.

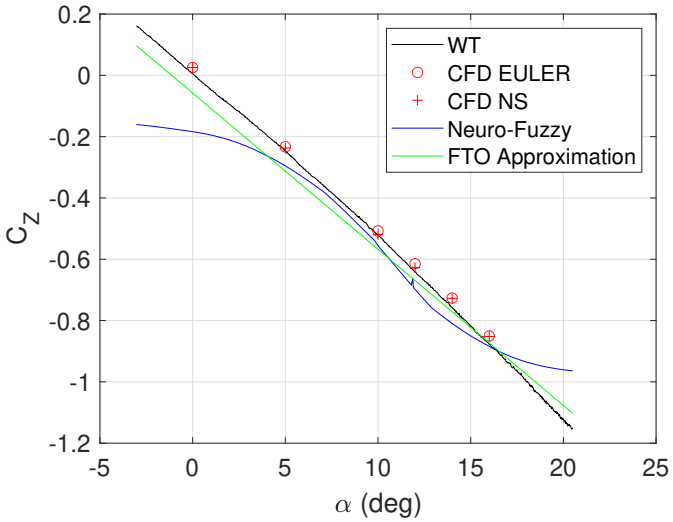

Figure 6.15: Comparison between CFD, Neuro-Fuzzy and Wind Tunnel results for the vertical force F_Z. Source: Larsson et al. (2022) and Author.

The comparison between the Neuro-Fuzzy, CFD and the WT results is close, especially when analyzing the C_X and C_Z. A difference is shown for the pitching moment coefficient. This difference may be due to the condition of the simulations. It is necessary to remember that the conditions are not similar, the flight data were acquired under a perturbed condition, and the simulations in WT and CFD were performed in the steady state. Another factor that could contribute to the difference between the results is the scale factor.

6.3 Model and Simulation

In this section, the author presents an aerodynamic model using Neuro-Fuzzy. This aerodynamic model starts with an initial condition and proceeds to predict the values of the state variables. Figure 6.16 illustrates the Simulink architecture built to simulate the GFF.

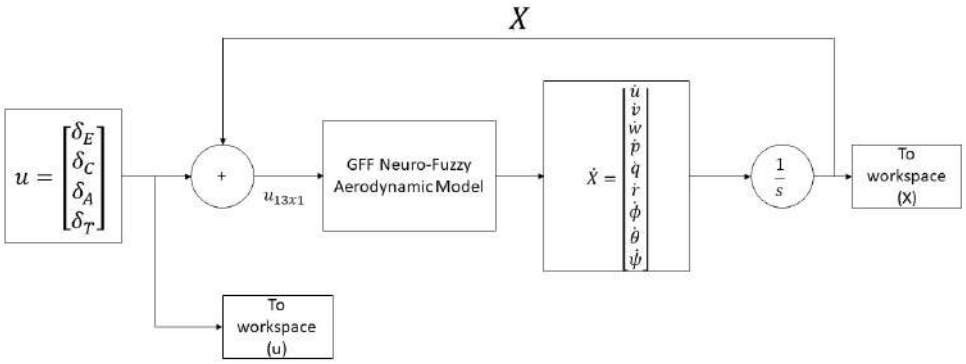

Figure 6.16: Simulink architecture of the GFF model and simulation. Source: Author.

To create the aerodynamic model and simulation, both linear and nonlinear approximations are performed using the stability derivatives presented in the previous section. Only first order polynomial functions are used, with higher order degrees being converted appropriately. The First Taylor Order (FTO) equations are integrated into the GFF Neuro-Fuzzy Aerodynamic Model function, allowing the calculation of each force and moment coefficient. These coefficients are determined using the stability derivatives presented in this chapter, as described in subsection 6.1, with the exception of the rolling moment coefficient, which is estimated based on literature approximations (RUEDA, 2021).

The calculations to obtain the output of the simulation, which is the rate of the stability variables, are better explained in the appendix A.

The input U-matrix consists of the deflection of the GFF control surfaces, as presented in Fig. 6.16. Three conditions are going to be presented: a steady condition, a step input condition and an unsteady state condition. The control surface signals for the unsteady simulation are implemented using the "Signal from Workspace" block available in the Simulink library. It is important to note that in the first two simulations - steady condition and step input condition - the value of the C_{Y_α} was set to zero. This was done as a simplification method to eliminate the influence of the longitudinal mode on the lateral-directional mode. In addition, all lateral-directional static stability derivatives were also set to zero.

The calculation of the state angle rates, such as $\dot{\alpha}$ and $\dot{\beta}$, can be calculated accord-

ing to Fossen (2011). The mathematical expressions are given in Eq. 6.16 and in Eq. 6.17.

$$\dot{\alpha} = \frac{u\dot{w} - w\dot{u}}{u^2 + w^2} \tag{6.16}$$

$$\dot{\beta} = \frac{\dot{v}V - v\dot{V}}{Vcos(\beta)} \tag{6.17}$$

Where $\dot{V}$ can be obtained through Eq. 6.18

$$\dot{V} = \frac{\dot{u}u + \dot{v}v + \dot{w}w}{V} \tag{6.18}$$

6.3.1 Steady Control Inputs

The steady state simulation of the airplane uses a constant value for the U-matrix as input, in order to identify the trim condition of the aircraft. The Figure 6.17 shows the elevator, canard, and aileron deflections as well as the thrust applied during the steady state simulation. The values of this specific trim condition are presented in Eq. 6.19

$$\begin{bmatrix} \delta_E \\ \delta_C \\ \delta_A \\ T \end{bmatrix} = \begin{bmatrix} 0.06 \\ 0 \\ 0 \\ 44 \end{bmatrix} \tag{6.19}$$

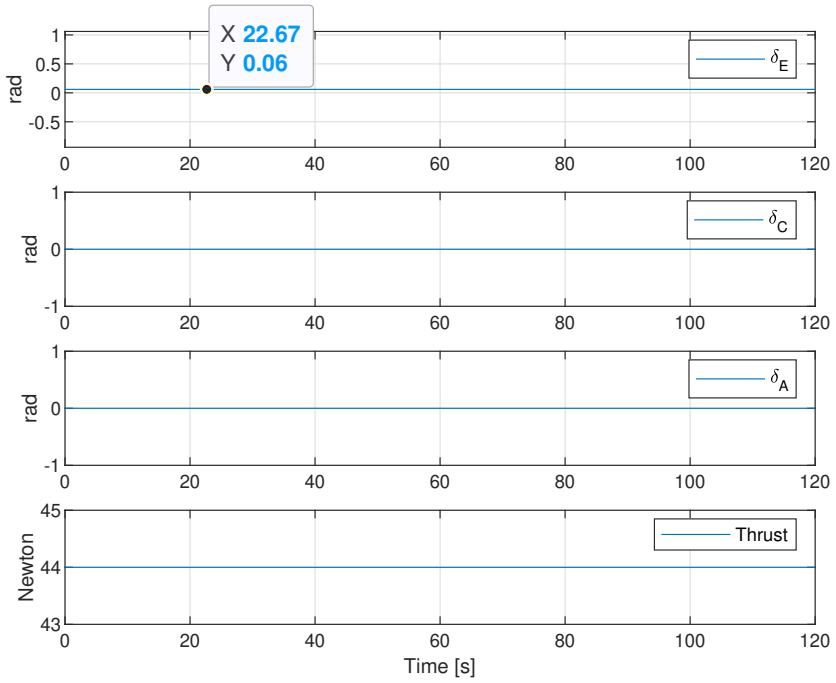

Figure 6.17: Static control deflections over 120 seconds of simulation. Source: Author.

It takes a few seconds for the aircraft to begin to stabilize; however, it still appears to be stable with fixed control actions. A phugoid oscillation in the longitudinal dynamics can be observed in Figure 6.18. This behavior occurs because the aircraft is trying to stabilize itself. Additionally, the simulation was started with the state variable values shown in equation 6.20.

$$\begin{bmatrix} u \\ v \\ w \\ p \\ q \\ r \\ \phi \\ \theta \\ \psi \end{bmatrix} = \begin{bmatrix} 40 \\ 0 \\ 2 \\ 0 \\ 0 \\ 0 \\ 0 \\ 0.03 \\ 0 \end{bmatrix} \tag{6.20}$$

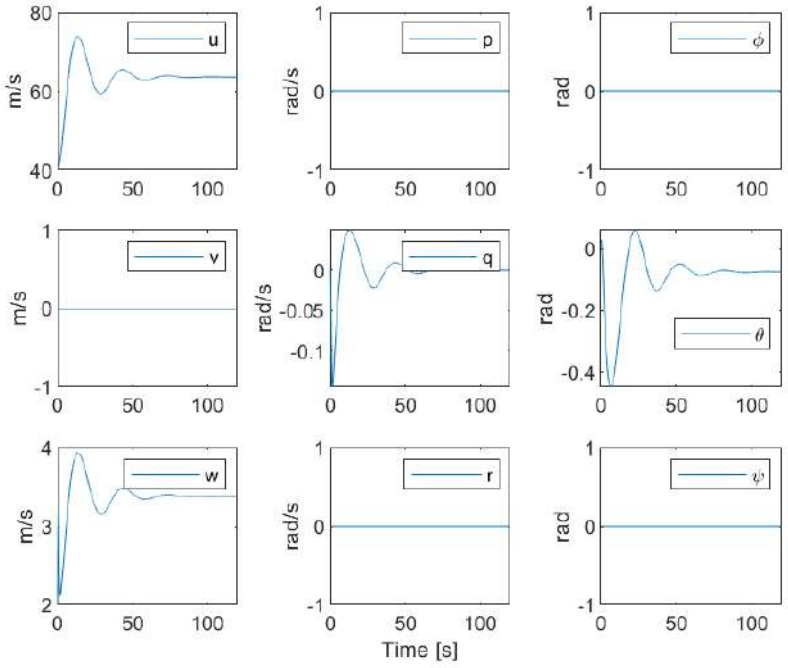

Figure 6.18: State variables behavior over 120 seconds of simulation with no control deflections. Source: Author.

The aircraft model simulated in Simulink appears to be a stable aerodynamic model; even with a given state condition and deflected control surfaces, the aircraft still dampens its behavior.

6.3.2 Step Input Signals

To evaluate the response of the aircraft, one step deflection signal was randomly generated by the elevator. The step pulse has 0.4 seconds of duration and it is applied at second 10. The simulation was run in Simulink with positive elevator deflection step. The Figure 6.19 shows the amplitudes of the pulse.

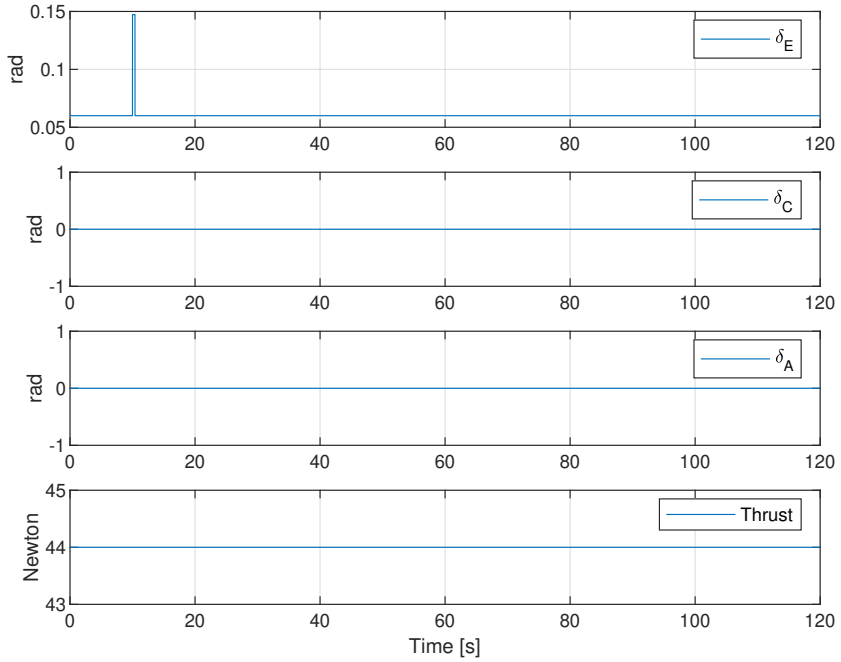

Figure 6.19: Control deflections behavior over 120 seconds of simulation with two positive step signals. Source: Author.

With the step input signals, the aircraft exhibited a different behavior in terms of speed and pitching rate. Due to the reduced scale factor the step time interval should be reduced, because a long elevator perturbation shall be catastrophic. Figure 6.20 shows the results for the second set of step input signals.

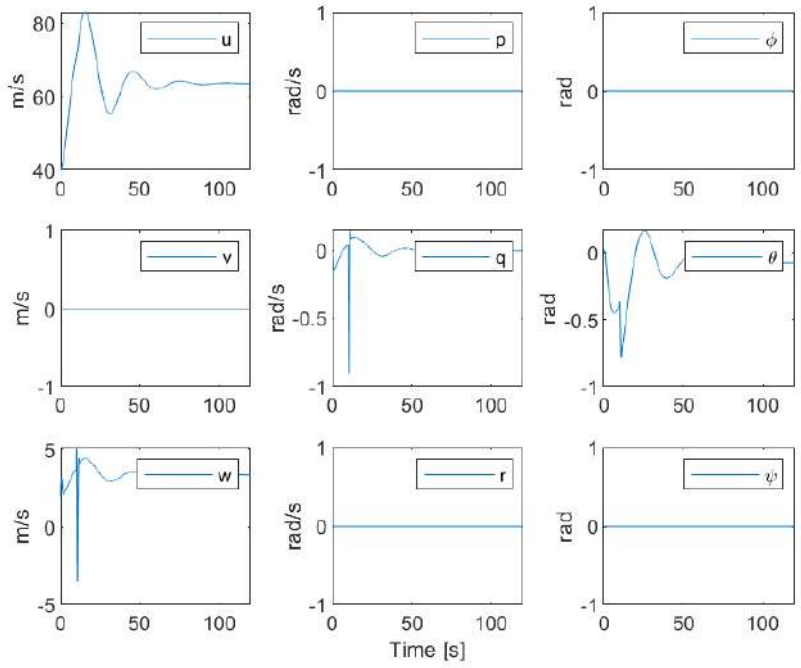

Figure 6.20: State variables behavior over 120 seconds of simulation with two positive step signals. Source: Author.

The step input signals showed that the aerodynamic model created for the GFF is a dynamically stable model of the aircraft. However, it is a unsteady condition model, which means that steady-state conditions are difficult to be simulate.

6.3.3 Unsteady Simulation

The unsteady simulation uses the control surface deflections recorded during the flight test. In this state, the C_{Y_α} stability derivative does not affect the simulation as it does in the steady state. The Fig. 6.21 presents the control surface variation over time, and they are presented in the following order: δ_E, δ_C, δ_A and δ_T.

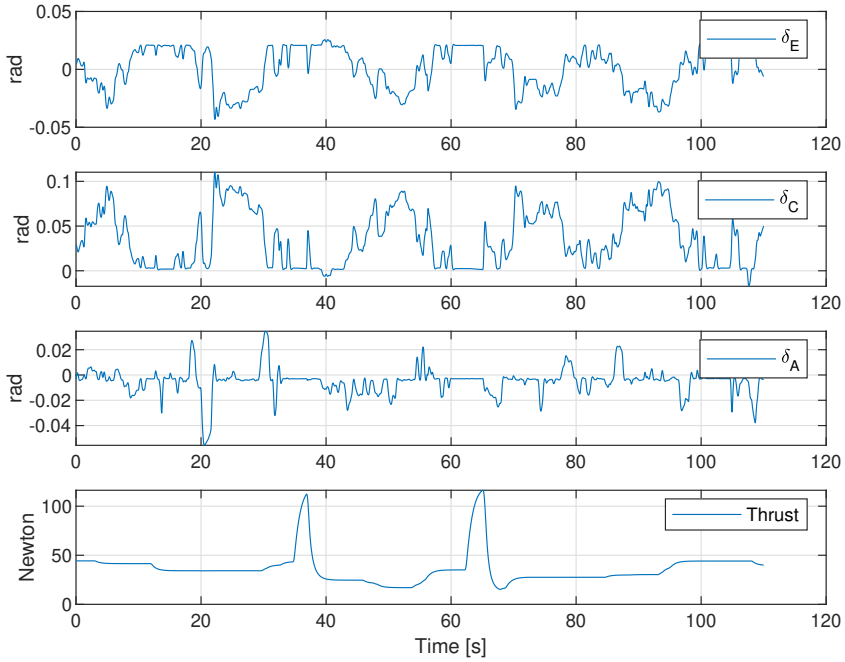

Figure 6.21: Control variables behavior over 60 seconds of simulation. Source: Author.

The results of the simulation with unsteady control inputs can be observed in Fig. 6.22, which shows the states of the aircraft (X vector). The simulation was performed for 110 seconds and the input control surfaces were the real data obtained from the flight tests of the aircraft. The interval used to feed the model is the same as that shown in Fig. 3.8.

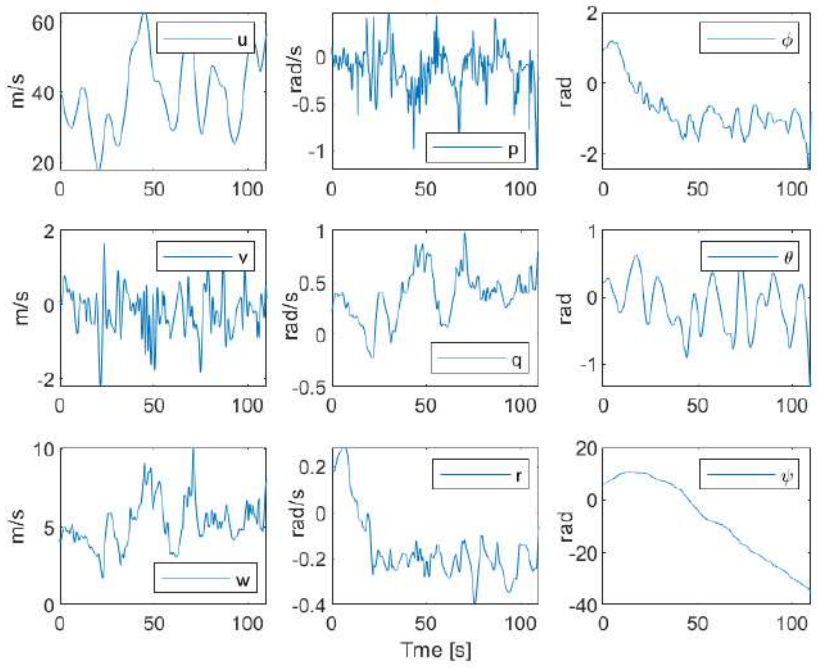

Figure 6.22: State variables behavior over 60 seconds of simulation. Source: Author.

It can be observed that the elevator and aileron deflections at 20 seconds and 30 seconds affect the longitudinal motion, explaining some peaks in the u and w velocities, as well as the pitching rate.

The Z-axis Euler angle (ψ) starts at 6 radians, increases to 11 radians, and then begins to decrease. This high oscillation can be related to the equation used to calculate angular acceleration, which does not reset to 0 after completing a 2π turn, but continues to increase in value. The equation 6.21 shows how angular accelerations are calculated (source: (LARSSON, 2019)).

$$\begin{bmatrix} \dot{\phi} \\ \dot{\theta} \\ \dot{\psi} \end{bmatrix} = \begin{bmatrix} p + qsin(\phi)tan(\theta) + rcos(\phi)tan(\theta) \\ qcos(\phi) - rsin(\phi) \\ qsin(\phi)sec(\theta) + rcos(\phi)sec(\theta) \end{bmatrix} \tag{6.21}$$

The value of the angle of attack of the aircraft was also compared to the flight data. The behavior of the predicted angle of attack, calculated by Eq. 6.22, is very close to the flight data. However, when the same approach is extended to the sideslip angle, there is a greater difference between the prediction and the flight data. The sideslip angle is calculated with Eq. 6.23.

$$\alpha = tan^{-1}(w/u) \tag{6.22}$$

$$\beta = sin^{-1}(v/V) \tag{6.23}$$

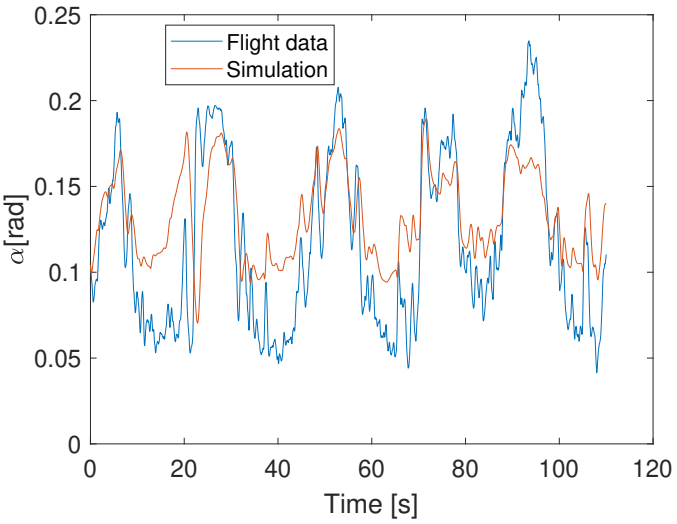

Figure 6.23: Comparison between simulated and recorded in the flight test for the angle of attack . Source: Author.

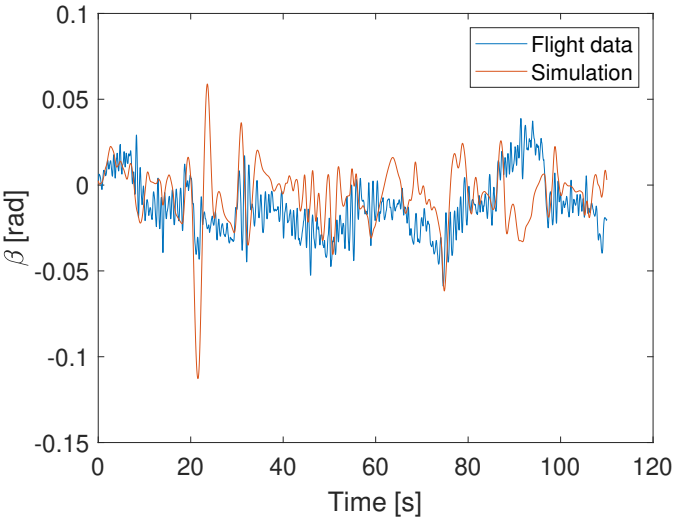

Figure 6.24: Comparison between simulated and recorded in the flight for the sideslip angle. Source: Author.

While the GFF simulation provides a commendable approximation of the aircraft state variables under varying control states, it requires further improvements to increase its accuracy. The current version of the aerodynamic model, lacks crucial lon-

gitudinal and lateral-directional damping parameters, such as C_{m_q} and C_{n_r}. Future work should aim to incorporate these elements to promote a more stable and reliable aerodynamic model.

Nevertheless, despite the need for refinement, the simulation of the GFF provides a valuable approximation of the aircraft state variables as the control states vary according to the input signals given by the pilot during flight testing. This demonstrates its potential as a basis for further development and improvement in future work.

Chapter 7

Conclusions

This study has introduced an alternative and innovative approach to perform system identification on a reduced scale fighter aircraft, the GFF, using the Adaptive Network-based Fuzzy Inference System (ANFIS) or Neuro-Fuzzy. The presented Neuro-Fuzzy architecture integrates Differential Evolution as an optimization method, predicts parameters from membership functions and outputs consequent functions.

To select Neuro-Fuzzy with Differential Evolution, three additional configurations were tested using experimental aerodynamic flight data. These configurations included two additional optimization methods (Complex RF and Genetic Algorithm) and one additional Fuzzy Inference Method (Pondered Individual Analysis). Chapter 4 presents the comparisons and conclusions. Additionally, the same chapter includes a comparison between the shapes of the membership functions and types of output functions. The results showed that the NF-DE is the best method tested to perform the system identification of the GFF.

According to the results presented in Chapter 5, NF-DE is capable of mimicking the aircraft behavior based on only three input variables and predicting the aircraft behavior in other flight intervals that fall within the boundaries of the training limits. However, NF-DE is unable to accurately capture the high peaks of oscillation in all aerodynamic coefficients. As shown in Section 5, it is apparent that the force and moment coefficients do not align well with the extremes of the curves.

The flight simulation is capable of replicating the behavior of the GFF by using Neuro-Fuzzy predictions of the forces and moment coefficients. However, some improvements are needed to further refine the simulation. These include incorporating

damping stability derivatives into the pitching moment coefficient (C_{m_q}) and yawing moment coefficient (C_{n_r}). In addition, increasing the number of input variables in the Neuro-Fuzzy model would help reduce the error in training and validation.

As future work, it is recommended to increase the number of input variables in an attempt to capture the missing peaks observed in the training and validation in Chapter 5, also it is important to evaluate the uncertainties alongside the model training. In addition, it is proposed to more accurately model the thrust and twisting moments of the aircraft to ensure a better approximation of the tangential aerodynamic force and rolling moment, respectively. Implementation of these adjustments is expected to significantly improve the GFF simulation, paving the way for more accurate and reliable modeling. Finally, a self-adaptive Neuro-Fuzzy will be created to allow the model to self-improve with on-board data collection.

References

AGGARWAL, C. C. et al. Neural networks and deep learning. **Springer**, Springer, v. 10, n. 978, p. 3, 2018.

ANDERSON, J. D. **Aircraft performance & design**. [S.l.]: McGraw-Hill Science Engineering, 1999.

BOX, M. A new method of constrained optimization and a comparison with other methods. **The Computer Journal**, The British Computer Society, v. 8, n. 1, p. 42–52, 1965.

BRANDON, J. M.; MORELLI, E. A. Nonlinear aerodynamic modeling from flight data using advanced piloted maneuvers and fuzzy logic. 2012.

BRANDON, J. M.; MORELLI, E. A. Real-time onboard global nonlinear aerodynamic modeling from flight data. **Journal of Aircraft**, American Institute of Aeronautics and Astronautics, v. 53, n. 5, p. 1261–1297, 2016.

BRAUN, R.; KRUS, P. Parallel implementations of the complex-rf algorithm. **Engineering Optimization**, Taylor & Francis, v. 49, n. 9, p. 1558–1572, 2017.

CARVALHO, F. C.; OLIVEIRA, M. V. Fernandes de; LARA-MOLINA, F. A.; JR, A. A. C.; JR, V. S. Fuzzy robust control applied to rotor supported by active magnetic bearing. **Journal of Vibration and Control**, SAGE Publications Sage UK: London, England, v. 27, n. 7-8, p. 912–923, 2021.

ETKIN, B.; REID, L. D. **Dynamics of flight: stability and control**. [S.l.]: John Wiley & Sons, 1995.

FOSSEN, T. I. Mathematical models for control of aircraft and satellites. **Department of Engineering Cybernetics Norwegian University of Science and Technology**, 2011.

HOLLAND, J. H. **Adaptation in natural and artificial systems: an introductory analysis with applications to biology, control, and artificial intelligence**. [S.l.]: MIT press, 1992.

JAFELICE, R. M.; BARROS, L. C. de; BASSANEZI, R. C.; GOMIDE, F. Fuzzy modeling in symptomatic hiv virus infected population. **Bulletin of Mathematical Biology**, Springer, v. 66, n. 6, p. 1597–1620, 2004.

JAFELICE, R. S. d. M.; BARROS, L. C. d.; BASSANEZI, R. C. Usando a teoria dos conjuntos fuzzy na modelagem de fenômenos biológicos. In: **II Congresso Brasileiro de Sistemas Fuzzy, Natal-RN**. [S.l.: s.n.], 2012.

JAFELICE, R. S. d. M. et al. Modelagem fuzzy para dinâmica de transferência de soropositivos para hiv em doença plenamente manifesta. [sn], 2003.

JANG, J.-S. Anfis: adaptive-network-based fuzzy inference system. **IEEE transactions on systems, man, and cybernetics**, IEEE, v. 23, n. 3, p. 665–685, 1993.

JOUANNET, C.; BERRY, P.; MELIN, T.; AMADORI, K.; LUNDSTRÖM, D.; STAACK, I. Subscale flight testing used in conceptual design. **Aircraft Engineering and Aerospace Technology**, Emerald Group Publishing Limited, v. 84, n. 3, p. 192–199, 2012.

KARALI, H.; INALHAN, G.; DEMIREZEN, M. U.; YUKSELEN, M. A. A new nonlinear lifting line method for aerodynamic analysis and deep learning modeling of small unmanned aerial vehicles. **International Journal of Micro Air Vehicles**, SAGE Publications Sage UK: London, England, v. 13, p. 17568293211016817, 2021.

KRUS, P. et al. Simulation based optimisation for system design. In: **DS 31: Proceedings of ICED 03, the 14th International Conference on Engineering Design, Stockholm**. [S.l.: s.n.], 2003. p. 459–460.

LARSSON, R. **Flight test system identification**. [S.l.]: Linköping University Electronic Press, 2019.

LARSSON, R.; RINGERTZ, U.; LUNDSTRÖM, D.; SOBRON, A. Rapid prototyping in aircraft design using cfd, wind tunnel and flight testing. In: **Proceedings of the 33rd Congress of the International Council of the Aeronautical Sciences, Stockholm, Sweden**. [S.l.: s.n.], 2022. p. 4–9.

LI, K.; KOU, J.; ZHANG, W. Deep learning for multifidelity aerodynamic distribution modeling from experimental and simulation data. **AIAA Journal**, American Institute of Aeronautics and Astronautics, p. 1–15, 2022.

LUNDSTRÖM, D.; SOBRON, A.; KRUS, P.; JOUANNET, C.; SILVA, R. G. A. da. Subscale flight testing of a generic fighter aircraft. In: INTERNATIONAL COUNCIL OF THE AERONAUTICAL SCIENCES. **30th Congress of the International Council of the Aeronautical Sciences (ICAS), September 25-30, Daejeon, South Korea**. [S.l.], 2016.

MCCULLOCH, W. S.; PITTS, W. A logical calculus of the ideas immanent in nervous activity. **The bulletin of mathematical biophysics**, Springer, v. 5, p. 115–133, 1943.

PEREIRA, B. L.; JAFELICE, R. M.; FINZI, R. M. An approach of pondered individual analysis method in aircraft control. **Journal of the Brazilian Society of Mechanical Sciences and Engineering**, Springer, v. 44, n. 11, p. 1–16, 2022.

PEREIRA, B. L. et al. Aplicação de sistemas neuro-fuzzy e evolução diferencial na modelagem e controle de veículo de duas rodas. Universidade Federal de Uberlândia, 2017.

PEREIRA, B. L. et al. Aplicação de sistemas neuro-fuzzy no controle de aeronaves em operações críticas de voo. Universidade Federal de Uberlândia, 2021.

RAJKUMAR, T.; BARDINA, J. E. Prediction of aerodynamic coefficients using neural networks for sparse data. In: **FLAIRS Conference**. [S.l.: s.n.], 2002. p. 242–246.

ROSKAM, J. **Airplane flight dynamics and automatic flight controls**. [S.l.]: DAR-corporation, 1998.

ROY, A. G.; PEYADA, N. Lateral aircraft parameter estimation using neuro-fuzzy and genetic algorithm based method. In: IEEE. **2017 IEEE Aerospace Conference**. [S.l.], 2017. p. 1–11.

ROY, A. G.; PEYADA, N. Longitudinal aircraft parameter estimation using neuro-fuzzy and genetic algorithm based method. In: **AIAA Atmospheric Flight Mechanics Conference**. [S.l.: s.n.], 2017. p. 3896.

RUEDA, A. S. **On Subscale Flight Testing: Cost-effective techniques for research and development**. Phd Thesis (PhD Thesis) — Linköping University Electronic Press, 2021.

SANT'ANA, V. T. et al. Aerodynamic modeling using neuro-fuzzy for a scaled model of cessna 182. Universidade Federal de Uberlândia, 2019.

SOBRON, A.; LUNDSTRÖM, D.; STAACK, I.; KRUS, P. Design and testing of a low-cost flight control and data acquisition system for unstable subscale aircraft. In: THE INTERNATIONAL COUNCIL OF THE AERONAUTICAL SCIENCES. **30th Congress of The International Council of the Aeronautical Sciences (ICAS), Daejeon, Korea, September 25-30, Daejeon, South Korea.** [S.l.], 2016.

SPENDLEY, W.; HEXT, G. R.; HIMSWORTH, F. R. Sequential application of simplex designs in optimisation and evolutionary operation. **Technometrics**, Taylor & Francis, v. 4, n. 4, p. 441–461, 1962.

STORN, R.; PRICE, K. Differential evolution–a simple and efficient heuristic for global optimization over continuous spaces. **Journal of global optimization**, Springer, v. 11, n. 4, p. 341–359, 1997.

TAO, J.; SUN, G. Application of deep learning based multi-fidelity surrogate model to robust aerodynamic design optimization. **Aerospace Science and Technology**, Elsevier, v. 92, p. 722–737, 2019.

TATAR, M.; SABOUR, M. H. Reduced-order modeling of dynamic stall using neuro-fuzzy inference system and orthogonal functions. **Physics of Fluids**, AIP Publishing LLC, v. 32, n. 4, p. 045101, 2020.

Appendix A

Some calculations performed inside the GFF simulation are:

Velocities rate:

$$\begin{bmatrix} \dot{u} \\ \dot{v} \\ \dot{w} \end{bmatrix} = \begin{bmatrix} \frac{1}{m} F_A^b - w^b \times V^b \end{bmatrix} \tag{A.1}$$

In this expression:

- F_A^b is the aerodynamic forces in the body frame.
- V^b is the aircraft velocities in the body frame.
- w^b is the angular velocity vector in the body frame.

Angular accelerations:

$$\begin{bmatrix} \dot{p} \\ \dot{q} \\ \dot{r} \end{bmatrix} = \begin{bmatrix} \mathbf{I}_b^{-1} \left(\mathbf{M}_{cg}^b - \mathbf{w}^b \times (\mathbf{I}_b \cdot \mathbf{w}^b) \right) \end{bmatrix} \tag{A.2}$$

In this expression:

- I_b^{-1} is the inverse of the inertia matrix in the body frame.
- M_{cg}^b is the moment acting on the center of gravity in the body frame.
- w^b is the angular velocity vector in the body frame.

Angular velocities

$$\begin{bmatrix} \dot{\phi} \\ \dot{\theta} \\ \dot{\psi} \end{bmatrix} = \begin{bmatrix} H_{\phi}\mathbf{w}^{b} \end{bmatrix} \tag{A.3}$$

Where

$$H_{\phi} = \begin{bmatrix} 1 & \sin(x_7)\tan(x_8) & \cos(x_7)\tan(x_8) \\ 0 & \cos(x_7) & -\sin(x_7) \\ 0 & \frac{\sin(x_7)}{\cos(x_8)} & \frac{\cos(x_7)}{\cos(x_8)} \end{bmatrix} \tag{A.4}$$